

SOLVING ATOMIC STRUCTURES USING STATISTICAL MECHANICAL SEARCHES ON
X-RAY SCATTERING DERIVED POTENTIAL ENERGY SURFACES

by

Christopher James Wright

Bachelor of Science
Brown University 2014

Submitted in Partial Fulfillment of the Requirements

for the Degree of Masters of Science in

Chemical Engineering

College of Engineering and Computing

University of South Carolina

2016

Accepted by:

Xiao-Dong Zhou, Major Professor

Mark Uline, Committee Member

Jochen Lauterbach, Committee Member

Lacy Ford, Vice Provost and Dean of Graduate Studies

© Copyright by Christopher James Wright, 2016
All Rights Reserved.

DEDICATION

To Diane & Donald Wright

My first scientific advisers

To see a World in a Grain of Sand

ACKNOWLEDGMENTS

This work would not have been possible without my entire ensemble of colleagues, advisers, friends, and family.

To Dr. Sanjit Ghose thank you very much for getting me started in the x-ray field and sticking with me, even when I went into the mathematical deep end. To Dr. Yan Li, thank you very much for always pushing my simulations to be the best they could be, and pushing me to search every possible nook and cranny of parameter space.

To Emir, thank you very much for being my partner in beamtime. I hope you continue your x-ray work. I'd also like to thank the NSLS-II XPD team for their experimental, intellectual, and moral support. To Dr. Thomas Caswell, Dr. Eric Dill, and Dr. Dan Allen, I would not be $1e^{-6}$ of the programmer I am today without your guidance, conversation, and explanations.

To Prof. Scopatz, thank you very much for your insights, conversation, and being a spectacular developer role model.

To my many readers, I'd like to say thank you, if my thesis hasn't put you to sleep already.

To my parents, I don't know if any language could correctly render the magnitude of my gratitude for everything you have done for me.

Last, but certainly not least, Prof. Zhou. I am certain that I could not have gotten a better start in research science than working with you.

ABSTRACT

Engineering the next generation of materials, especially nanomaterials, requires a detailed understanding of the material's underlying atomic structure. Understanding these structures we can obtain a better understanding of the structure-property relationship, allowing for a property driven rational design of the material structure on the atomic level. Even more importantly, understanding the structure in-situ will allow the reversal of the flow of information, translating stimuli and responses on the macroscopic system level to changes in the atomic structure. Despite the importance of atomic structures for designing materials, solving the atomic structure of materials is difficult both experimentally and computationally. Atomic pair distribution functions (PDFs) have been shown to provide information on atomic structure, although extracting the PDF from x-ray total scattering measurements can be difficult. Computationally, translating the PDF to an atomic structure requires the search of a very high dimensional space and can be computationally expensive.

This work aims to address these issues by developing 1) novel statistical mechanical approaches to solving material structures, 2) fast simulation of x-ray total scattering and atomic pair distribution functions (PDFs), and 3) data processing procedures for experimental x-ray total scattering measurements. First, experimentally derived potential energy surfaces (PES) and the statistical mechanical ensembles used to search them are developed. Then the mathematical and computational framework for the PDF and its gradients will be discussed. The combined PDF-PES-ensemble system will be benchmarked against a series of nanoparticle structures to ascertain the efficiency and effectiveness of the system. Experimental data processing proce-

dures, which maximize the usable data, will be presented. Finally, preliminary results from experimental x-ray total scattering measurements will be discussed. This work presents one of the most complete end-to-end systems for processing and modeling x-ray total scattering PDF data, potentially allowing for high-throughput structural solution.

TABLE OF CONTENTS

DEDICATION	iii
ACKNOWLEDGMENTS	iv
ABSTRACT	v
LIST OF FIGURES	x
CHAPTER 1 INTRODUCTION	1
CHAPTER 2 STATISTICAL MECHANICAL ENSEMBLES AND POTENTIAL ENERGY SURFACES	3
2.1 Introduction	3
2.2 Potential Energy Surfaces	3
Experimentally Derived Potential Energy Surfaces	4
Potentials	4
Forces	5
2.3 Ensembles	6
Monte Carlo Modeling	7
Hamiltonian Monte Carlo	8
No-U-Turn Sampling	10
Grand Canonical Ensemble	10
Ensemble description	11
Grand Canonical Monte Carlo	11
GCMC biasing	12
2.4 Conclusions	15
CHAPTER 3 ATOMIC PAIR DISTRIBUTION FUNCTION: THEORY AND COMPUTATION	16

3.1	Introduction	16
3.2	Theory	17
	Derivation	17
	Analytically Gradients	18
	Without ADPs	19
	Periodic Boundary Conditions	20
3.3	Computation	20
	HPC and GPUs	21
	GPUs and Parallelization	21
	Map from ij space to k space	22
	GPU Memory Allocation	24
	Speed and Scaling of PDF Computation	26
3.4	Conclusions	27
 CHAPTER 4 BENCHMARKS		 28
4.1	Introduction	28
	Target Setup	29
	Model Parameters	30
4.2	Structural Solutions	31
	Case I: crystalline Au ₅₅	31
	Case II: Au ₅₅ with surface disorder	32
	Case III: amorphous Au ₅₅	34
	Case IV: ligand-protected Au ₁₀₂	36
	Starting from fcc structure	36
	Starting from Marks Decahedron	38
4.3	Discussion and Conclusion	39
 CHAPTER 5 X-RAY TOTAL SCATTERING DATA ACQUISITION AND PROCESSING		 42
5.1	Introduction	42
5.2	Detector <i>Q</i> resolution	42
5.3	Automated Mask Generation	45
	Introduction	45

Algorithm Design	46
Test Cases	46
Results and Discussion	47
Conclusions	53
5.4 Automated Image Azimuthal Integration	54
5.5 Conclusions	59
CHAPTER 6 PHASE CHANGES AND ANNEALING DYNAMICS OF Pr_2NiO_4 AND ITS DERIVATIVES	60
6.1 Introduction	60
6.2 Experiments	61
Pr_2NiO_4 Synthesis	61
X-ray Measurements	61
6.3 Data Processing	61
6.4 Data Analysis	62
Intra Sample Comparison	62
PDF	62
$I(Q)$	67
Inter Sample Comparison	72
6.5 Simulation	75
6.6 Conclusions	75
CHAPTER 7 CONCLUSION	77
BIBLIOGRAPHY	80
APPENDIX A SUPPLEMENTAL INFORMATION: PHASE CHANGES AND AN- NEALING DYNAMICS OF Pr_2NiO_4 AND ITS DERIVATIVES . . .	86
Intra Sample Comparison	86
Inter Sample Comparison	99

LIST OF FIGURES

Figure 2.1	Addition biasing with a Lennard Jones potential.	14
Figure 3.1	Comparison of the CPU and GPU chip architectures	21
Figure 3.2	Speed comparison of CPU and GPU implementations	26
Figure 4.1	Au ₅₅ PDF fitting of DFT-optimized <i>c</i> -Au ₅₅ .	32
Figure 4.2	Au ₅₅ PDF fitting of surface-disordered Au ₅₅ .	33
Figure 4.3	Similar to figure 4.2 for DFT-optimized amorphous Au ₅₅ .	35
Figure 4.4	Similar to Fig. 4.2 for Au ₁₀₂ as in DFT-optimized Au ₁₀₂ MBA ₄₄ cluster.	37
Figure 4.5	Similar to Fig. 4.4 with Marks decahedron as the starting structure.	38
Figure 5.1	Scattering onto a flat detector	43
Figure 5.2	Q resolution as a function of Q .	44
Figure 5.3	Number of pixels as a function of Q , binned at the Q resolution of the detector.	45
Figure 5.4	Generated dead/hot pixel masks for a detector with 100 bad pixels.	48
Figure 5.5	Generated dead/hot pixel masks for a detector with 300 bad pixels.	48
Figure 5.6	Generated dead/hot pixel masks for a detector with 500 bad pixels.	49
Figure 5.7	Generated dead/hot pixel masks for a detector with 1000 bad pixels.	49
Figure 5.8	Generated beamstop holder masks for a beamstop holder with 10% transmittance.	50

Figure 5.9 Generated beamstop holder masks for a beamstop holder with 30% transmittance.	50
Figure 5.10 Generated beamstop holder masks for a beamstop holder with 50% transmittance.	50
Figure 5.11 Generated beamstop holder masks for a beamstop holder with 90% transmittance.	51
Figure 5.12 Generated beamstop holder masks which is rotated away from vertical	51
Figure 5.13 Masked experimental data.	52
Figure 5.14 Masked experimental data with Pt single crystal signal.	52
Figure 5.15 Masked experimental data with Pt single crystal signal using figure's 5.13 mask as a starting mask.	53
Figure 5.16 Masking, average, and standard deviation of an example x-ray total scattering measurement with with no mask.	56
Figure 5.17 Masking, average, and standard deviation of an example x-ray total scattering measurement with with only an edge mask.	57
Figure 5.18 Masking, average, and standard deviation of an example x-ray total scattering measurement with combining an edge mask and the automatically generated mask.	58
Figure 6.1 PDF as a function of temperature for as synthesized PNO showing the full PDF	63
Figure 6.2 PDF as a function of temperature for as synthesized PNO showing a close up on the short range section	64
Figure 6.3 PDF as a function of temperature for PNO annealed at 750 °C for 25 hours showing the full PDF	65
Figure 6.4 PDF as a function of temperature for PNO annealed at 750 °C for 25 hours showing a close up on the short range section	66
Figure 6.5 $I(Q)$ as a function of temperature for as synthesized PNO showing the full XRD	68

Figure 6.6 $I(Q)$ as a function of temperature for as synthesized PNO showing a close up on the low Q section	69
Figure 6.7 $I(Q)$ as a function of temperature for PNO annealed at 750 °C for 25 hours showing the full XRD	70
Figure 6.8 $I(Q)$ as a function of temperature for PNO annealed at 750 °C for 25 hours showing a close up on the low Q section	71
Figure 6.9 Comparison of PNO sample PDFs as a function of annealing time high-temp	73
Figure 6.10 Comparison of PNO sample $I(Q)$ as a function of annealing time high-temp	74
Figure A.1 PDF as a function of temperature for PNO annealed at 750 °C for 50 hours showing the full PDF	87
Figure A.2 PDF as a function of temperature for PNO annealed at 750 °C for 50 hours showing a close up on the short range section	88
Figure A.3 PDF as a function of temperature for PNO annealed at 750 °C for 100 hours showing the full PDF	89
Figure A.4 PDF as a function of temperature for PNO annealed at 750 °C for 100 hours showing a close up on the short range section	90
Figure A.5 PDF as a function of temperature for PNO annealed at 750 °C for 200 hours showing the full PDF	91
Figure A.6 PDF as a function of temperature for PNO annealed at 750 °C for 200 hours showing a close up on the short range section	92
Figure A.7 $I(Q)$ as a function of temperature for PNO annealed at 750 °C for 50 hours showing the full XRD	93
Figure A.8 $I(Q)$ as a function of temperature for PNO annealed at 750 °C for 50 hours showing a close up on the low Q section	94
Figure A.9 $I(Q)$ as a function of temperature for PNO annealed at 750 °C for 100 hours showing the full XRD	95
Figure A.10 $I(Q)$ as a function of temperature for PNO annealed at 750 °C for 100 hours showing a close up on the low Q section	96

Figure A.11 $I(Q)$ as a function of temperature for PNO annealed at 750 °C for 200 hours showing the full XRD	97
Figure A.12 $I(Q)$ as a function of temperature for PNO annealed at 750 °C for 200 hours showing a close up on the low Q section	98
Figure A.13 Comparison of PNO sample PDFs as a function of annealing time at room temperature	100
Figure A.14 Comparison of PNO sample PDFs as a function of annealing time at room temperature	101
Figure A.15 Comparison of PNO sample PDFs as a function of annealing time at room temperature	102
Figure A.16 Comparison of PNO sample PDFs as a function of annealing time at room temperature	103
Figure A.17 Comparison of PNO sample PDFs as a function of annealing time at operating temperature	104
Figure A.18 Comparison of PNO sample PDFs as a function of annealing time at operating temperature	105
Figure A.19 Comparison of PNO sample PDFs as a function of annealing time at operating temperature	106
Figure A.20 Comparison of PNO sample PDFs as a function of annealing time at operating temperature	107
Figure A.21 Comparison of PNO sample PDFs as a function of annealing time cooled back to room temperature	108
Figure A.22 Comparison of PNO sample PDFs as a function of annealing time cooled back to room temperature	109
Figure A.23 Comparison of PNO sample PDFs as a function of annealing time cooled back to room temperature	110
Figure A.24 Comparison of PNO sample PDFs as a function of annealing time cooled back to room temperature	111
Figure A.25 Comparison of PNO sample $I(Q)$ as a function of annealing time at room temperature	112

Figure A.26 Comparison of PNO sample $I(Q)$ as a function of annealing time at operating temperature 113

Figure A.27 Comparison of PNO sample $I(Q)$ as a function of annealing time cooled back to room temperature 114

1

CHAPTER 1

2

INTRODUCTION

3 Engineering materials and chemicals on the atomic scale has long been a goal for the
4 chemistry, physics, materials science, and chemical engineering fields. Realizing this
5 goal could lead to durable fuel cell catalysts, more bioavailable pharmaceuticals, and
6 radiation damage resistant spacecraft shielding. Before we can even think of making
7 atomistically exact structures, durable structures, or structures which change in re-
8 producible ways, we need to know the atomic structure exactly. This work addresses
9 these issues by developing a methodology for solving the structure of nanomaterials
10 by matching experimental x-ray scattering data with simulated atomic structures.

11 Chapter 2 develops the statistical mechanical system used to match the theoretical
12 structure. §2.2 focuses on the development of potential energy surfaces, including
13 potential energy and force equations, which have minima where experimental results
14 and simulated structures agree the most. §2.3 will discuss statistical mechanical
15 ensembles which are used to search for minima on the potential energy surface.

16 Chapter 3 will discuss the mathematical and computational development of the
17 atomic pair distribution function (PDF). §3.3 will focus on the rapid graphical pro-
18 cessing unit based calculation of the PDF and its gradients.

19 Chapter 4 will discuss the benchmarking of the the combined statistical mechan-
20 ical optimizer and PDF calculation systems against a series of theoretical nanoparti-
21 cles, focusing on understanding limitations of the method and structure reproduction.

22 Chapter 5 will focus on the acquisition of experimental data, its management, and
23 processing. §5.2, 5.3, and 5.4 will discuss the derivation of the Q resolution function,

24 the automated masking of 2D area detectors for x-ray total scattering measurements
25 using the previously derived Q resolution, and the impact of different averaging meth-
26 ods and masks on azimuthal integration, respectively.

27 Chapter 6 will discuss preliminary experimental results investigating the phase
28 changes and local structure of Pr_2NiO_4 , revealing the influence of thermal history on
29 the structure.

30

CHAPTER 2

31

STATISTICAL MECHANICAL ENSEMBLES AND POTENTIAL ENERGY SURFACES

32 33 2.1 INTRODUCTION

34 The approach taken in this work for solving the atomic structures of materials is one
35 of optimization. The plan is to develop a potential energy surface (PES) which has
36 minima associated with atomic structures who's properties match the experimentally
37 observed properties. Thus, the various positional variables of the structure can be
38 solved by optimizing the structure against the PES. This approach is popular in the
39 PDF community for solving the structure of materials using both extensive large box
40 models and simpler small box models.

41 In this chapter we discuss the development of the various PESs used in the PDF
42 community for comparing theoretical and experimental PDFs. Special attention will
43 be paid to the gradients of the potential energy functions, as these are important
44 to some optimization techniques. Additionally, we also discuss the use of statistical
45 mechanical ensembles for finding minima on the PES.

46 2.2 POTENTIAL ENERGY SURFACES

47 A PES simply describes the potential energy of the system as a function of all its
48 relevant coordinates in phase space, essentially providing a mapping $\mathbb{R}^n \rightarrow \mathbb{R}$, where \mathbb{R}
49 is the set of real numbers and n is the number of positional parameters in the system.
50 Usually these coordinates are the positions of the atoms q and their conjugate the

51 momenta p . Note that there could be more variables associated with the system,
52 for instance the magnetic moments of the atoms could play a role in describing the
53 system. In this magnetic system there would be positional variables for the atom-wise
54 spin vectors and their "momenta". Application of the term "momenta" might seem
55 odd here, as the magnetic spin does not have a mass or a velocity. However, since the
56 magnetic "position" is defined on the PES we need to describe its conjugate variable
57 to properly formulate Hamiltonian dynamics and the kinetic portion of the PES.

58 Experimentally Derived Potential Energy Surfaces

59 Generally PESs are obtained from purely computational experiments including: ab-
60 initio DFT, classical approximations via the embedded atom method, or even param-
61 eter driven models with experimentally fitted parameters. However, one can derive
62 a PES from an experiment which describes how well the model reproduces the ex-
63 perimental data. In this case one needs a theoretical and computational framework
64 mapping the atomistic variables of the simulation to the same space of the data ob-
65 tained from the experiment. This allows the experiment to be compared directly
66 against the predicted data via an experimentally derived PES.

67 Potentials

68 For an experiment which produces 1D data, like powder diffraction, EXAFS or XPS,
69 the implemented potentials are:

$$\chi^2 = \sum_{a=a_{\min}}^{a_{\max}} (A_{\text{obs}} - \alpha A_{\text{calc}})^2 \quad (2.1)$$

70

$$Rw = \sqrt{\frac{\sum_{a=a_{\min}}^{a_{\max}} (A_{\text{obs}} - \alpha A_{\text{calc}})^2}{\sum_{a=a_{\min}}^{a_{\max}} A_{\text{obs}}^2}} \quad (2.2)$$

71

$$\chi^2_{\text{INVERT}} = \frac{1}{N} \sum_j \sum_r [A_{\text{obs}}(r) - \alpha A_{j\text{calc}}(r)]^2 \quad (2.3)$$

72

$$\alpha = \frac{\sum_{a=a_{\min}}^{a_{\max}} A_{\text{obs}} A_{\text{calc}}}{\sum_{a=a_{\min}}^{a_{\max}} A_{\text{calc}}^2} = \frac{\vec{A}_{\text{obs}} \cdot \vec{A}_{\text{calc}}}{|\vec{A}_{\text{calc}}|^2} \quad (2.4)$$

73 where A_{calc} and A_{obs} are the calculated and observed 1D experimental data and $A_{\text{calc},j}$
 74 is the calculated data for a single atom interacting with the other atoms of the system.
 75 Note that A_{calc} has a dependence on q , the positions of the system.

76 The Rw and χ^2 potentials have been reported numerous times. [46, 35, 7, 36, 48]
 77 Essentially these potentials measure the least squares distance between the observed
 78 scattering and the predicted scattering providing a way to quantify the agreement
 79 between the model and experiment. While RW and χ^2 are now standard in the PDF
 80 community, the INVERT potential is fairly new and aims to incorporate descriptions
 81 of the structural symmetry into the PES. [10, 11] In the case of the INVERT poten-
 82 tial NMR or other symmetry sensitive data is used to describe the number of unique
 83 atomic coordinations. This is then used to describe the number of unique atom-wise
 84 pair distribution functions, thus causing systems with more or less unique coordi-
 85 nation environments to be higher in energy. This approach has been shown to be
 86 useful for C_{60} and other systems which are highly symmetric, creating a PES with an
 87 easier to find minima. [10, 11] However, many times this kind of data is unavailable
 88 when refining the structure causing the potential to be less useful. Additionally, this
 89 potential introduces an element of user bias as the refiner must decide, based on some
 90 spectroscopic data, how many unique environments are in the material. This bias
 91 could be removed by using one of the other potentials with a method for simulat-
 92 ing the observed spectra, allowing the computational system decide what structures
 93 properly reproduce all the observed data.

94 **Forces**

$$\vec{\nabla} \chi^2 = -2 \sum_{a=a_{\min}}^{a_{\max}} \left(\alpha \frac{\partial A_{\text{calc}}}{\partial \gamma_{i,w}} + A_{\text{calc}} \frac{\partial \alpha}{\partial \gamma_{i,w}} \right) (A_{\text{obs}} - \alpha A_{\text{calc}}) \quad (2.5)$$

95

$$\vec{\nabla}Rw = \frac{Rw}{\chi^2} \sum_{a=a_{\min}}^{a_{\max}} (\alpha \frac{\partial A_{\text{calc}}}{\partial \gamma_{i,w}} + A_{\text{calc}} \frac{\partial \alpha}{\partial \gamma_{i,w}})(\alpha A_{\text{calc}} - (A_{\text{obs}})) \quad (2.6)$$

96

$$\vec{\nabla}\chi^2_{\text{INVERT}} = \frac{-2}{N} \sum_{a=a_{\min}}^{a_{\max}} \sum_j (\alpha \frac{\partial A_{j,\text{calc}}}{\partial \gamma_{i,w}} + A_{j,\text{calc}} \frac{\partial \alpha}{\partial \gamma_{i,w}})(A_{\text{obs}} - \alpha A_{j,\text{calc}}) \quad (2.7)$$

97

$$\frac{\partial \alpha}{\partial \gamma_{i,w}} = \frac{(\sum_{a=a_{\min}}^{a_{\max}} A_{\text{obs}} \frac{\partial A_{\text{calc}}}{\partial \gamma_{i,w}} - 2\alpha \sum_{a=a_{\min}}^{a_{\max}} A_{\text{calc}} \frac{\partial A_{\text{calc}}}{\partial \gamma_{i,w}})}{\sum_{a=a_{\min}}^{a_{\max}} A_{\text{calc}}^2} \quad (2.8)$$

98 where $\gamma_{i,w}$ is the i th arbitrary positional variable in the w th direction. The concept
 99 of an "arbitrary positional variable" might seem a bit cumbersome but it allows us
 100 to define the forces for any atomic parameter which can be represented as a vector
 101 in 3-space. This comes in handy when trying to define the forces acting on variables
 102 like anisotropic displacement parameters or atomic magnetic spins.

103 2.3 ENSEMBLES

104 While PESs describe which atomic configurations are the most desirable and how
 105 the atoms would like to get there, the ensemble describes how the atoms move on
 106 the PES. The abstraction of the PES from the ensemble is an important one, as it
 107 allows for the reuse and exchange of both PESs and ensembles for a wide array of
 108 problems. Statistical mechanical ensembles can be described in two ways, analytically
 109 and scholastically. For long simulation times and fine enough numerical or analytical
 110 integration these two descriptions should be identical.

111 In either case one starts by defining the Hamiltonian, \mathcal{H} , as the total energy of
 112 the system. Thus, the Hamiltonian is described as the sum of the potential $U(q)$ and
 113 kinetic $K(p)$ energies, where q is the positions of the atoms and p is their momenta

$$\mathcal{H}(q, p) = U(q) + K(p) \quad (2.9)$$

114 where $K(p) = \frac{1}{2} \sum_i \frac{p_i^2}{m_i}$ and i denotes the i th particle.

115 Analytically one generally defines a partition function, which describes the sum
116 of probabilities over all potential atomic states.

$$\Xi = \sum_i P_i(q, p) \quad (2.10)$$

117 where P_i is the probability of the i th state and is a function of the total energy of
118 that state. This partition function can then be used to obtain the probability of any
119 specific state. The relationship of the probability of a state to the state's energy and
120 other properties depends on the ensemble being used.

121 For the canonical ensemble the partition function is probability is:

$$Q(N, V, T) = \exp\left(\frac{-\mathcal{H}(q, p)}{k_b T}\right) \quad (2.11)$$

122 where k_b is the Boltzmann constant and T is the temperature of the system. [37]

123 Monte Carlo Modeling

124 Monte Carlo can be used to simulate a statistical mechanical ensemble which can not
125 be solved analytically. In most Monte Carlo systems the ensemble is simulated by
126 randomly changing one of the system parameters and comparing the energy of the
127 new system against the energy of the old system. If the energy of the new system is
128 lower than the current energy then the new configuration is accepted. Otherwise the
129 new system is rejected unless

$$\exp\left(\frac{-\Delta E}{E_T}\right) < u \quad (2.12)$$

130 where u is a random number $[0, 1)$ and E_T is the thermal energy characteristic to the
131 system. The ability of Monte Carlo modeling to accept “bad” moves allows the system
132 to hop out of local energy minima during the search for the global minimum. Reverse
133 Monte Carlo (RMC) is similar to Monte Carlo except it uses χ^2 as the PES.[36]

134 Despite the utility of RMC, and its wide use in the x-ray scattering community, as
135 Hoffman and Gelman state “Not all MCMC [Markov Chain Monte Carlo] algorithms

136 are created equal".[24] RMC, similar to standard Monte Carlo simulations, samples
 137 from the PES at random, usually by translating atoms in the system randomly. This
 138 creates a less efficient, random walk based, exploration of the PES.[24, 38] Thus,
 139 methods for suppressing this random walk nature, while still searching the potential
 140 energy surface fully are needed.

141 Hamiltonian Monte Carlo

142 Hybrid or Hamiltonian Monte Carlo (HMC) can help to address some of these issues.
 143 HMC was developed originally in the lattice quantum chromodynamics community
 144 and provides a more efficient, more scalable approach to PES sampling for Monte
 145 Carlo.[15, 39] In HMC the PES is explored using Hamiltonian dynamics, essentially
 146 following the gradient of the PES to find more acceptable configurations.

In order to model dynamics we need to describe the motion of the particles in our system, thus:

$$\frac{dq_i}{dt} = \frac{\partial \mathcal{H}}{\partial p_i} = p_i \quad (2.13)$$

$$\frac{dp_i}{dt} = -\frac{\partial \mathcal{H}}{\partial q_i} = -\vec{\nabla}U \quad (2.14)$$

Using these equations we can derive the position and momentum vectors at any point in time using the leap-frog algorithm:

$$p_i(t + \delta t/2) = p_i(t) - \frac{\delta t}{2} \frac{\partial}{\partial q_i} U(q(t)) \quad (2.15)$$

$$q_i(t + \delta t) = q_i(t) + \delta t * p_i(t + \delta t/2) \quad (2.16)$$

$$p_i(t + \delta t) = p_i(t + \delta t/2) - \frac{\delta t}{2} \frac{\partial}{\partial q_i} U(q(t + \delta t)) \quad (2.17)$$

147 Note that $\frac{\partial}{\partial q_i}$ is the gradient with respect to q where i denotes the i th atom being

148 moved. Using this notation the gradient is

$$\vec{\nabla}U = \begin{bmatrix} \frac{\partial U}{\partial q_{0,x}} & \frac{\partial U}{\partial q_{0,y}} & \frac{\partial U}{\partial q_{0,z}} \\ \vdots & \frac{\partial U}{\partial q_{i,w}} & \vdots \\ \frac{\partial U}{\partial q_{n,x}} & \frac{\partial U}{\partial q_{n,y}} & \frac{\partial U}{\partial q_{n,z}} \end{bmatrix} = \begin{bmatrix} \vec{\mathcal{F}}_0 \\ \vdots \\ \vec{\mathcal{F}}_i \\ \vdots \\ \vec{\mathcal{F}}_n \end{bmatrix} \quad (2.18)$$

149 where $\frac{\partial}{\partial q_{i,w}}$ is the derivative with respect to q where w denotes direction of the deriva-
 150 tive (x , y , or z), n is the number of atoms and U is the potential which depends on q ,
 151 and $\vec{\mathcal{F}}_i$ is the "force" on the i th atom. Using these equations new potential configura-
 152 tions are proposed from the PES. These proposals are checked against the standard
 153 Metropolis criteria discussed above, except that the change in potential energy ΔE
 154 is replaced with the change in the Hamiltonian $\Delta\mathcal{H}$. Note that while this sampling
 155 closely simulates the canonical ensemble, it is not exactly the same. Usually the
 156 canonical ensemble is formulated as microcanonical ensembles in contact with an in-
 157 finite heat bath at a given temperature, or a set of microcanonical ensembles which
 158 exchange thermal energy. However, the HMC ensemble presented here has a momen-
 159 tum bath instead of a temperature bath. One could imagine the atoms sitting in a
 160 simulation box which has walls which can toggle their thermal exchange. Initially the
 161 box starts in the momentum bath, allowing the atoms to come to equilibrium with
 162 the bath momentum. The box is then removed from the bath causing it to become
 163 adiabatic. Hamiltonian dynamics are then propagated inside the box, essentially run-
 164 ning a microcanonical simulation. Once the dynamics are finished the energy of the
 165 system is checked with the Metropolis criteria and the box is reintroduced to the
 166 momentum bath and the process starts again.

167 **No-U-Turn Sampling**

168 Two parameters must be specified in HMC simulations, the step size δ and the number
169 of steps N . The step size is critical to the stability of the fitting procedure: with
170 a too small δ the simulation runs inefficiently producing structures too close to the
171 previous, whereas with a too big δ the linear approximation for the forces breaks
172 down and often the simulated NP explodes. The number of steps to take during the
173 dynamics is equally important and an inappropriate choice may result in backtracking
174 or random walk characteristics in the simulations. In this work, we employ the No-
175 U-Turn Sampling (NUTS) method recently proposed by Hoffman and Gelman to
176 address this issue [24]. In the NUTS method δ and N are dynamically computed
177 by examining the ratio of accepted to rejected configurations as well as whether
178 or not the simulation has started to take a U-turn. The U-Turn criteria makes
179 certain that the simulation stops when it begins to backtrack, preventing excess
180 computation on configurations that have very little new information to offer. The
181 use of NUTS leaves us with two simulation parameters: the simulation temperature
182 and the target acceptance. Hoffman and Gelman have empirically shown that the
183 ideal target acceptance, which governs the dynamics time steps, is .65, which we have
184 used for all of the simulations here. The simulation temperature sets the magnitude
185 of the random starting momenta for the atoms at the beginning of each dynamics
186 run [24].

187 **Grand Canonical Ensemble**

188 While NUTS-HMC simulations provide a system to find minima on PESs, the sim-
189 ulation is fundamentally run in the Canonical Ensemble thus the variables in the
190 simulation are limited to a fixed number of particles, simulation volume, and thermal
191 energy. Fixing the thermal energy and simulation volume is not a problem, as they
192 are not variables of interest in the final structure. However, specifying the number of

193 atoms in the system can be problematic, as the exact number of atoms in a sample
194 can be difficult to count or a sample could have a distribution of particle sizes. Thus,
195 a new ensemble needs to be used to allow the number of atoms to vary as a function
196 of the PES. This new ensemble is the Grand Canonical Ensemble.

197 **Ensemble description**

198 In the Grand Canonical Ensemble (GCE) two sets of variables are allowed to change,
199 the atomic positions, and the total number of atoms and their associated identi-
200 ties. These two variables are controlled by temperature, or average momentum, and
201 chemical potential. The partition function is

$$\Xi = \sum_{N=0}^{\infty} Q(N, V, T) \exp \frac{N\mu\beta}{T} \quad (2.19)$$

202 where $Q(N, V, T)$ is the Canonical partition function discussed above, μ is the chem-
203 ical potential. [37] This is translated into a Monte Carlo system, producing Grand
204 Canonical Monte Carlo (GCMC).

205 **Grand Canonical Monte Carlo**

206 While the probabilities for atomic motion are the same as in the Canonical Ensemble,
207 the addition or removal of an atom have their own probabilities. For the addition of
208 an atom the probability is formally:

$$\min[1, \frac{V}{(N+1)\Lambda(T)^3} e^{-\beta\Delta U + \beta\mu}] \quad (2.20)$$

209 Similarly the removal of an atom has the probability:

$$\min[1, \frac{(N)\Lambda(T)^3}{V} e^{-\beta\Delta U - \beta\mu}] \quad (2.21)$$

210 However, both of these equations depend of the overall simulation volume and the
211 thermal wavelength, which is undesirable as these are not really properties that we
212 are of interest to these simulations. Thus, we roll them into the definition of the

chemical potential, essentially setting the base chemical potential to counteract these effects. This makes certain that our simulation does not change if we change the overall cell volume. A GCMC move consists of creating a new atomic configuration, where an atom has been added or removed, and checking the above criteria. However, previous results have shown that this method is computationally expensive in dense liquids, and exceedingly expensive in solid materials. The long simulation times are due to the random nature of the atomic additions or removals which produce: over-tightly packed atoms, atoms in the middle of nowhere, or nonphysical vacancies. These configurations are rejected by the GCMC criteria but their probability of being sampled is much higher than configurations which are lower in energy, since the number of incorrect ways to add/remove atoms is much larger than the correct ways. Thus, we have implemented methods for biasing the atomic addition positions and the atomic removals toward configurations which are more likely to be accepted.

226 GCMC biasing

The basic idea of GCMC biasing is mapping, in 3 dimensions, where an atomic addition or removal is most likely to be accepted. Thus, the simulation volume is broken up into voxels, 3 dimensional volumes which are contained by the total simulation volume, with a pre-set size. Each voxel is given a probability of being chosen for a trial insertion where the probability is:

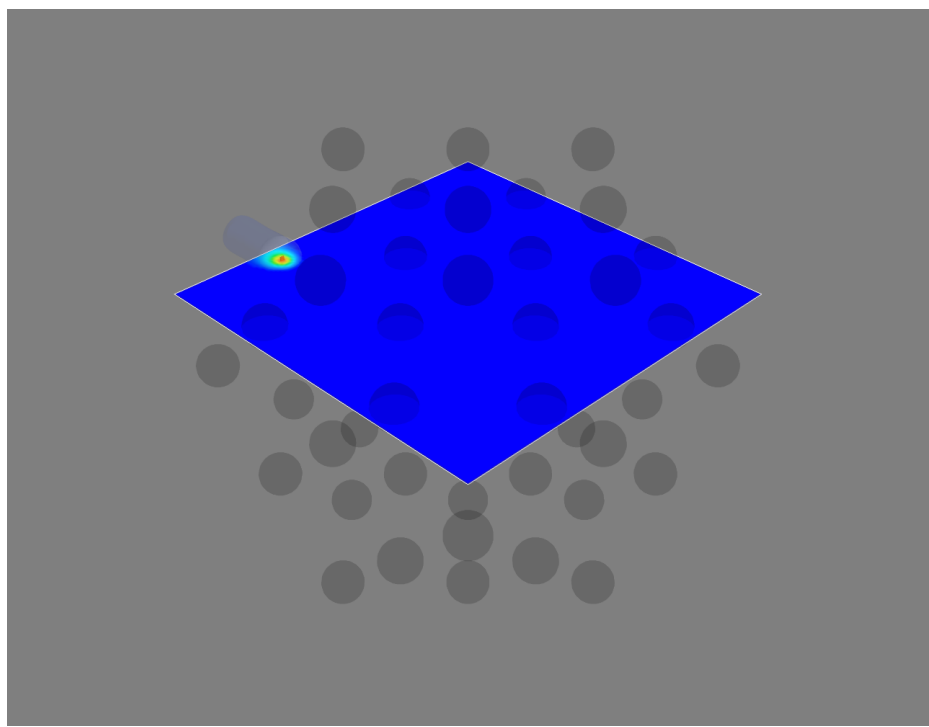
$$P_{i,j,k} = \frac{e^{\beta\Delta U_{i,j,k}}}{\sum_{i,j,k} e^{\beta\Delta U_{i,j,k}}} \quad (2.22)$$

where $\Delta U_{i,j,k}$ is the change in energy. However, calculating $\Delta U_{i,j,k}$ can be particularly expensive, especially when calculating scattering from atomic positions. The computational expense can be mitigated by using a cheaper potential, if only for the evaluation of the voxel energy, as previously shown. Similar to previous work we can use the Lennard Jones potential to approximate the addition potential, lowering the computational burden. [52]

238 Atomic deletion follows a similar biasing procedure, calculating the energy of each
239 atom and biasing the probability of each atom to be chosen for removal by its energy.
240 This way atoms which add the most energy to the system are more likely to be
241 removed.

242 Figure 2.1a shows an example map for atomic addition in a Au54 atom system,
243 with an Au55 atom target. Figure 2.1b shows the results of a few GCMC insertions
244 with biasing, showing the focusing of the simulation on the missing atom. The high
245 density of insertions around the missing atom would not have been possible without
246 the biasing.

(a)



(b)

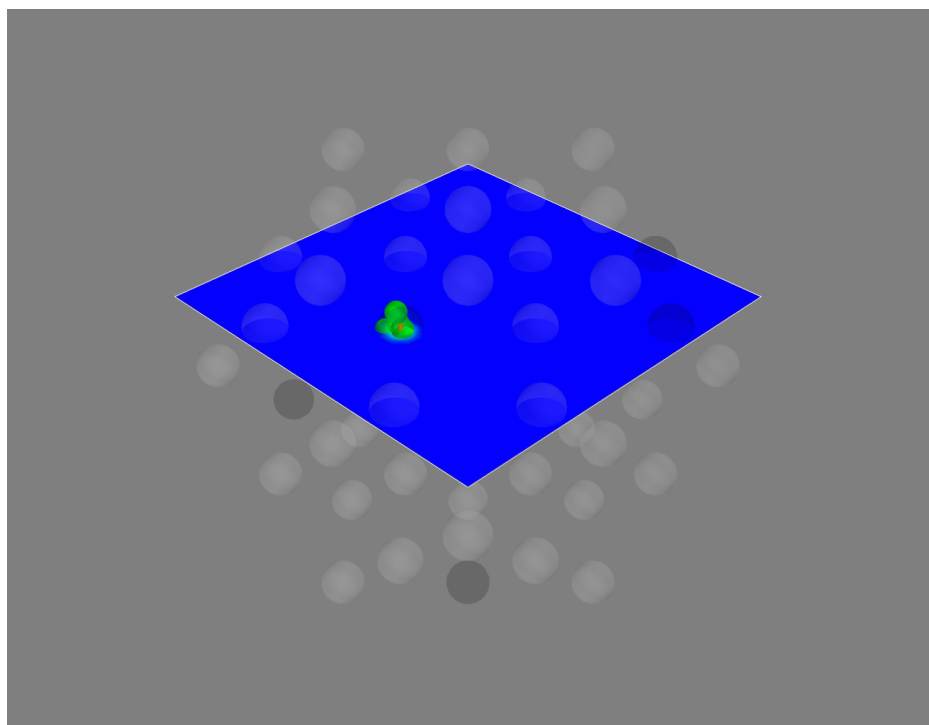


Figure 2.1: These figures show slices of the three dimensional addition potential energy surface. a) shows the addition probability, with the red area most probable. b) shows the results of trial insertions, where the green spheres denote where insertions were attempted.

247 2.4 CONCLUSIONS

248 In this chapter we have presented the development of both PES and the statistical
249 mechanical ensembles used to search them. We expanded the classical concept of
250 a PES to a more general mapping from positional variable space to energy space.
251 This expansion allowed for the implementation of experimentally derived PES, where
252 the disagreement between experimental and computed results can be included in the
253 PES. Common experimental PESs were discussed, and their forces derived. The
254 implementation of various statistical mechanical ensembles, used for searching the
255 PES for minima, was also discussed with a special focus on No-U-Turn-Sampling
256 Hamiltonian Monte Carlo. Grand Canonical Monte Carlo was also discussed, with
257 an emphasis on the us of biasing to increase the overall acceptance rate. Future
258 work in this area may include the development of PESs which leverage 2 dimensional
259 data, like STEM images, or ensembles which help to eliminate tuned parameters like
260 parallel tempering.

261 CHAPTER 3

262 ATOMIC PAIR DISTRIBUTION FUNCTION:
263 THEORY AND COMPUTATION

264 3.1 INTRODUCTION

265 Atomistic structural insight is essential for understanding and controlling a mate-
266 rial's properties and functions, which has led to some of the most exciting advances
267 in modern materials science and engineering. X-ray diffraction techniques are one of
268 the most powerful tools for probing atomic structures with ultimate precision. Tradi-
269 tionally, thousands of diffraction peaks are analyzed using refinements of a structural
270 model with few parameters to determine the 3D structure of bulk single crystals with
271 high precision [21]. However, real engineered materials differ from ideal single crystals
272 by showing a complexity in morphology, crystallite size, and atomic structure. The
273 X-ray Powder Diffraction method (XPD) is among the most widely used methods
274 for solving the structure of micro-crystals. The XPD technique utilizes hundreds of
275 diffraction peaks and constrains the refinement of the structural model to few pa-
276 rameters in order to resolve the structure [42]. Solving the atomic structure becomes
277 difficult using traditional x-ray diffraction techniques when the size of the material or
278 its important features is reduced to the nanometer scale with non-periodic or short-
279 periodic atomic arrangements. Materials consisting of particles with sizes less than
280 a few tens of nanometers, often called nanoparticles (NPs), are structurally more
281 complex than their bulk cousins. This structural complexity is often attributed to
282 the large number of surface atoms which have incomplete coordination spheres [53],

283 surface relaxation [25], and surface environment effects [47, 23, 34]. These effects
284 make the precise determination of 3D atomic structure of NPs far more complicated
285 and problematic [4].

286 Over the years many advances have been made to address the famous “nanostruc-
287 ture problem”[4], for example, by using the atomic Pair Distribution Function (PDF)
288 analysis of x-ray and neutron total scattering data [17, 40, 48], PDF analysis combined
289 with molecular dynamics simulations [56, 22], bulk crystallography approaches [26],
290 and others. Attempts with non-diffraction based approaches have also been made,
291 including Transmission Electron Microscopy (TEM) [12], Raman spectroscopy[29],
292 Extended X-ray Absorption Fine-Structure Spectroscopy (EXAFS)[20] and Nuclear
293 Magnetic Resonance (NMR) [2].

294 In this chapter the PDF and its gradients will be derived. These expressions,
295 when combined with the PES and statistical mechanical treatment from chapter 2,
296 will allow for the solution of atomic structures. This chapter will also develop a
297 computational framework for evaluating the PDF and its gradients using Graphical
298 Processing Units (GPUs) to enable fast structural solution.

299 3.2 THEORY

300 To properly understand the PDF and its limitations we need to derive its mathemat-
301 ics. The PDF has been previously derived many times so it is not re-derived here.
302 This discussion of the PDF and its gradients use the notation of Farrow and Billinge.
303 [18]

304 **Derivation**

305 Many of the above techniques require the gradient of the PES. This in turn requires
306 the gradient of the PDF to be derived. Mathematically treating thermal vibrations
307 will also be discussed in this section. Systems which are truly extended materials, like

308 powders with particle sizes larger than 10nm, are best formulated as systems with
 309 periodic boundaries. Thus, the equations for a periodically bound PDF need to be
 310 developed as well, with their gradients.

311 Analytically Gradients

312 Many optimization algorithms and simulations methodologies, including HMC, re-
 313 quire not only the potential energy of a given configuration but also the forces acting
 314 on that configuration. These forces are described by the gradient of potential energy
 315 of the system which in turn requires the gradient of the PDF. As previously shown the
 316 PDF is the Fourier Transform of the Debye equation. Since the Fourier Transform is
 317 expressed as an integral we can exchange the order of the gradient and the integral,
 318 allowing us to calculate the analytical gradient of the Debye equation and FFT the
 319 resulting function. The Debye equation, with a Debye-Waller vibrational correction
 320 is

$$F(Q) = \frac{1}{N\langle f \rangle^2} \sum_{j \neq i} f_i^*(Q) f_j(Q) \exp(-\frac{1}{2}\sigma_{ij}^2 Q^2) \frac{\sin(Qr_{ij})}{r_{ij}} \quad (3.1)$$

321 where

$$\sigma_{ij}^2 = (\vec{u}_{ij} * \hat{d}_{ij})^2 \quad (3.2)$$

$$\vec{u}_{ij} = \vec{u}_i - \vec{u}_j \quad (3.3)$$

$$\hat{d}_{ij} = \frac{\vec{d}_{ij}}{r_{ij}} \quad (3.4)$$

$$r_{ij} = \|\vec{d}_{ij}\| \quad (3.5)$$

$$\vec{d}_{ij} = \begin{bmatrix} q_{ix} - q_{jx} \\ q_{iy} - q_{jy} \\ q_{iz} - q_{jz} \end{bmatrix} \quad (3.6)$$

322 where Q is the scatter vector, f_i is atomic scattering factor of the i th atom, and r_{ij} is
 323 the distance between atoms i and j and has q dependence. [27] For simplicity's sake

324 we will break up $F(Q)$ so that

$$F(Q) = \alpha \sum_{j \neq i} \beta_{ij} \tau_{ij} \Omega_{ij} \quad (3.7)$$

325 where

$$\alpha = \frac{1}{N \langle f \rangle^2} \quad (3.8)$$

$$\beta_{ij} = f_i^*(Q) f_j(Q) \quad (3.9)$$

$$\tau_{ij} = \exp\left(-\frac{1}{2} \sigma_{ij}^2 Q^2\right) \quad (3.10)$$

$$\Omega_{ij} = \frac{\sin(Qr_{ij})}{r_{ij}} \quad (3.11)$$

326 The derivatives are as follows:

$$\frac{\partial}{\partial q_{i,w}} F(Q) = \alpha \sum_j \beta_{ij} \left(\frac{\partial \tau_{ij}}{\partial q_{i,w}} \Omega_{ij} + \tau_{ij} \frac{\partial \Omega_{ij}}{\partial q_{i,w}} \right) \quad (3.12)$$

327 where

$$\frac{\partial \Omega_{ij}}{\partial q_{i,w}} = \frac{Q \cos(Qr_{ij}) - \Omega_{ij}}{r_{ij}^2} (q_{i,w} - q_{j,w}) \quad (3.13)$$

$$\frac{\partial \tau_{ij}}{\partial q_{i,w}} = \frac{\sigma_{ij} Q^2 \tau_{ij}}{r_{ij}^3} ((q_{i,w} - q_{j,w}) \sigma_{ij} - (u_{i,w} - u_{j,w}) r_{ij}^2) \quad (3.14)$$

328 Since \vec{u}_{ij} is a variable as well, we need the derivative with respect to it as well.

329 Thus

$$\frac{\partial}{\partial u_{i,w}} F(Q) = \alpha \sum_j \beta_{ij} \frac{\partial \tau_{ij}}{\partial u_{i,w}} \Omega_{ij} \quad (3.15)$$

$$\frac{\partial \tau_{ij}}{\partial u_{i,w}} = -\frac{\sigma_{ij} Q^2 \tau_{ij}}{r_{ij}} (q_{i,w} - q_{j,w}) \quad (3.16)$$

330 **Without ADPs**

331 Without ADPs the equations simplify down to

$$F(Q) = \frac{1}{N \langle f \rangle^2} \sum_{j \neq i} f_i^*(Q) f_j(Q) \frac{\sin(Qr_{ij})}{r_{ij}} \quad (3.17)$$

332 and

$$\frac{\partial}{\partial q_{i,w}} F(Q) = \alpha \sum_j \beta_{ij} \frac{\partial \Omega_{ij}}{\partial q_{i,w}} \quad (3.18)$$

333 use of these equations, when ADPs are not appropriate (like at cryogenic tempera-
334 tures), greatly speeds up the computation.

335 Periodic Boundary Conditions

336 Periodic boundary conditions can be helpful when simulating extended solids or large
337 nanoparticles. In this case all the non-crystallinity is contained within the simulation
338 box and the box is repeated to create the longer distance peaks observed in the PDF.
339 To perform this we can break up the Debye equation into two main parts, the part
340 that describes the interatomic distances within the simulation box and those between
341 boxes. Neglecting the thermal motion portion:

$$F(Q) = \frac{1}{N\langle f \rangle^2} \left(\sum_{j \neq i} f_i^*(Q) f_j(Q) \frac{\sin(Qr_{ij})}{r_{ij}} + \sum_{i,j} f_i^*(Q) f_j(Q) \frac{\sin(QR_{ij})}{R_{ij}} \right) \quad (3.19)$$

342 where

$$R = |\vec{r} + \vec{\nu}| \quad (3.20)$$

$$\vec{\nu} = \gamma_1 * \vec{a} + \gamma_2 * \vec{b} + \gamma_3 * \vec{c} \quad (3.21)$$

343 where γ_i is the number of copies of the simulation box in the i th direction, and $\vec{a}, \vec{b}, \vec{c}$
344 are the lattice or superlattice directions.

345 3.3 COMPUTATION

346 Simply deriving the equations for the PDF is not enough. The many body nature of
347 the PDF equation make analytical solution of the structure from the PDF impossible.
348 Thus, the PDF must be computed from a structural candidates and compared against
349 experimental results to evaluate the reliability of the model. These computations were
350 implemented using high performance or high throughput computing methods (HPC
351 or HTC) and Graphical Processing Units to provide quicker solutions.

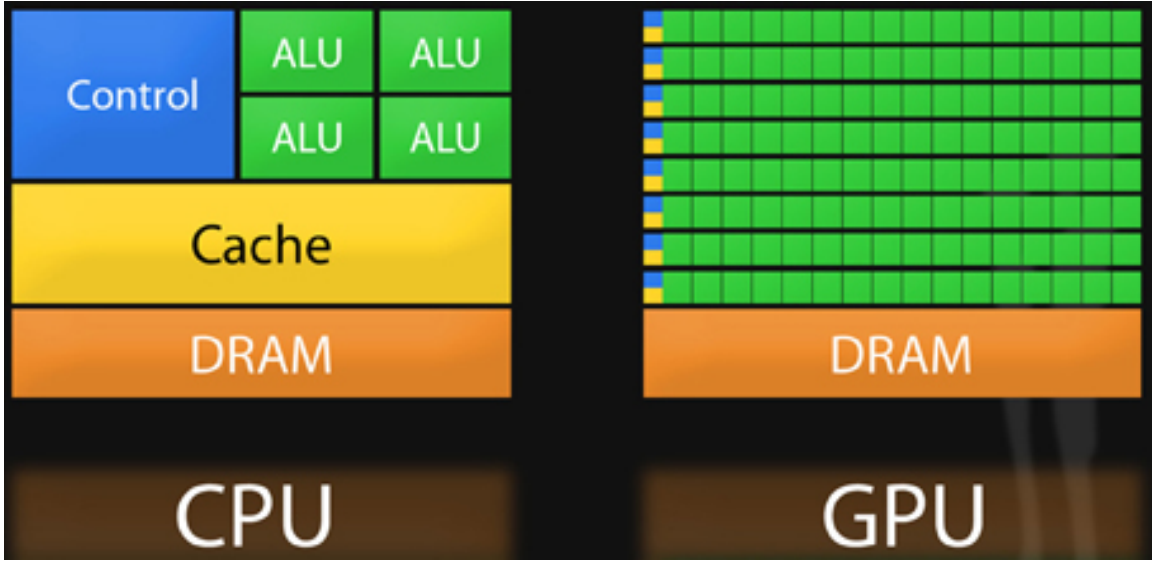


Figure 3.1: Comparison of the central processing unit (CPU) and GPU chip architectures from [6]. The arithmetic logic unit (ALU) are the arithmetic logic units which perform the mathematical operations, the dynamic random-access memory (DRAM) holds most of the data, although it is slower to access, the Cache holds rapidly accessed data, and the Control controls the execution of software. Note the greater number of ALUs on the GPU, the comparatively smaller cache, and the allocation of caches and controls to entire rows of processors.

352 HPC and GPUs

353 To properly solve the structure of materials the PDF will need to be computed many
 354 times and checked against experimental results. This requires computation of the
 355 PDF, potentially over many atoms. Calculating these PDFs requires a fast, highly
 356 parallelized, computational framework.

357 GPUs and Parallelization

358 Computing the PDF is an embarrassingly parallel problem. The basic procedure is
 359 to calculate the reduced structure factor $F(Q)$ for each atom pair and momentum
 360 transfer vector, sum over all the atom pairs, and Fourier transform the structure to
 361 the PDF. The first part of this procedure is perfectly parallelizable, as each atom pair
 362 is separate from the others. The summation over all the atomic reduced structure fac-

363 tors can be parallelized via distributed summing. Lastly the FFT can be parallelized
364 using existing parallel Fast Fourier Transform (FFT) algorithms.

365 Graphical Processing Units (GPUs) are particularly well suited to the task of
366 computing PDFs. GPU chip architecture is designed to perform many task simulta-
367 neously by having potentially thousands of cores. Figure 3.1 show the comparison
368 of CPU and GPU architectures. As the figure shows the GPUs have a very different
369 layout of computational processors (ALUs) and memory. While each ALU is simpler
370 on the GPU, requiring the instructions to be less demanding in terms of memory,
371 there are many more of them. The greater number of processors allows each atomic
372 pairing to be placed on its own processor, so long as the math can be broken into sim-
373 pler operations. The equations are broken up on the GPUs into various pieces which
374 correspond to the α , β , τ and Ω as shown in equations 3.8-3.11 and sub-equations as
375 needed. For example, while β is computed in one step, Ω requires the computation
376 of the displacement array, then the distance array and finally the Ω array. The exact
377 breakdown of processes, how the problems are broken down and spread across the
378 processor has been optimized for speed and reliability.

379 **Map from ij space to k space**

380 The above equations, although formally correct, are very inefficient. $F(Q)$ and its
381 gradient are indexed over all the atoms twice, however there are symmetries that
382 allow us to only compute over the atom pairs essentially mapping from an $n \times n$ space,
383 ij space, to a $\frac{n(n-1)}{2}$ space, k space. For $F(Q)$ we apply the following mapping where

$$\begin{array}{ccccc} E & \xrightarrow{\psi} & E' & \xrightarrow{\Sigma} & Z \\ \phi \downarrow & & & \nearrow \Sigma' & \\ B & \xrightarrow{\psi'} & B' & & \end{array}$$

383

384 E denotes the atomic coordinates in ij space, E' denotes $F(Q)$ before the summation
 385 in ij space, B denotes the atomic pairs in k space, B' denotes $F(Q)$ in k space, and
 386 Z denotes the final summed $F(Q)$. For the operators, ϕ denotes the mapping from
 387 ij space to k space $k = j + i * \frac{i-1}{2}$, ψ and ψ' denote the $F(Q)$ operation in ij and k
 388 space, respectively. Σ denotes the sum over all the atoms.

389 To properly define Σ' we must establish whether $F(Q)$ is an even function. We
 390 can accomplish this by examining each of the portions of $F(Q)$, $\alpha, \beta, \tau, \Omega$. Ω is even,
 391 since r_{ij} is the interatomic distance, which is the same despite a flip of indices, Q
 392 does not depend on the atomic indices, and since Qr_{ij} is even so is $\sin Qr_{ij}$. Thus,
 393 Ω is even. Providing similar analysis to τ we can see that while \vec{u}_{ij} is odd, so is
 394 the unit displacement vector between the two atoms, thus the two odds cancel out.
 395 Intuitively this makes sense, since the $F(Q)$ equation is fundamentally interested
 396 in the interatomic distances which is even. Thus, switching atom indices does not
 397 change $F(Q)$. Due to the even nature of the $F(Q)$ operator the Σ' operator sums
 398 over all the atom pairs, and multiplies by two to reflect the double counting of the Σ
 399 operator.

For the gradient a similar mapping is used:

$$\begin{array}{ccccc}
 & & \psi & & \\
 E & \xrightarrow{\quad} & E' & \xrightarrow{\Sigma} & Z \\
 \phi \downarrow & & & \nearrow \tilde{\phi}\Sigma & \\
 B & \xrightarrow{\quad} & B' & &
 \end{array}$$

400

401 In this mapping, however, we use the $\tilde{\phi}\Sigma$ operator. This operator simultaneously
 402 performs a reverse mapping from k to ij space, and a summation with the correct
 403 symmetry. In this case the ψ and ψ' operators, which denote the $\vec{\nabla}F(Q)$ operator
 404 in ij and k space, are antisymmetric. Intuitively this makes sense as an extension
 405 of Newton's Second Law, since each particle's interaction is felt oppositely by its

406 partner.

407 **GPU Memory Allocation**

408 While GPUs are very fast computational engines they tend to be memory bound.
409 While a gradient array for a 10nm Au nanoparticle, consisting of 31,000 atoms and
410 half a billion unique distances, occupies 1.5 TB of memory a single GPU's RAM
411 allotment varies from 4GB on a NVIDIA GTX970 to 24 GB on a NVIDIA Tesla K80.
412 Thus, it is important to determine exactly how many atoms can fit on a GPU of
413 arbitrary size as a function of the number of atoms and the Q range. The memory
414 required per array is:

$$q[=]3n \quad (3.22)$$

$$d[=]3k \quad (3.23)$$

$$r[=]k \quad (3.24)$$

$$scatter[=]nQ \quad (3.25)$$

$$normalization[=]kQ \quad (3.26)$$

$$\Omega[=]kQ \quad (3.27)$$

$$F_k(Q)[=]kQ \quad (3.28)$$

$$Sum[=]kQ \quad (3.29)$$

$$Sum2[=]kQ \quad (3.30)$$

$$F(Q)[=]Q \quad (3.31)$$

415 where n is the number of atoms, k is the number of unique distances, Q is the scatter
416 vector, and the $[=]$ operator denote the number of single precision floating point
417 values in memory. Each of the above arrays are used in the computation and thus
418 must be able to be held in memory. Thus the number of atom pairs that can fit on

419 a GPU with am bytes of available memory is:

$$k_{perGPU} = \frac{1}{16Q + 16} (-4Qn - 4Q + am - 12n) \quad (3.32)$$

420 If ADPs are included in the calculation, then the following arrays are also added to
421 the memory allocation:

$$adps = 3n \quad (3.33)$$

$$\sigma = k \quad (3.34)$$

$$\tau = kQ \quad (3.35)$$

422 Thus the pair allotment is:

$$k_{perGPU} = \frac{-4Qn - 4Q + am - 24n}{20Q + 20} \quad (3.36)$$

423 For the Gradient we need to calculate $F(Q)$ and its gradient, so the total memory
424 overhead is equal to the previously mentioned arrays plus:

$$\vec{\nabla}\Omega = 3kQ \quad (3.37)$$

$$\vec{\nabla}F_k(Q) = 3kQ \quad (3.38)$$

$$\vec{\nabla}F_n(Q) = 3nQ \quad (3.39)$$

425 Thus the gradient allotment is:

$$\vec{\nabla}k_{perGPU} = \frac{-16Qn + am - 12n}{32Q + 16} \quad (3.40)$$

426 For the gradient with ADPs the ADP gradient array is:

$$\vec{\nabla}\tau = 3kQ \quad (3.41)$$

427 Thus the allocation is:

$$\vec{\nabla}k_{perGPU} = \frac{-16Qn + am - 24n}{48Q + 20} \quad (3.42)$$

428 These equations were solved by sympy as their validity is very important to the overall
429 reliability of the software. If the GPU is over allocated then the system may crash
430 or return meaningless results.

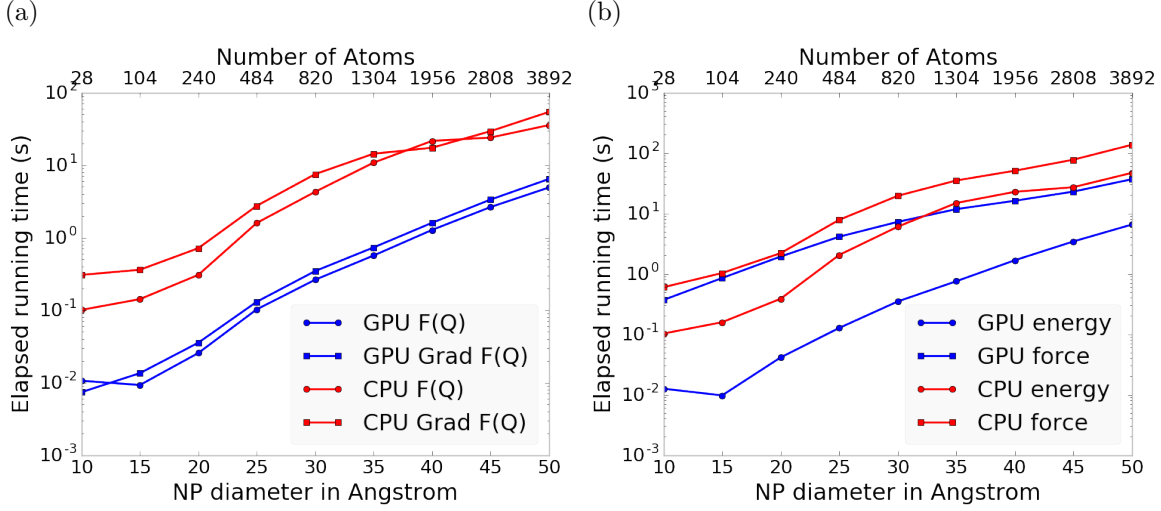


Figure 3.2: Speed comparison of CPU and GPU implementations. a) shows the time to compute the $F(Q)$ by itself. b) shows the time to compute the Rw based energy for Au NPs of various sizes, which includes computing $F(Q)$, its FFT, and the Rw .

431 Speed and Scaling of PDF Computation

432 To understand exactly how much the GPUs speed up the computation of $F(Q)$ and
 433 the PDF a series of time studies were run Au nanoparticles of varying size. Figure
 434 3.2 shows the results of these time studies. CPU and GPU calculations were carried
 435 out on an Intel i7-4820K @3.70GHz Quad-Core and one NVIDIA GTX970s, respec-
 436 tively. The $F(Q)$ computations show a 100x to 10x speedup using the GPUs over
 437 the CPUs. Additionally, the $\vec{\nabla}F(Q)$ and $F(Q)$ computations seem to have similar
 438 computation time and scaling relationships on the GPU. This implies that the two
 439 processes may have similar bottlenecks, most likely in the $F(Q)$ computation work-
 440 flow. This relationship is similarly preserved, although to a lesser extent, in the CPU
 441 scaling.

442 Interestingly, the tight run time relationship between $F(Q)$ and its gradient are
 443 not preserved in the Rw based force calculations. While the energy calculations are
 444 very similar to the $F(Q)$ calculations in terms of run time, the GPU and CPU force
 445 calculations are much closer, with the GPU calculations being much slower. This is

446 due to the force bottleneck being the $3n$ FFT operations which must be performed
447 on the $\vec{\nabla}F(Q)$ array to produce the $\vec{\nabla}\text{PDF}$ array. While the GPU is leveraged
448 to perform the FFT, the data must be loaded off the GPU and back on, causing a
449 potential slowdown. Larger systems of atoms were not tried as the CPU computation
450 quickly becomes very slow. Even higher GPU speedup is expected on more advanced
451 GPUs like the NVIDIA Tesla series.

452 3.4 CONCLUSIONS

453 In this chapter we developed the gradients of the PDF in the discrete and periodic
454 boundary condition case. We also developed the computational implementation of
455 the PDF equations. This implementation emphasized use of GPUs to compute the
456 PDF and its gradient. The GPU software was further sped up by mapping the com-
457 putation to atom pairs rather than atom by atom. Finally, the speed of the GPU
458 implementation was checked against the CPU implementation via speed benchmark-
459 ing.

460

CHAPTER 4

461

BENCHMARKS

462 4.1 INTRODUCTION

463 Having developed the ensemble, PES, and PDF mathematics in chapters 2 and 3 this
 464 chapter will now benchmark the system to check its ability to produce reasonable
 465 structures from PDFs. The benchmarks shown here are certainly not exhaustive, nor
 466 are they even all the benchmarks run against the NUTS-HMC system. However,
 467 they do provide a good window into the workings, limitations, and abilities of the
 468 system.

469 The formation of NPs with both crystallographic and non-crystallographic struc-
 470 tures [34] and with different chemical patterns [19] are well documented. For sim-
 471 plicity, we chose monometallic Au clusters as benchmarks and considered two groups
 472 of structures with different size and degrees of structural disorder in order to assess
 473 the reliability and efficiency of our HMC method for solving atomic structures from
 474 PDFs. The first group consists of Au_{55} clusters with different degrees of disorder,
 475 including a crystalline cluster structure in O_h (Octahedral) symmetry, a structure
 476 with a disordered surface, and an amorphous structure. The second group consists
 477 of the crystallographically solved Au_{102} structure as in the $\text{Au}_{102}\text{MBA}_{44}$ nanocrystals
 478 [26, 33]. We used optimized structures from the Density Functional Theory (DFT)
 479 as target structures and generated the corresponding PDF, G_{obs} , according to

$$G_{\text{obs}} = \frac{2}{\pi} \int_{Q_{\min}}^{Q_{\max}} Q[S_{\text{obs}}(Q) - 1] \sin(Qr) dQ \quad (4.1)$$

480 where S_{obs} is the target structure's structure factor. Since all the target structures

481 were optimized by DFT at zero Kelvin the target and model PDF profiles were
482 calculated at zero temperature, with no atomic displacement parameters (ADPs).
483 However, ADPs would have a considerable impact on the calculation of the PDF,
484 especially for nanoparticles at non-zero temperatures.

485 **Target Setup**

486 Spin-polarized DFT calculations were carried out using the Vienna ab initio simula-
487 tion package (VASP) [32, 31] within the Perdew-Burke-Ernzerhof (PBE) exchange-
488 correlation functional [43]. The projected augmented wave method [5] and a kinetic
489 energy cutoff of 400 eV were used. Structural optimization was performed until the
490 total energy and ionic forces were converged to 10^{-6} eV and 10 meV/Å, respectively.
491 The amorphous Au₅₅ structures were generated by simulated annealing using the
492 classical embedded atom method potential [50]. Different annealing temperatures
493 between 1200 K and 1670 K (bulk melting temperature of Au) were used and the
494 thermally equilibrated structures were cooled down to 300 K before minimization at
495 0 K. Further optimization using DFT leads to total energies that vary within 1-2
496 eV among different amorphous structures and the lowest energy one was used as the
497 target structure. The target structure of Au₁₀₂ was taken as the Au₁₀₂ core of the
498 DFT-optimized Au₁₀₂MBA₄₄ cluster [33].

499 All systems were solved using a PES which consists of a linear combination of
500 Rw , the repulsive and attractive thresholded spring potentials. The total potential
501 energy in the Hamiltonian in Eq. (2.9) is expressed as:

$$U(q) = U_{Rw}(q) + U_{\text{spring}}(q, R_{\min}) + U_{\text{spring}}(q, R_{\max}) \quad (4.2)$$

502 The thresholded spring potentials are based on those previously proposed on by Pe-
503 terson [44], i.e. $U_{\text{spring}}(q, r_t) = \frac{\kappa}{2} \sum_{i,j} (r_{i,j} - r_t)^2$ for all atomic distance $r_{i,j}$ outside the
504 bounds of the spring threshold r_t . The resulting restoring forces on the out-of-bound

505 atoms bring the system back within the bounds of the PDF, R_{\min} and R_{\max} , and
506 therefore preventing the system from exploding or collapsing. Otherwise, incorrect
507 solutions may result by having atomic pair distances out of the PDF bounds. κ is
508 the spring constant in eV/Å and the Rw potential is converted from unitless to eV
509 via multiplication by a conversion factor λ .

510 Whereas the choice of the absolute values of λ and κ is somewhat arbitrary, their
511 relative values are important in determining which term in Eq. (4.2) dominates the
512 PES, especially when considering the effect of the simulation temperature. Generally,
513 the ratio between the total potential energy and the temperature determines how
514 much random motion will dominate the dynamics; a lower ratio implies that random
515 motion will play a large role in the dynamics. The ratio between λ and κ of each
516 spring describes how far the PDF can push the system below or above the bounds set
517 by the spring potentials. Heuristically, too stiff a spring forbids the system to access
518 new configurations, e.g. high energy “transition states” which may involve shorter
519 bonds or a larger system size. Conversely, too small a spring constant makes it slower
520 for the system to snap back within bounds and may lead to an explosion or implosion
521 of the system, leaving the dynamics to drift aimlessly.

522 Model Parameters

523 Unless otherwise stated, the PDFs of the target and starting structures were generated
524 using Eqn. (4.1) with a step of $\delta R = .01 \text{ \AA}$, $Q_{\min} = 0.1 \text{ \AA}^{-1}$, $Q_{\max} = 25.0 \text{ \AA}^{-1}$. R_{\min}
525 and R_{\max} correspond to the first minimum before the first PDF peak and that after
526 the last PDF peak, respectively, which ensure that the full meaningful region of the
527 PDF is modeled. For each of the simulations, the Q resolution was calculated by

$$\delta Q = \frac{\pi}{R_{\max} + \frac{12\pi}{Q_{\max}}} \quad (4.3)$$

528 The HMC simulation was run with $N = 300$ iterations, a target acceptance rate of

529 0.65, and an average starting momentum for each NUTS iteration of 10 eVfs/Å. Both
530 repulsive and attractive spring potentials are used with $\kappa = 200$ eV/Å and thresholds
531 matching R_{\max} and R_{\min} of the PDF, respectively. $\lambda = 300$ eV was used as conversion
532 factor for Rw . Each simulation was run with a pair of NVIDIA GTX970 graphics
533 cards, with one card partially occupied with desktop visualization.

534 4.2 STRUCTURAL SOLUTIONS

535 **Case I: crystalline Au₅₅**

536 We first test our algorithm by solving the crystalline Au₅₅ (*c*-Au₅₅) cluster structure
537 from its PDF. The starting structure is taken as the bulk-cut cuboctahedron of Au₅₅
538 with a uniform bond length of 2.89 Å. Due to finite-size and surface effects, the DFT-
539 relaxed cluster structure shows a distinctively different bond length distribution as a
540 function of the bond's distance to the cluster center of mass, and therefore is difficult
541 to model with a small box approach which assumes an identical unit cell throughout
542 the whole system.

543 R_{\min} and R_{\max} for this simulation were 2.45 Å and 11.4 Å, respectively, with
544 $\delta Q = 0.24$ Å⁻¹. The simulation ran for approximately 34 minutes, over a total of
545 ~40 thousand configurations. The results are shown in Fig. 4.1.

546 The PDF, radial bond distribution, and bond angle distribution show good agree-
547 ment between the target and final fitted structures, with a Rw of 0.3% whereas Rw
548 of the starting structure is as high as 44.8%. DFT calculations yield a total energy of
549 the final structure very close to that of the target structure (within a few meV). The
550 success in the fitting is largely attributed to the factor that the target structure is
551 only locally (and mildly) disturbed from its bulk-like counterpart and therefore there
552 is no need to overcome any high PES barriers to reach the correct solution. As shown
553 below, the situation is rather different for much more disordered target structures.

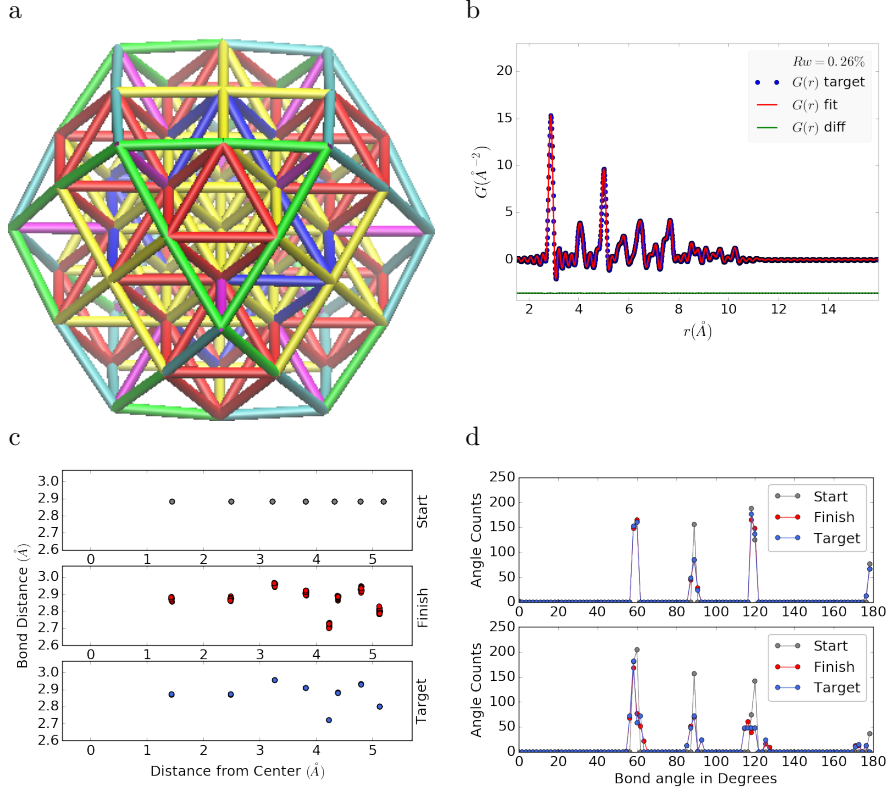


Figure 4.1: Au_{55} PDF fitting of DFT-optimized $c\text{-Au}_{55}$. a) the final structural solution ($Rw=0.3\%$) with bond lengths color-coded by step of 0.05\AA , b) the target PDF(blue dots) overlaid with the PDF of the final structure (solid red lines) with the difference in green lines offset below, c) the radial bond distribution, and d) bond angle distribution.

554 Interestingly, the small-box solution using PDFgui[17] yields a rather large Rw of
 555 43%, due to the failure to fit the surface contracted atoms with a unit cell. The
 556 PDF fits of the starting structure and small-box solution are shown in Fig. S1 in the
 557 Supporting Information.

558 Case II: Au_{55} with surface disorder

559 In addition to surface relaxation, the structure of a cluster or nanoparticle is often
 560 disrupted by the presence of defects and/or ligand bound to the surface. To mimic
 561 such surface disorders, we took the DFT-optimized $c\text{-Au}_{55}$ structure from case I as
 562 the starting structure and randomly displaced the surface atoms with a normal distri-

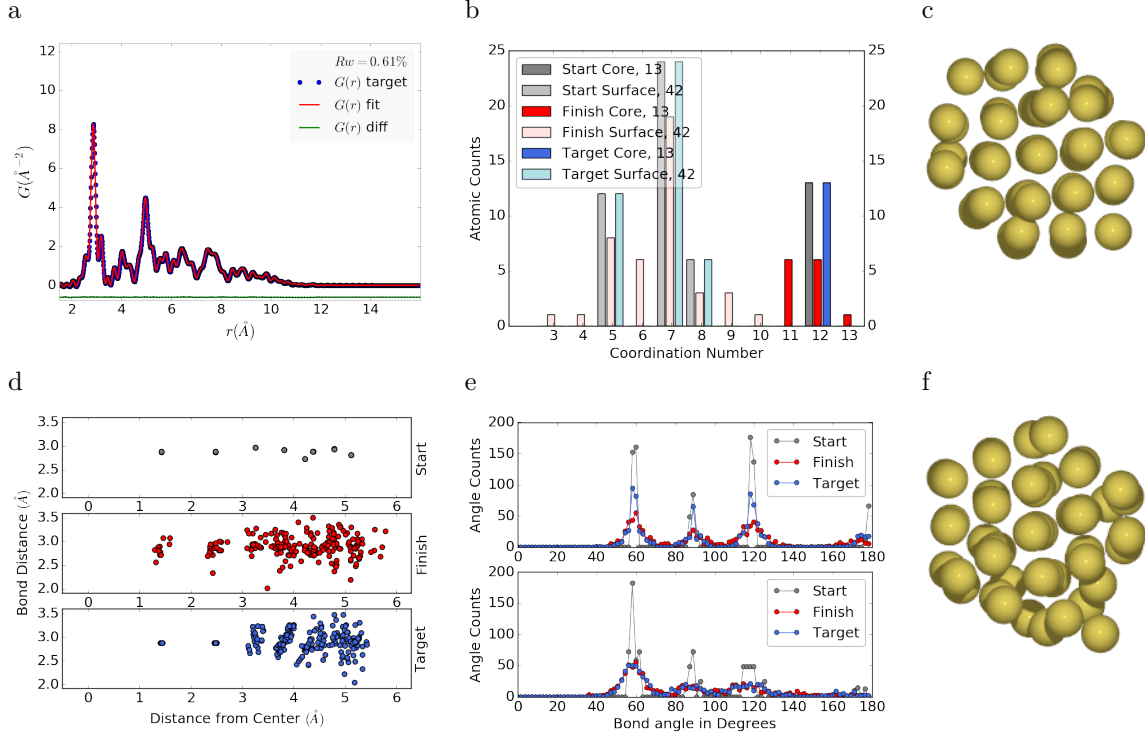


Figure 4.2: Au_{55} PDF fitting of surface-disordered Au_{55} . (a) the comparison of PDFs, (b) the CN distribution, (c) the target structure, (d) the radial bond distribution, (e) the bond angle distribution, and (f) the final structural solution ($Rw=0.6\%$)

563 bution of $\sigma = 0.2 \text{ \AA}$. All atoms are allowed to move in the HMC simulation, including
 564 the originally undisturbed core, which is a Au_{13} cluster with O_h symmetry.

565 R_{\min} and R_{\max} for this simulation were 1.95 \AA and 12.18 \AA , respectively, with
 566 $\delta Q = 0.23 \text{ \AA}^{-1}$. The simulation ran for approximately 3.6 hours, over a total of ~ 270
 567 thousand configurations. The results of the simulation are shown in Fig. 4.2.

568 Overall, good agreement is found between PDFs of the target structure and the
 569 final structural solution, even out to larger r , with an $Rw = 0.6\%$ starting from an
 570 $Rw = 50.4\%$ (see Fig. S2). The radial bond distribution and angle distribution
 571 show reasonably good agreement, but with lower degree of crystallinity in the final
 572 structure compared to the target structure. The discrepancy is most obvious in
 573 the core: despite the identical core structure in the starting and target structures,
 574 the core atoms were displaced in the HMC simulations in order to achieve a “best”

575 solution. This is because PDF measures the global average of interatomic distances
576 between each atomic pair and does not contain direct information about the locality
577 of such pairs, e.g. on the surface or cores. If such information is obtained a priori, for
578 example, from theoretical prediction or other experimental measurements, the core
579 structure can then be fixed and excluded from HMC dynamics.

580 Similar discrepancies are found in the CN distribution. Since the initial displace-
581 ments of the surface atoms are relatively mild, the interatomic connectivities remain
582 more or less the same and therefore the target structure has an identical CN distri-
583 bution to the starting (unperturbed) structure. This is, however, not the case for
584 the final fitted structure, which shows discernible differences, especially at the low
585 and high CN numbers. This is partly caused by the displacement of the core atoms
586 mentioned above, and partly by the lack of CN constraints for the PDF fitting, which
587 has been previously demonstrated in the case of α -Si [10]. Additional experimental
588 data, e.g. from EXAFS or NMR, may help to steer the simulations towards better
589 agreement in both PDF and CN distribution.

590 Case III: amorphous Au₅₅

591 Next, we turn to the case in which the entire cluster structure is disordered. We used
592 a DFT-optimized amorphous Au₅₅ (*a*-Au₅₅) as the target structure, and the DFT-
593 relaxed *c*-Au₅₅ cluster from Case I as the starting structure. The total energy of
594 *a*-Au₅₅ was computed to be *lower* than that of *c*-Au₅₅ by as large as 2.9 eV, consistent
595 with the 3.0 eV found in previous DFT work [13].

596 R_{\min} and R_{\max} for this simulation were 2.6 Å and 11.26 Å, respectively, with
597 $\delta Q = 0.25 \text{ \AA}^{-1}$. The simulation ran for approximately an hour, over a total of ~ 87
598 thousand configurations. The results of the simulation are shown in Fig. 4.3.

599 Our PDF fitting yielded a final structure of Rw of 1.7%, whereas that of the
600 initial structure is as high as 76.1% (see Fig. S3), due to the drastically different

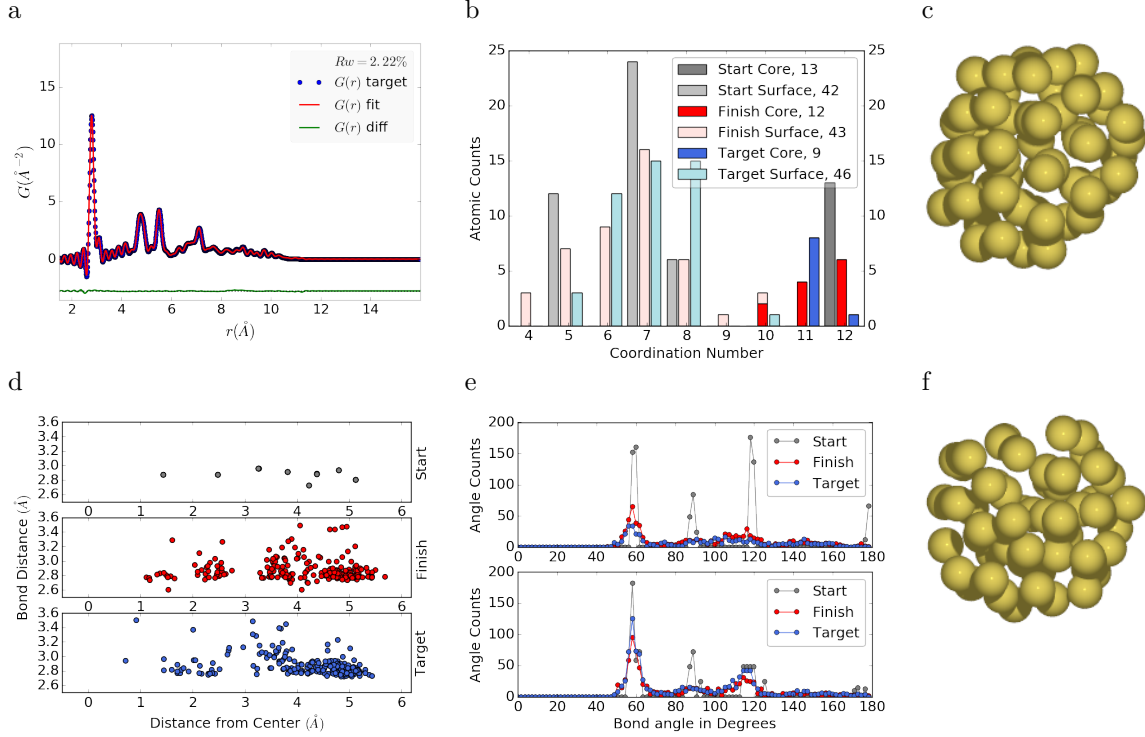


Figure 4.3: Similar to figure 4.2 for DFT-optimized amorphous Au_{55} .

atomic structure of the crystalline and amorphous Au_{55} clusters. Overall reasonable agreement in PDF, bond angle distribution, and radial bond distance distribution was found, and the wide spread of the bond lengths was qualitatively reproduced. However, the mismatch in CNs is problematic, partly due to the lack of information and/or constraints on the CNs. The total energy of the final structure is computed to be ~ 6 eV higher than that of the target structure and the difference is substantially larger than the variation among different amorphous structures computed by DFT ($\Delta E_{\text{tot}} \sim \pm 1\text{-}2$ eV). Such a fitting result, despite the rather small Rw , clearly indicates the importance of complementary information and/or constraints necessary for reliably solving disordered NP structures from PDF.

611 **Case IV: ligand-protected Au₁₀₂**

612 Our final benchmark is Au₁₀₂, whose structure was initially solved by Jadzinsky and
613 co workers using x-ray crystallography [26] and further confirmed by DFT studies
614 [33]. The Au₁₀₂ structure consists of three main parts, a 49-atom Marks decahedron
615 core, two C_5 caps consisting of 20 atoms each, and 13 equatorial atoms. Unlike
616 previous cases, the multi-symmetry nature of the structure, i.e. each part has its own
617 distinct symmetry, poses a challenge for PDF-based solution of the structure. This is
618 because of the atomically centralized nature of the PDF, in which each atom “sees”
619 a density of other atoms surrounding it and has a strong tendency towards becoming
620 the center of the main symmetry group. Such tendency may lead to a solution where
621 some of the correct atomic symmetries are discarded in favor of the core symmetry.

622 **Starting from fcc structure**

623 The starting structure was generated by a spherical cut of the fcc bulk lattice, with
624 two surface atoms removed to conserve the total number of Au atoms.

625 R_{\min} and R_{\max} for this simulation were 2.7 Å and 16. Å, respectively, with $\delta Q =$
626 0.18 \AA^{-1} . The simulation ran for approximately two hours, over a total of ~ 82
627 thousand configurations. The results of the simulation are shown in Fig. 4.4.

628 The initial structure of an fcc bulk-cut cluster, had a starting Rw of 77.6% (see Fig.
629 S4), whereas the final structure has a Rw as low as 8.1%. The disagreement between
630 the final and target PDFs shows that the majority of the error is in the high R region,
631 which is related to the long range distances between the core, caps, and equatorial
632 atoms. The agreement for other structural metrics is less satisfactory. The bond
633 angle distribution for core atoms in the final structure has a poor correlation with
634 those in the target structure, with much broader peak widths. This is likely caused
635 by the high kinetic barrier to change from one high-symmetry core structure (fcc)
636 to another (Marks Decahedron). In contrast, the bond angle distribution for surface

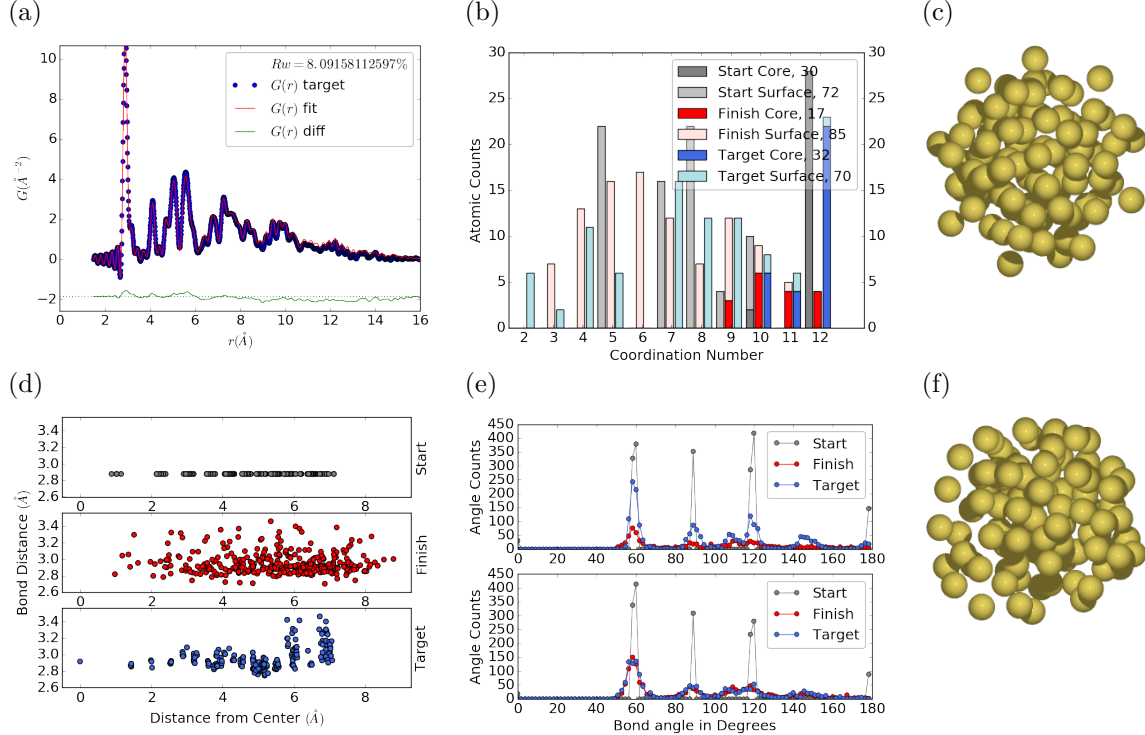


Figure 4.4: Similar to Fig. 4.2 for Au_{102} as in DFT-optimized $\text{Au}_{102}\text{MBA}_{44}$ cluster.

637 atoms, which are of lower symmetry than the core, show a much better agreement.
 638 This is due to the preference of Monte Carlo techniques for higher entropy, and thus
 639 lower symmetry, structures. Similarly, the radial bond distance does not show the
 640 correct clustering of bond lengths as expected from an ordered structure, indicating
 641 the amorphous nature of our fit. Finally, the CN distribution shows the largest
 642 discrepancy at $\text{CN}=12$, again due to the amorphous nature of the fit. Overall, the
 643 structural metrics beyond the PDF indicate the poor agreement between the final
 644 and target structures. A higher simulation temperature, potentially combined with
 645 CN or bond length aware potentials (such as DFT or EXAFS derived PESs) may
 646 help to resolve this discrepancy.

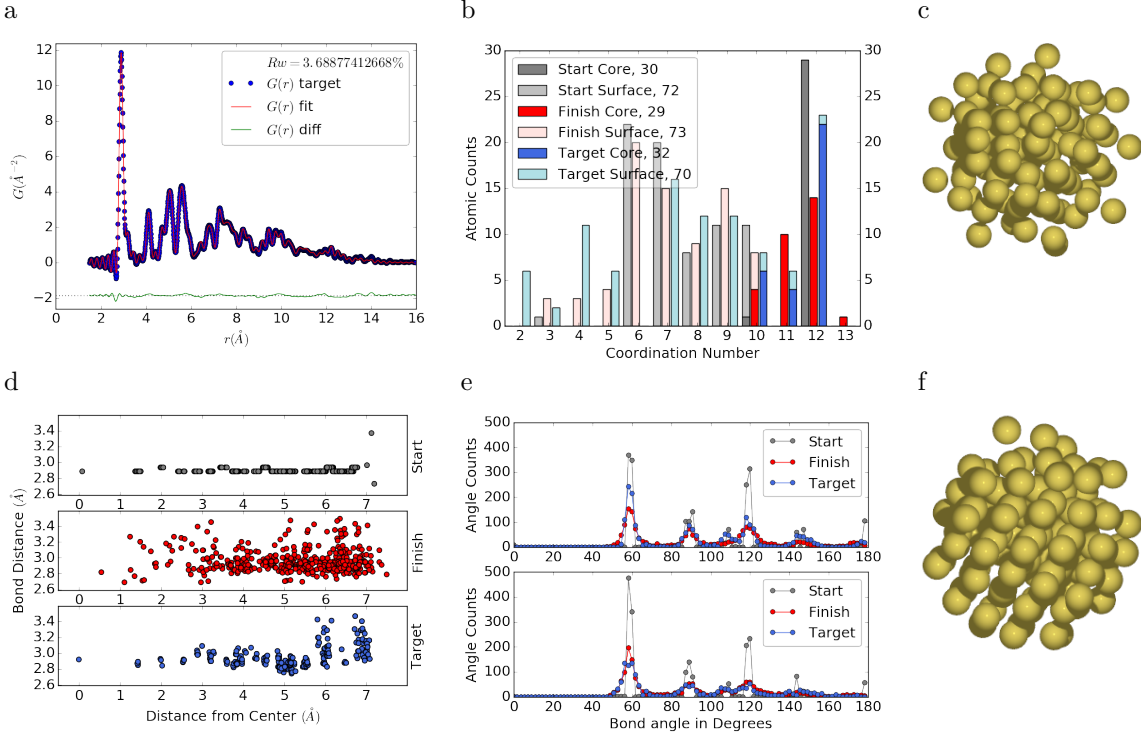


Figure 4.5: Similar to Fig. 4.4 with Marks decahedron as the starting structure.

647 Starting from Marks Decahedron

648 The starting structure, a Marks Decahedron, was generated by the ASE Cluster tool
 649 with 2 atoms on the [100] face normal to the 5-fold axis, 3 atoms on the [100] plane
 650 parallel to the 5-fold axis and, 1 atom deep Marks reentrance. This produced a
 651 structure with 101 atoms which was extended by one more Au atom to fill out the
 652 Au_{102} structure.

653 R bounds and Q resolution were the same as the previous case. The simulation
 654 ran for approximately 2.5 hours over a total of ~ 90 thousand configurations. The
 655 results of the simulation are shown in Fig. 4.5.

656 The starting structure of Marks decahedron ($Rw=56.6\%$, see Fig. S5) yielded
 657 a better structural solution, with a final Rw of 3.3%. However, the discrepancies at
 658 high R remains as in the previous case. By examining the final structure, we can see
 659 that these high R errors are due to a lack of the two 20-atom caps and 13 equatorial

660 atoms. Similarly, the radial bond distance distribution displays a diffusive behavior
661 unlike the bond length clustering in the target structure. Compared to the previous
662 case, the agreement in the CN and bond angle distributions are improved, with the
663 latter capturing nearly all peaks in the target structure with the exception of the 110
664 bond angle. Relatively large discrepancies are found in the CN distribution at the
665 low and high ends.

666 4.3 DISCUSSION AND CONCLUSION

667 The challenge of NP structure determination from X-ray Diffraction stems from the
668 absence of long range atomic ordering and the presence of non-trivial disordered
669 structures. PDF data analysis is one of the successful experimental methods for
670 solving NP structures, which has been tested on varieties of NP structures using
671 non-crystallographic large box hybrid methods [46]. In this work, we developed a
672 novel, HMC-based method to solve the structures of NPs from PDFs. We chose
673 monometallic Au clusters as benchmarks and generated synthetic experimental PDF
674 data from DFT-optimized cluster structures. Two cluster sizes (Au_{55} and Au_{102})
675 and different degree of disorders (crystalline, surface disordered, amorphous, ligand-
676 protected) were considered, which pose further challenges in addition to the lack of
677 long-range order in finite-size systems.

678 The quality of the PDF fit, as measured by the agreement factor Rw , is expected
679 to provide a basis for the comparison between the fit structure and the target struc-
680 ture. The HMC method is designed to find minima in the Rw PES and therefore the
681 ultimate criterion for its success is the magnitude of the Rw values. This criterion has
682 been met in the cases of surface relaxed $c\text{-}\text{Au}_{55}$, surface distorted-Au55, and $a\text{-}\text{Au}_{55}$
683 systems, where we obtained an excellent fits with $Rw < 2\%$. With most of the mod-
684 eling methods a PDF fit with an $Rw < 15\%$ would be considered a solved structure
685 [46, 1, 35, 51, 45]. However, a low Rw does not necessarily translate into the correct

686 structural solution and the discrepancies may be caused by several different factors.
687 For example, the disordered surfaces associated with NPs produces a fall off in the
688 PDF profile, resulting in underestimated NP sizes in the fitted structures [46]. In ad-
689 dition, as the PDF profile depends on the average core and surface pair distributions,
690 the structural solution may not be unique especially for disordered systems. This is
691 best manifested in the example of amorphous Au₅₅, in which the final structure pro-
692 duces a rather small R_w but has distinctively different structural features and a much
693 higher total energy compared to the target structure. In order to faithfully solve the
694 structures, other fitting metrics, such as the atomic coordination numbers, may need
695 to be considered. For ordered or partially ordered systems, we have demonstrated
696 a reasonable agreement between the final and target CN distributions, whereas the
697 discrepancy increases for disordered structures. A hybrid HMC method combining
698 with other experimental (EXAFS, NMR) or computational (DFT, force field) meth-
699 ods is expected to provide more physical constraints, e.g. CN distribution, in the
700 PDF fitting and result in better structural agreement.

701 The case of ligand-protected Au₁₀₂, a crystallographically well solved NP system
702 by X-ray diffraction, provides a unique test for the HMC algorithm due to its multi-
703 symmetry nature and very short range ordering. The structure of Au₁₀₂ was solved
704 using two different starting crystal structures, i.e. fcc and Mark decahedron. The R_w
705 values support the Marks decahedron structure of the cluster core over the fcc one,
706 but discrepancies are found at high R values. This could be explained as limitation
707 of the method while using PDF profile fit for high symmetry local structures such
708 as cap atoms in Au₁₀₂, which has a C_5 symmetry. This is an intrinsic problem with
709 the PDF, which measures the global inter-atomic distances, thus causing each atom
710 to see itself at the epicenter of the majority symmetry. Use of additional techniques,
711 like EXAFS, which has an emphasis on the local coordination spheres, may help
712 with finding better minima by breaking the dominant symmetry and providing a low

713 energy path to compartmentalized structures.

714 In summary, we present the development of a novel Hamiltonian Monte Carlo
715 based method for finding atomic structure solutions to PDFs. We derived the ana-
716 lytical derivatives of Rw , $G(r)$, and $F(Q)$, which were used to guide the Hamiltonian
717 dynamics to follow the gradient of the PES towards minimum energies. The ma-
718 trix element algebra inherent to the Debye sum and its derivatives lent itself to be
719 written as GPU kernels, allowing for the speedup of the HMC algorithm by massive
720 parallelization. The GPU implementation is 100 to 4x faster than the comparable
721 multi-core CPU enabled code, depending on the size of the NP. The robustness and
722 accuracy of the HMC method was benchmarked against a set of Au cluster struc-
723 tures of different size and degree of disorder. Overall, low Rw values were obtained
724 for all the benchmarks, with most of the structural features reproduced as shown by
725 various structural metrics. The Au_{102} cluster, which contains both high symmetry
726 local structures and disordered surface regions, posed the largest challenge. Although
727 the fitted structure shows some dependence on two starting configurations, neither
728 of them was able to fully solve the target structure. Future work which employs ex-
729 perimentally derived potentials, including EXAFS, or computational potentials that
730 contain chemical bonding information, may help to solve these particularly difficult
731 cases. Work is underway to extend this method to the grand canonical ensemble and
732 parallel tempering, which will allow for solving structures with unknown number of
733 atoms and compositions and provide better stochastic mixing of structures.

734

CHAPTER 5

735

X-RAY TOTAL SCATTERING DATA ACQUISITION AND PROCESSING

737

5.1 INTRODUCTION

738 X-ray total scattering experiments are generally performed at synchrotron light sources,
739 as only these sources can provide the needed flux, energy, and high momentum trans-
740 fer vectors needed to obtain reliable PDFs. [9, 16] Despite the need for a dedicated
741 facility to perform the total scattering experiments, the experiments themselves are
742 fairly forgiving, allowing for reactive gaseous environments, experiment temperatures
743 ranging from 2 K to 1800 K, and even electrochemical cycling. [8, 47, 49] The rapid
744 PDF data acquisition associated with 2D area detectors creates a data management
745 problem, as 96 hours of beamtime could result in almost 10,000 images which need
746 to be associated with the experimental conditions and detector metadata. [9] Finally,
747 all this data needs to be processed by masking bad pixels and regions, integrating
748 azimuthally, and converting the scattering data to the PDF. [30, 28, 54, 41, 3]

749

5.2 DETECTOR Q RESOLUTION

750 To properly azimuthally integrate the images taken from the detector the Q resolution
751 of the pixels must be calculated. Azimuthal integration is the process of dividing the
752 pixels up into “bins”. Each bin has a set width, usually in Q , which describes which
753 pixels can go into the bin. During the integration process each pixel is placed into
754 its corresponding bin. Finally a statistical measurement of the average of all the

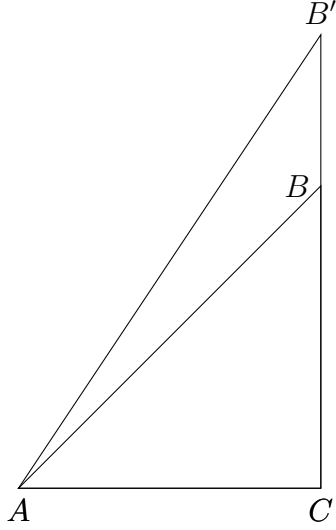


Figure 5.1: Scattering onto a flat detector

pixels in each bin is taken to produce the $I(Q)$ data. Although commonly performed, integrating using evenly spaced bins will cause pixels which are not on the same ring to be binned together, causing the incorrect value of $I(Q)$ to be obtained and a larger standard deviation in the integrated data. To properly calculate the Q resolution the resolution of each of the pixels in 2θ must be calculated. Figure 5.1 shows the scattering of x-rays onto a flat image plate detector. In this diagram the bottom of the n th pixel is B while the top is B' . The resolution of this pixel in 2θ is $\angle BAC - \angle B'AC$. Thus the resolution, calculated from the distances is

$$\Delta 2\theta = \arctan \frac{b}{d} - \arctan \frac{t}{d} \quad (5.1)$$

where d is the sample to detector distance (AC in figure 5.1), b is the distance to the bottom of a pixel (CB in figure 5.1)), and t is the distance to the top of that pixel (CB' in figure 5.1)). Note that these distances need to have been corrected for detector tilt and rotation. Thus the resolution of a pixel in Q is

$$\Delta Q = \frac{4\pi(\sin \arctan \frac{b}{d} - \sin \arctan \frac{t}{d})}{\lambda} \quad (5.2)$$

where λ is the x-ray wavelength.

768 This effect is analogous to looking at windows on a very tall building. The windows
769 are all the same size, but due to the nature of the perspective, the windows seem to
770 shrink as one looks higher up the building.

771 For a Perkin Elmer image plate, like the one used at the NSLS-II's XPD and the
772 APS's 11-ID-B, the resolution function is shown in 5.2. For the same detector the
number of pixels per Q is shown in 5.3

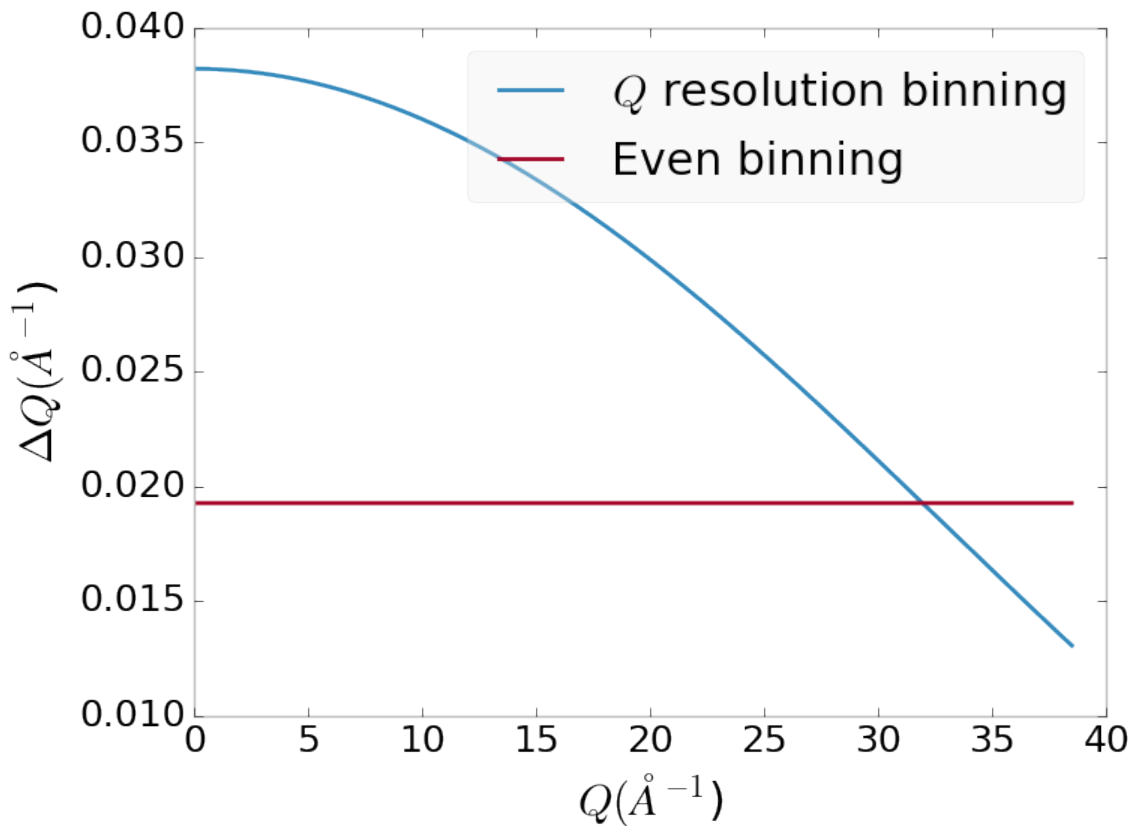


Figure 5.2: Q resolution as a function of Q .

773

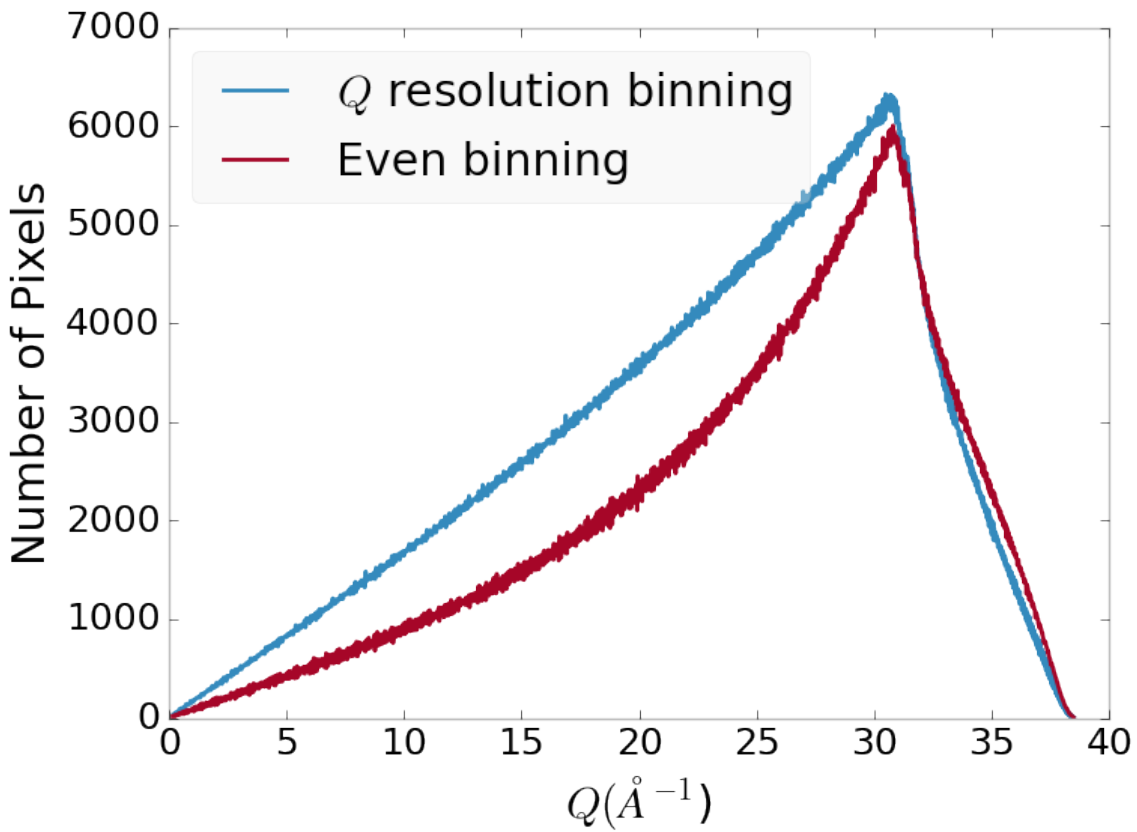


Figure 5.3: Number of pixels as a function of Q , binned at the Q resolution of the detector.

774 5.3 AUTOMATED MASK GENERATION

775 **Introduction**

776 Detector masking is an important part of any x-ray scattering workflow as dead/hot
 777 pixels, streak errors, and beamstop associated features can be averaged into the data
 778 changing the signal and its statistical significance. While some features, like the
 779 beamstop holder, can be easily observed and masked by hand other are much more
 780 difficult to observe even on large computer monitors. Additionally, while dead/hot
 781 pixels and streaks are usually static the hot pixels associated with textured or sin-
 782 gle crystal scattering or cosmic rays are not. Thus, coming up with an automated
 783 method for finding such erroneous pixels is important, especially as high flux diffrac-

784 tion beamlines can generate data very quickly.

785 While this problem can be quite complex in the most general case, we can use the
786 annular symmetry of the powder scattering pattern to our advantage, by comparing
787 a pixel against pixels in the same ring. Since non-textured powder scattering should
788 produce the same pixel intensity for a given ring we can mask any pixels which are α
789 standard deviations away from the mean. This method relies on the aforementioned
790 pixel binning algorithm, as using miss sized bins will cause some pixels which should
791 be in separate rings to be put together, and others which should be in the same ring
792 to be separated. In that case the masking algorithm will overestimate the number of
793 pixels to be masked due to the additional statistical variation in the sample.

794 **Algorithm Design**

795 The masking algorithm procedure takes in the image and a description of the pixel
796 positions in either distance from the point of incidence or in Q . The image is then
797 integrated twice, producing both the mean $I(Q)$ and the standard deviation of each
798 $I(Q)$ ring. The mask is created by comparing the pixel values against each ring's
799 standard deviation and threshold α . Note that the threshold can be a function of
800 distance from the point of incidence or Q .

801 **Test Cases**

802 To study the effectiveness of the masking we ran the algorithm against both simulated
803 and experimental data. In the case of the simulated data four systems were created:
804 1) dead/hot pixels with varying numbers of defective pixels, 2) beamstop holder with
805 varying beamstop holder transmittance, 3) rotated beamstop holder with varying
806 beamstop holder transmittance, and 4) beamstop holder with dead/hot pixels. The

807 base scattering was produced by

$$I = 100 \cos(50r)^2 + 150 \quad (5.3)$$

808 where r is a pixel's distance from the beam point of incidence. The positions of
809 the dead/hot pixels were chosen at random as was the dead or hot nature of the
810 defect. Dead pixels had values from 0 to 10, while hot pixels had values from 200
811 to 255. The beamstop was positioned at the vertical center of the detector with an
812 initial width of 60 pixels and final width of 120 pixels. The height of the beamstop
813 was 1024 pixels. The beamstop was calculated to attenuate the x-ray scattering
814 signal at various transmittance, as various beamstop holder materials have different
815 transmittance. Two version of the masking algorithm were run for each test case, one
816 using the standard even bin sizes for the integration step, and one where the bin sizes
817 are tuned to the pixel Q resolution as discussed in 5.2.

818 Results and Discussion

819 Three main studies were run each examining a different aspect of the simulated
820 or experimental studies. These included, masking bad pixels, masking a beamstop
821 holder, and masking experimental data. Figures 5.4-5.11 show the results of the
822 masking algorithm on simulated images. The dead/hot pixel masking shows the
823 importance of using the Q resolution based bin sizes as the even bin based mask have
824 a tendency to over mask the image, removing pixels which contain valuable signal.
825 This over-masking is caused by pixels being improperly associated with one another
826 by the even bins. Figure 5.4 indicates that the masking algorithm, with the proper
827 binning, masks the image perfectly, with no missed bad pixels or good pixels masked.
828 This is not the case in figures 5.5 - 5.7 as we can see pixels which should have been
829 masked but were not. Despite these missed pixels no pixels were improperly masked
830 in any of the well binned images. These test cases are actually more difficult than

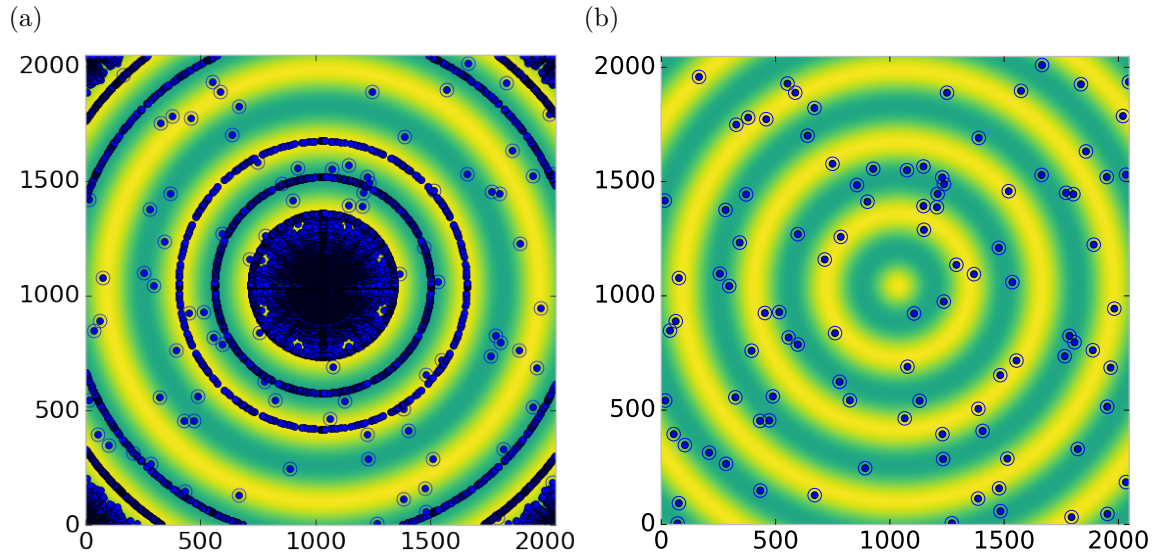


Figure 5.4: Generated dead/hot pixel masks for a detector with 100 bad pixels. a) the standard even bin mask and b) the Q resolution binned mask. The bad pixels are noted with open circles, masked pixels are noted with solid circles.

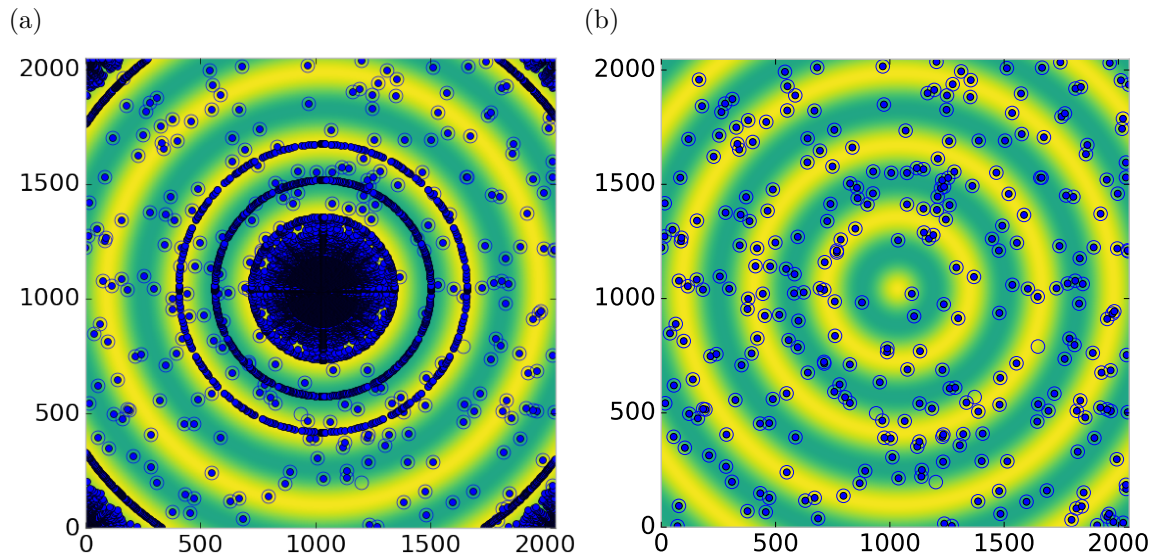


Figure 5.5: Generated dead/hot pixel masks for a detector with 300 bad pixels. a) the standard even bin mask and b) the Q resolution binned mask. The bad pixels are noted with open circles, masked pixels are noted with solid circles.

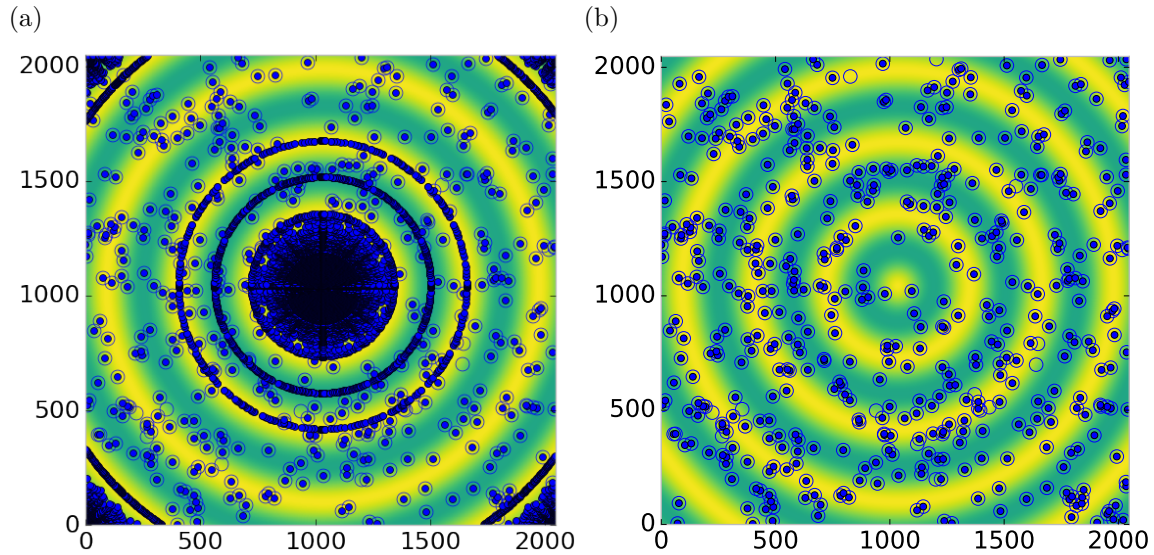


Figure 5.6: Generated dead/hot pixel masks for a detector with 500 bad pixels. a) the standard even bin mask and b) the Q resolution binned mask. The bad pixels are noted with open circles, masked pixels are noted with solid circles.

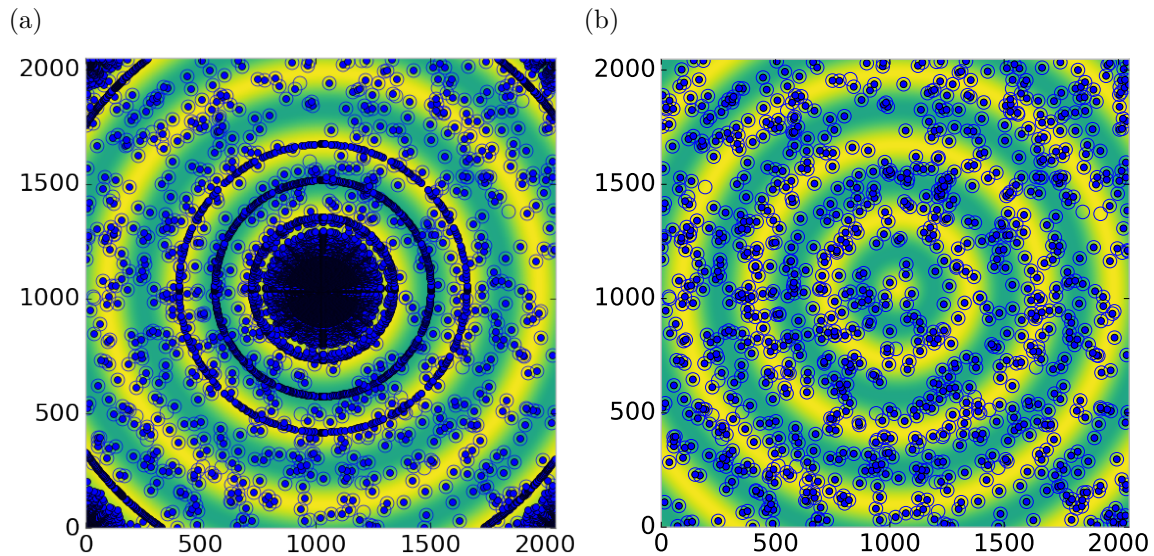


Figure 5.7: Generated dead/hot pixel masks for a detector with 1000 bad pixels. a) the standard even bin mask and b) the Q resolution binned mask. The bad pixels are noted with open circles, masked pixels are noted with solid circles.

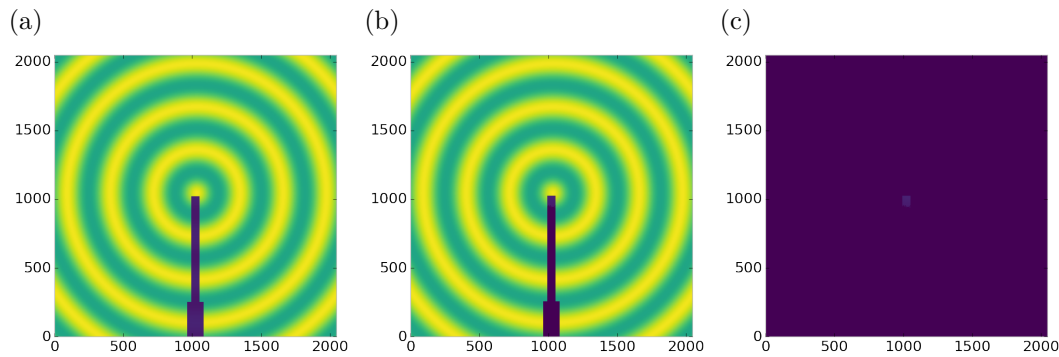


Figure 5.8: Generated beamstop holder masks for a beamstop holder with 10% transmittance. a) the raw image, b) the masked image, c) and the missed pixels

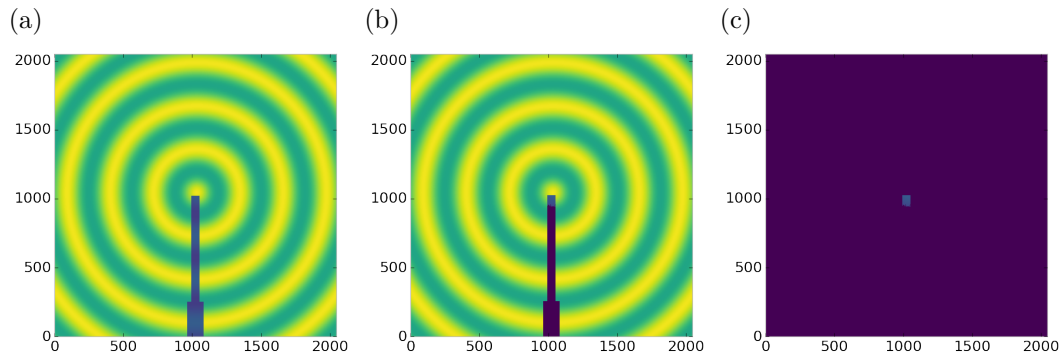


Figure 5.9: Generated beamstop holder masks for a beamstop holder with 30% transmittance. a) the raw image, b) the masked image, c) and the missed pixels

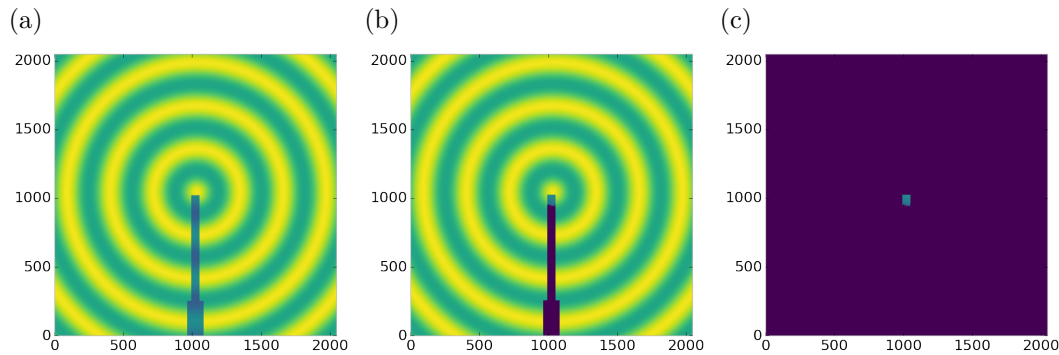


Figure 5.10: Generated beamstop holder masks for a beamstop holder with 50% transmittance. a) the raw image, b) the masked image, c) and the missed pixels

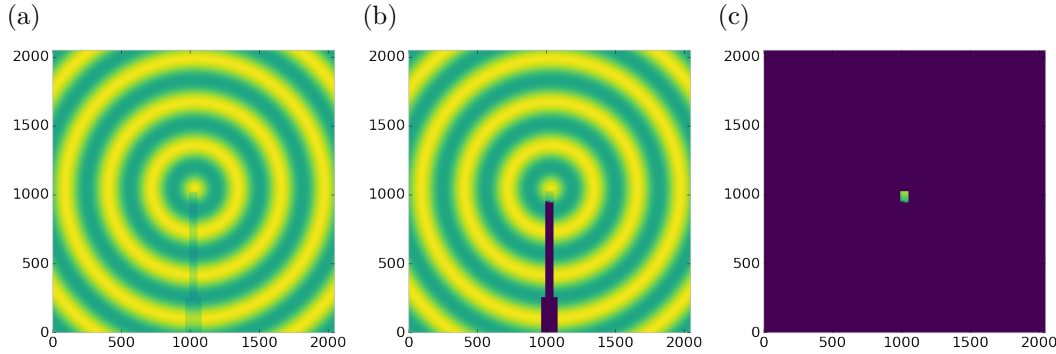


Figure 5.11: Generated beamstop holder masks for a beamstop holder with 90% transmittance. a) the raw image, b) the masked image, c) and the missed pixels

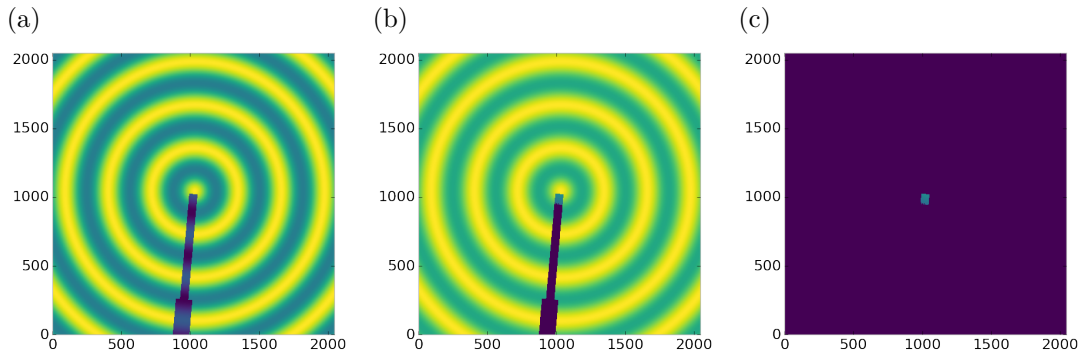


Figure 5.12: Generated beamstop holder masks which is rotated away from vertical

831 experimental data, as the dynamic range of most detector causes the dead/hot pixels
 832 and single crystal/texture peaks to be orders of magnitude away from the desired
 833 signal.

834 The beamstop holder masks shown in figures 5.8 - 5.11, which were all run with
 835 the Q resolution binning show similar results across the transmittance range, missing
 836 only a small part of the beamstop holder near the point of incidence. Near this point
 837 the beamstop holder becomes a statistically significant part of the total number of
 838 pixels in a given ring, thus it can not be masked out using a statistical search of the
 839 rings. For most PDF and XRD studies this small area can be masked automatically
 840 by masking all the pixels who's distance from the point of incidence is smaller than a
 841 given radius r , or can be neglected outright as the area is not used in the analysis or
 842 refinement. Similar results were produced for beamstop holders which were rotated

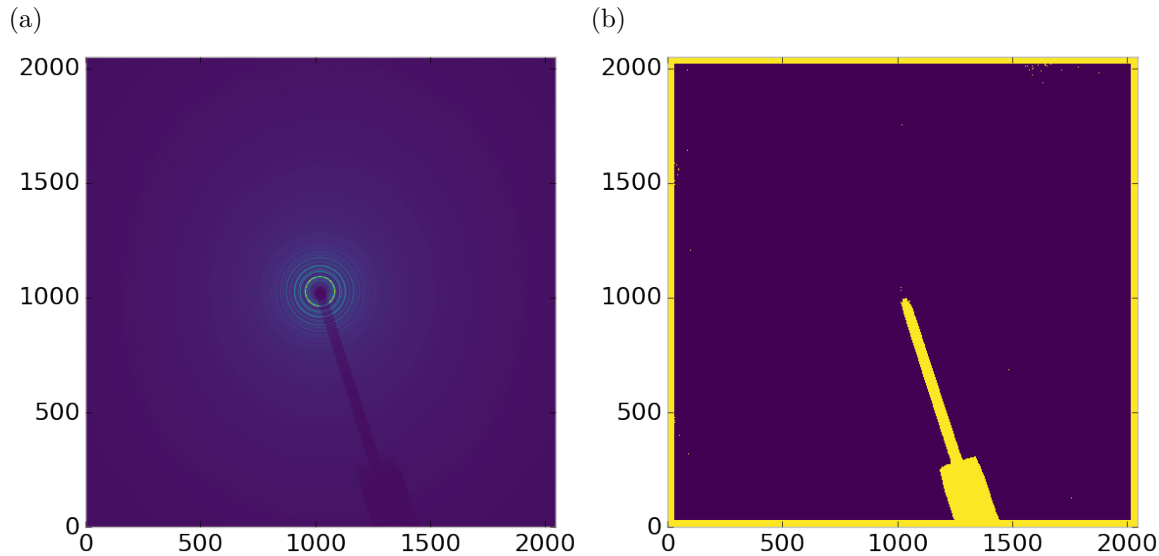


Figure 5.13: Masked experimental data. a) the raw image, b) the mask

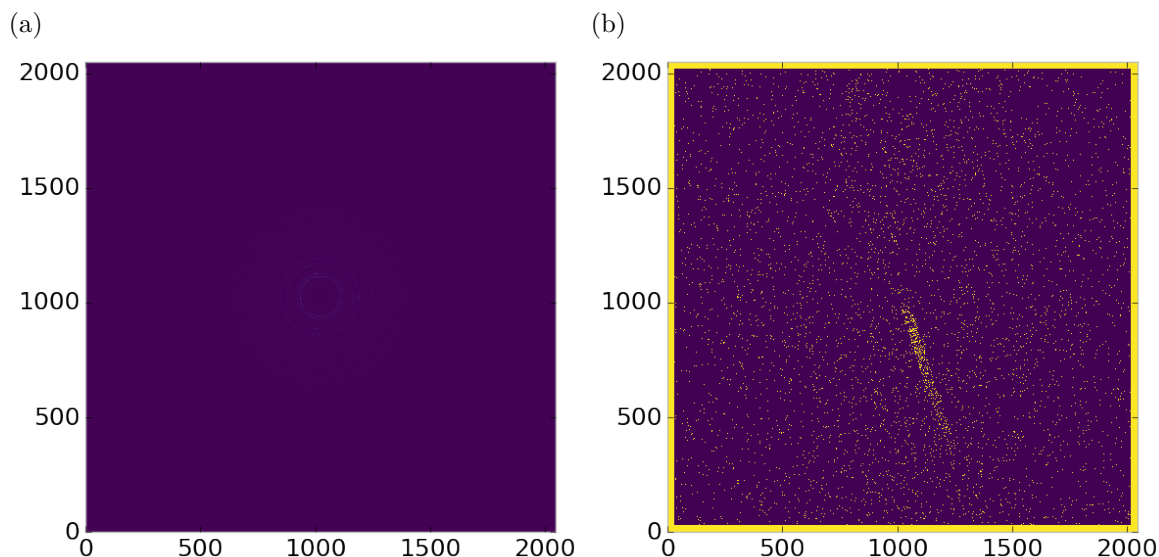


Figure 5.14: Masked experimental data with Pt single crystal signal. a) the raw image, b) the mask

843 away from the vertical position, as shown in figure 5.12

844 Working with actual experimental data, obtained at the Advanced Photon Source
 845 beamline 11-ID-B, shows the difficulty of masking images which have low photon
 846 counts. While the masking of experimental data taken with longer exposures, con-
 847 sisting of 250 .2 second shots, shown in figure 5.13 provides very sharp edges to the

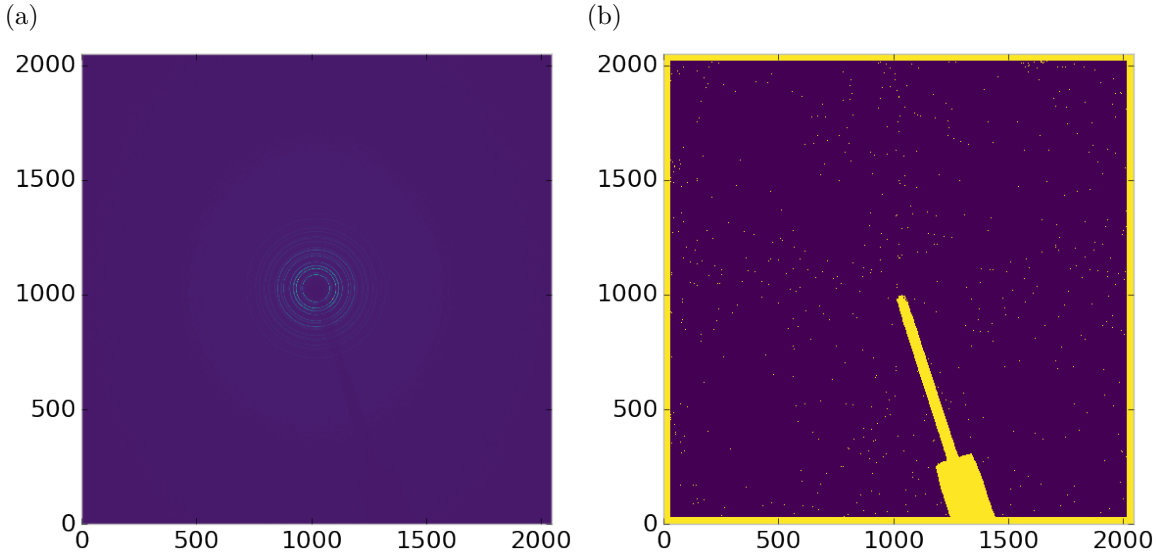


Figure 5.15: Masked experimental data with Pt single crystal signal using figure's 5.13 mask as a starting mask. a) the raw image, b) the mask

beamstop holder, and very little extra masking beyond the occasional dead pixel, this is not the case for the single crystal data. The single crystal data is more problematic because of its short exposure time and low flux, with 500 frame at a .1 second exposure and having shrunk the beam size. The low flux is to prevent the very strong single crystal peaks from damaging the detector. However, this causes the image to be less statistically viable than ideal, causing problems with the mask as seen in figure 5.14. This can be alleviated to some degree by using the previously generated mask as a starting mask for the single crystal image, as shown in 5.15. While the masking algorithm still produces many diffuse masked pixels, they are far fewer, this may be due to the removal of the beamstop which could have contributed to the large standard deviation in figure 5.14.

Conclusions

In this section the masking algorithm, which relies on both Q resolution based binning and a statistical approach to azimuthal symmetry, was developed. The focus of

862 this algorithm was to remove many unwanted detector features associated with pixel
863 defect, beamstop holder associated scattering attenuation, and single crystal/texture
864 peaks. Simulated data was used to evaluate the beamstop holder and dead/hot pixel
865 masking capacity, while experimental data was used to check for single crystal and
866 texture based masking. Q resolution based binning was shown to be very important
867 to avoid over-masking. The ability of the mask writer to mask images is somewhat
868 limited by the overall statistical image quality, although some deficiencies can be
869 obtained by using previously generated masks as starting points. This masking algo-
870 rithm is now in use in the data processing workflow and will be available in scikit-beam
871 soon.

872 5.4 AUTOMATED IMAGE AZIMUTHAL INTEGRATION

873 Using the Q resolution binning and masking developed in sections 5.2 and 5.3 the
874 images can be properly integrated. Generally, images are integrated by taking the
875 mean value of the pixels in a ring. However, other statistical measures of the average
876 value can be used, like the median. Note that all the integrations done here use the
877 pixels as they are, without pixel splitting, minimizing the covariance of the resulting
878 $I(Q)$.[54]

879 Figures 5.16-5.18 show the importance of masking and the choice of average func-
880 tion. All the figures were produced using the same dataset, 50 °C Pr_2NiO_4 taken at
881 the APS’s 11-ID-B on a Perkin Elmer area detector. The automatic masking alpha
882 was 3 standard deviations from the mean. While it is difficult to observe the changes
883 the mask causes in the full $I(Q)$ plot (subfigures a) and b)), the standard deviation
884 plots show the effect of bad pixels on the data (subfigure c)). Subfigure c) for figures
885 5.16-5.18 shows that removal of the beamstop holder lowers the low Q standard de-
886 viation from around .1 to almost .01 out to 15 \AA^{-1} . The high Q subfigures d) and f)
887 in figures 5.16-5.18 show the “kink” effect of the detector edge and beamstop holder,

888 where there is a dip in the $I(Q)$ scattering when the rings include the edge of the
889 detector. This effect seems to be due to both errors in the edge pixel intensity and the
890 beamstop holder as masking of the edges only seems to provide only partial removal
891 of the issue. It is important to note that while integration using the mean of the
892 ring has issues with only the edge mask, as evidenced by the change in slope in 5.17
893 d) around 29.5 \AA^{-1} , the median integration does not include this error. Ideally the
894 detector would have a normal distribution of pixel intensity for a given ring, which
895 would imply an equivalency between the mean and median $I(Q)$ values. Despite the
896 closeness of the mean and median once the final mask has been created, it seems that
897 the median is more reliable, as it was less effected by the beamstop holder in figure
898 5.17. Thus, for subsequent integrations discussed in this work the median is used to
899 avoid any defective features that the masking algorithm may have missed.

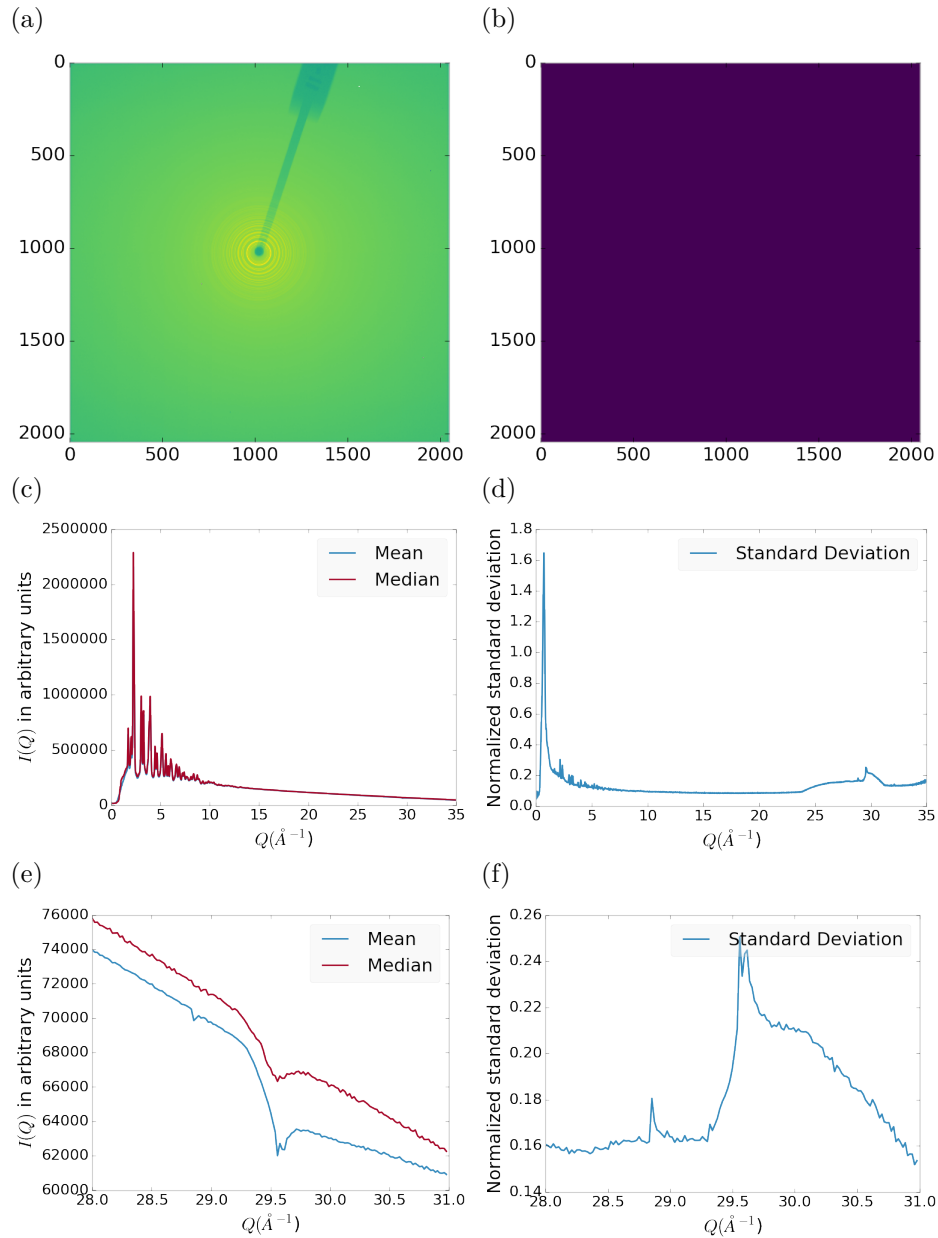


Figure 5.16: Masking, average, and standard deviation of an example x-ray total scattering measurement. This image was produced with no mask. a) the image, b) the mask, c) the mean and median values, d) the standard deviation (normalized to the median), e) a closeup of the 28 \AA^{-1} to 31 \AA^{-1} Q range for the mean and median, f) 28 \AA^{-1} to 31 \AA^{-1} Q range for the standard deviation

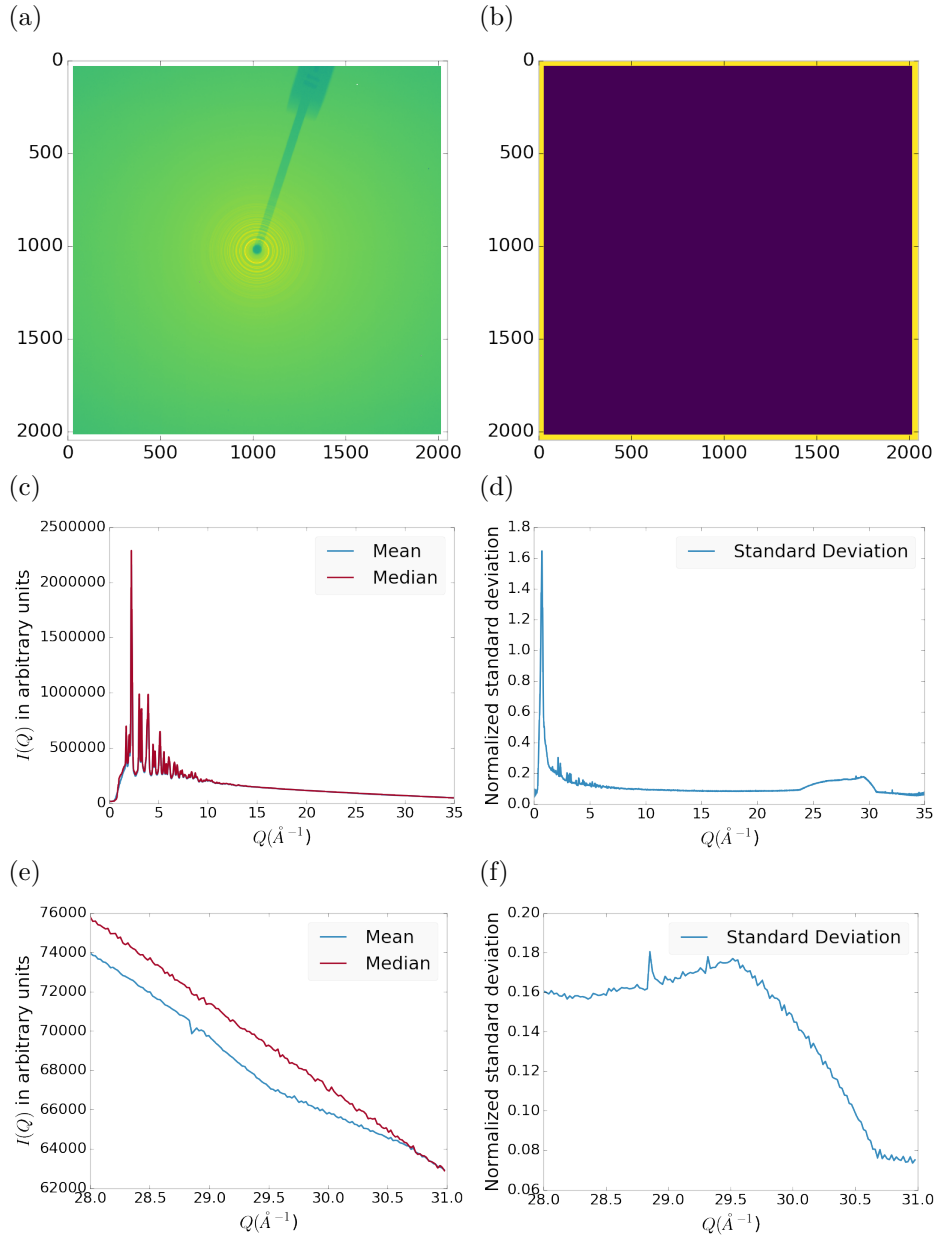


Figure 5.17: Masking, average, and standard deviation of an example x-ray total scattering measurement. This image was produced with only an edge mask. a) the image, b) the mask, c) the mean and median values, d) the standard deviation (normalized to the median), e) a closeup of the 28\AA^{-1} to 31\AA^{-1} Q range for the mean and median, f) 28\AA^{-1} to 31\AA^{-1} Q range for the standard deviation

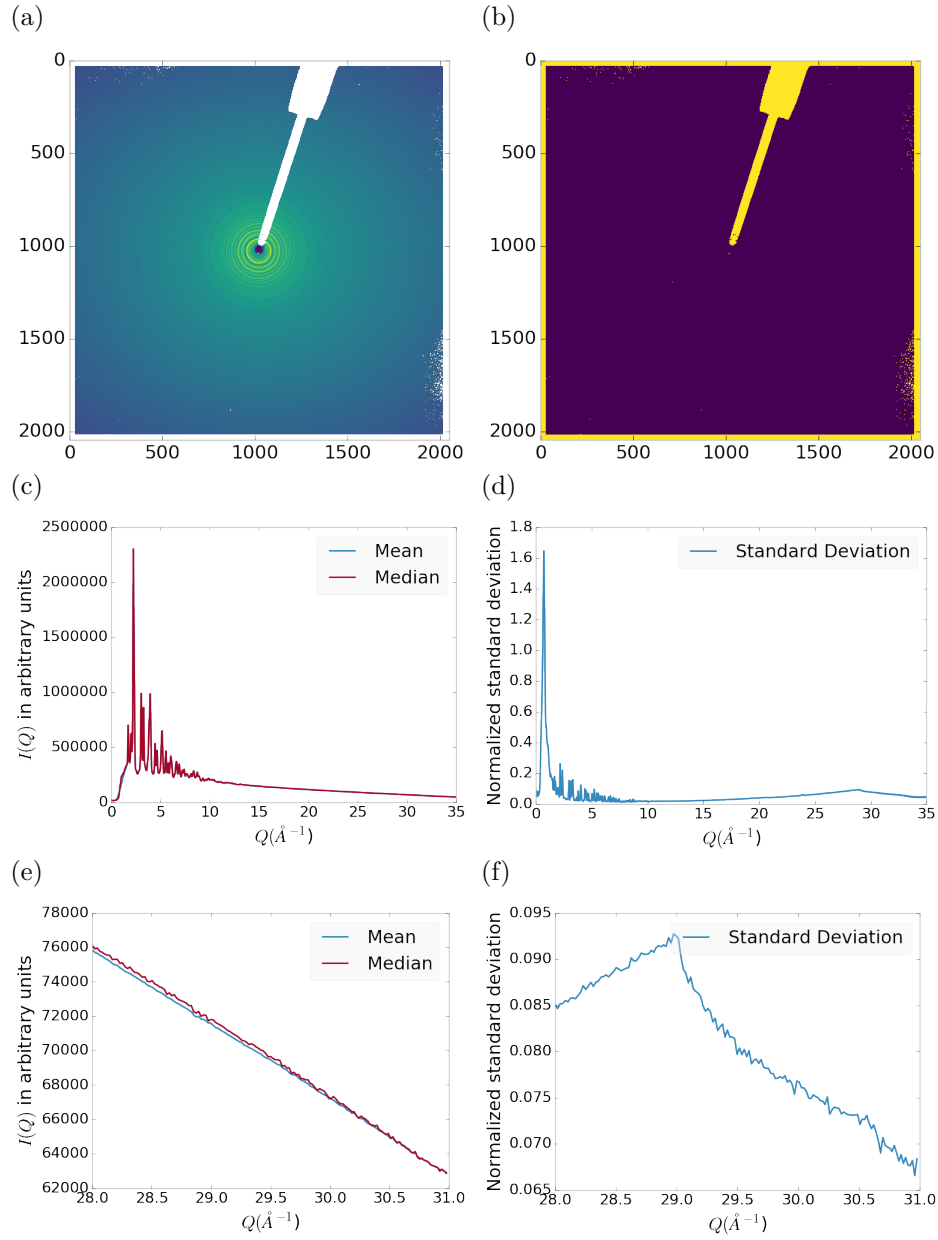


Figure 5.18: Masking, average, and standard deviation of an example x-ray total scattering measurement. This image was produced combining an edge mask and the automatically generated mask. a) the image, b) the mask, c) the mean and median values, d) the standard deviation (normalized to the median), e) a closeup of the 28 \AA^{-1} to 31 \AA^{-1} Q range for the mean and median, f) 28 \AA^{-1} to 31 \AA^{-1} Q range for the standard deviation

900 5.5 CONCLUSIONS

901 This chapter developed and analyzed the proper data processing and reduction method-
902 ology for producing reliable $F(Q)$ data from x-ray total scattering measurements.
903 Binning at the Q resolution of the detector was found to be key to the data process-
904 ing. The primary outcome of using the Q resolution binning was an enhancement
905 in effectiveness for the masking algorithm, producing much fewer false positives for
906 dead/hot pixels. This masking approach was then applied to the integration of ex-
907 perimental data taken at the APD's 11-ID-B beamline. The automatically generated
908 masks, when combined with edge masks, were found to greatly reduce the overall
909 standard deviation of the pixel intensity and produce a smoother $F(Q)$ at high Q ,
910 enabling the use of much higher Q data in the PDF. Different statistical measures
911 used in the azimuthal integration was also compared. This comparison showed that
912 the median was a more reliable statistic for integration with data which had more
913 detector defects. However, upon properly masking it was shown that these metrics
914 were almost identical. The masking induced similarity between the mean and me-
915 dian shows that the rings, when integrated, may form a Gaussian distribution. The
916 distribution of the pixel intensities for strongly and weakly scattering samples may
917 be investigated in future work.

918 CHAPTER 6

919 PHASE CHANGES AND ANNEALING DYNAMICS OF
920 Pr_2NiO_4 AND ITS DERIVATIVES

921 6.1 INTRODUCTION

922 Pr_2NiO_4 (PNO) electrodes provide higher power density than $\text{La}_{0.8}\text{Sr}_{0.2}\text{MnO}_3$ (LSM),
923 and is more stable than $(\text{La}_{0.60}\text{Sr}_{0.40})_{0.95}(\text{Co}_{0.20}\text{Fe}_{.80})\text{O}_{3-\text{x}}$ (LSCF), which is known to
924 rapidly degrade in performance. [57] PNO's high performance between 600-900 °C is
925 associated with its high activity towards the oxygen reduction reaction (ORR), which
926 stems from PNO's high oxygen diffusion and surface exchange coefficients, substantial
927 oxygen over-stoichiometry, and large oxygen ion conduction paths through the unit
928 cell. [55] Despite these advantages, PNO's tendency to partially decompose into
929 PrOx and other phases is particularly challenging. [14] Full cell operation after 500
930 hours at 750 °C and 0.8 V shows major decomposition of the parent PNO phase,
931 while the performance degrades by only 4%. Such significant changes in phase and
932 relatively small changes in performance further assure the necessity for understanding
933 the phase evolution in nickelate cathodes during operation. To address these disparity
934 in performance and phase degradation PDF and XRD analysis may be able to examine
935 these issues from both long and short range ordering perspectives.

936 6.2 EXPERIMENTS

937 **Pr₂NiO₄ Synthesis**

938 Pr₂NiO₄ was synthesized using the standard approach, as detailed in the work by
939 Dogdibegovic et. al. [14] The nickelate powder was initially prepared via the glycine-
940 nitrate process. This was followed by thermal annealing at 1080 °C for 10 hours in
941 air.

942 **X-ray Measurements**

943 X-ray total scattering and x-ray powder diffraction experiments were performed at
944 the APS's 11-ID-B beamline. An x-ray energy of 86.7 keV, .145 Åwas provided
945 by the beamline monochromator. The detector was moved between a 20cm and a
946 95 cm sample to detector distance to measure the x-ray total scattering and x-ray
947 diffraction patterns. Various PNO samples were annealed on the beamline during
948 x-ray measurement.

949 6.3 DATA PROCESSING

950 The data was calibrated at each of the detector positions using a CeO₂ standard via
951 pyFAI. [30] The images were corrected for a .95 x-ray polarization. Masks were pro-
952 duced for both the foreground and background images. The foreground masks were
953 produced using both a 30 pixel edge mask and a 2.5σ automatic mask as discussed
954 in chapter 5. The background masks were produced by using the fairground mask as
955 a starting mask with a 2.5σ automatic mask.

956 The foreground and background images were then integrated using the Q resolu-
957 tion binning discussed in chapter 5. The resulting $I(Q)$ data were corrected for their
958 number of frames and I_{00} . Finally the corrected background $I(Q)$ was subtracted
959 from the foreground $I(Q)$.

960 Each PDF was generated with a Q_{min} of 1.5, Q_{max} of 29., R_{poly} of .9, R_{max} of 40.
961 descriptions of these parameters can be found in the work by Juhas et. al. [28]

962 6.4 DATA ANALYSIS

963 **Intra Sample Comparison**

964 **PDF**

965 As figures 6.1 and 6.2 show the as synthesized PNO undergoes very little change in
966 structure according to the PDF. The PDF does show some broadening at around 3.5
967 and 8.5 Å, but the peak shifts themselves are fairly limited. This implies that the as
968 synthesized PNO structure is stable at least for the 1 hour that the sample was held
969 at 750 °C.

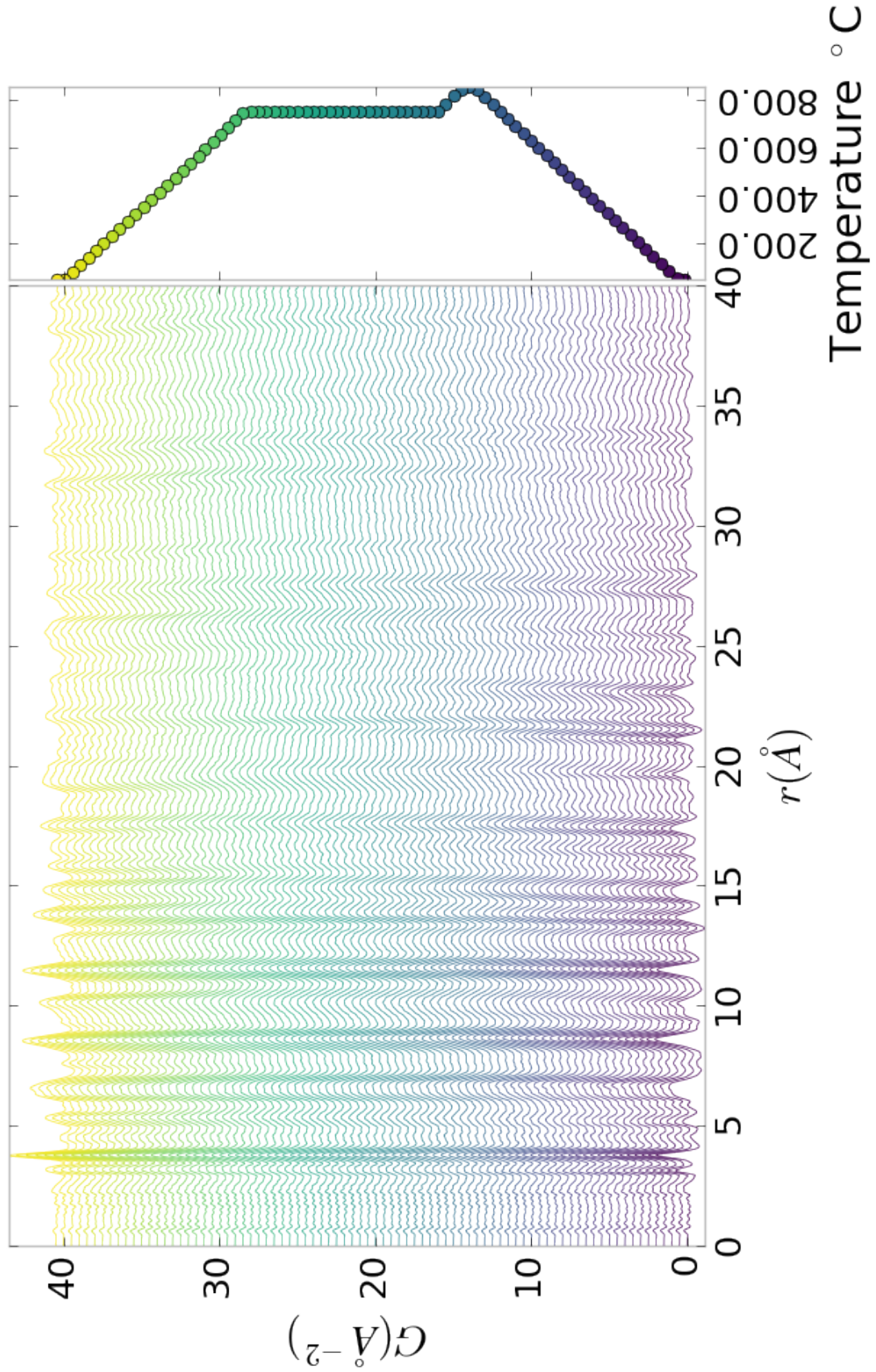


Figure 6.1: PDF as a function of temperature for as synthesized PNO showing the full PDF

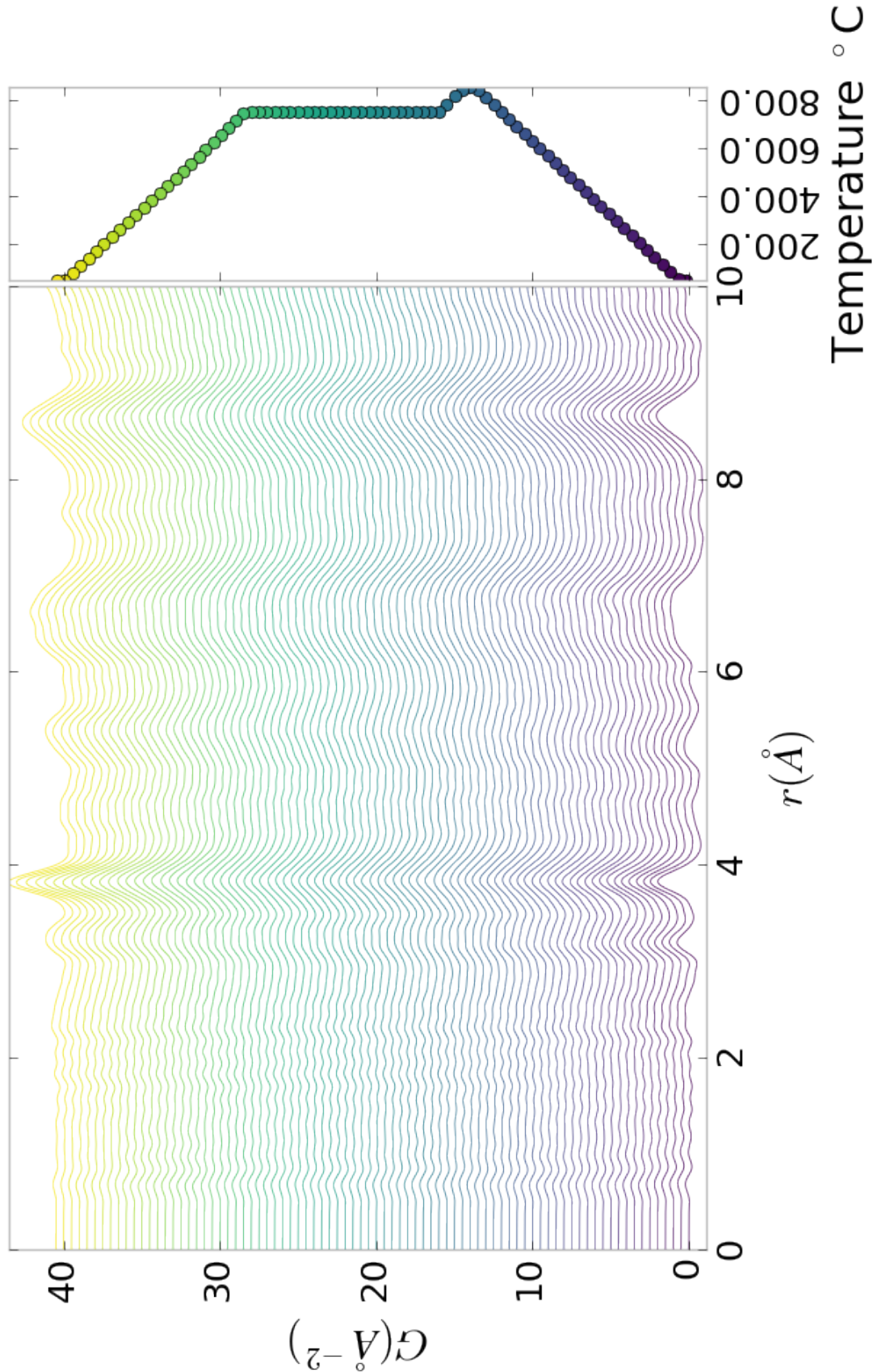


Figure 6.2: PDF as a function of temperature for as synthesized PNO showing a close up on the short range section

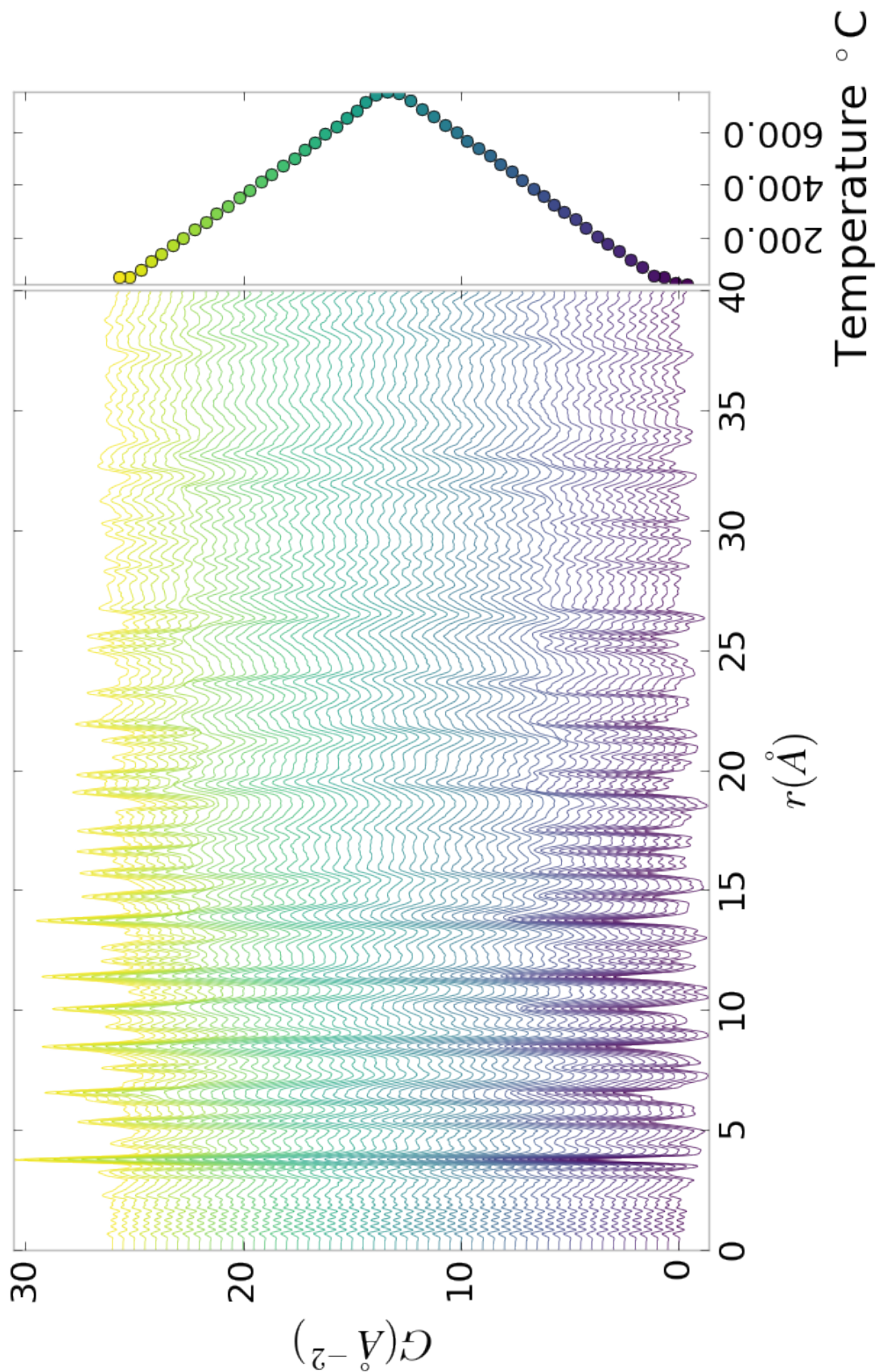


Figure 6.3: PDF as a function of temperature for PNO annealed at 750 °C for 25 hours showing the full PDF

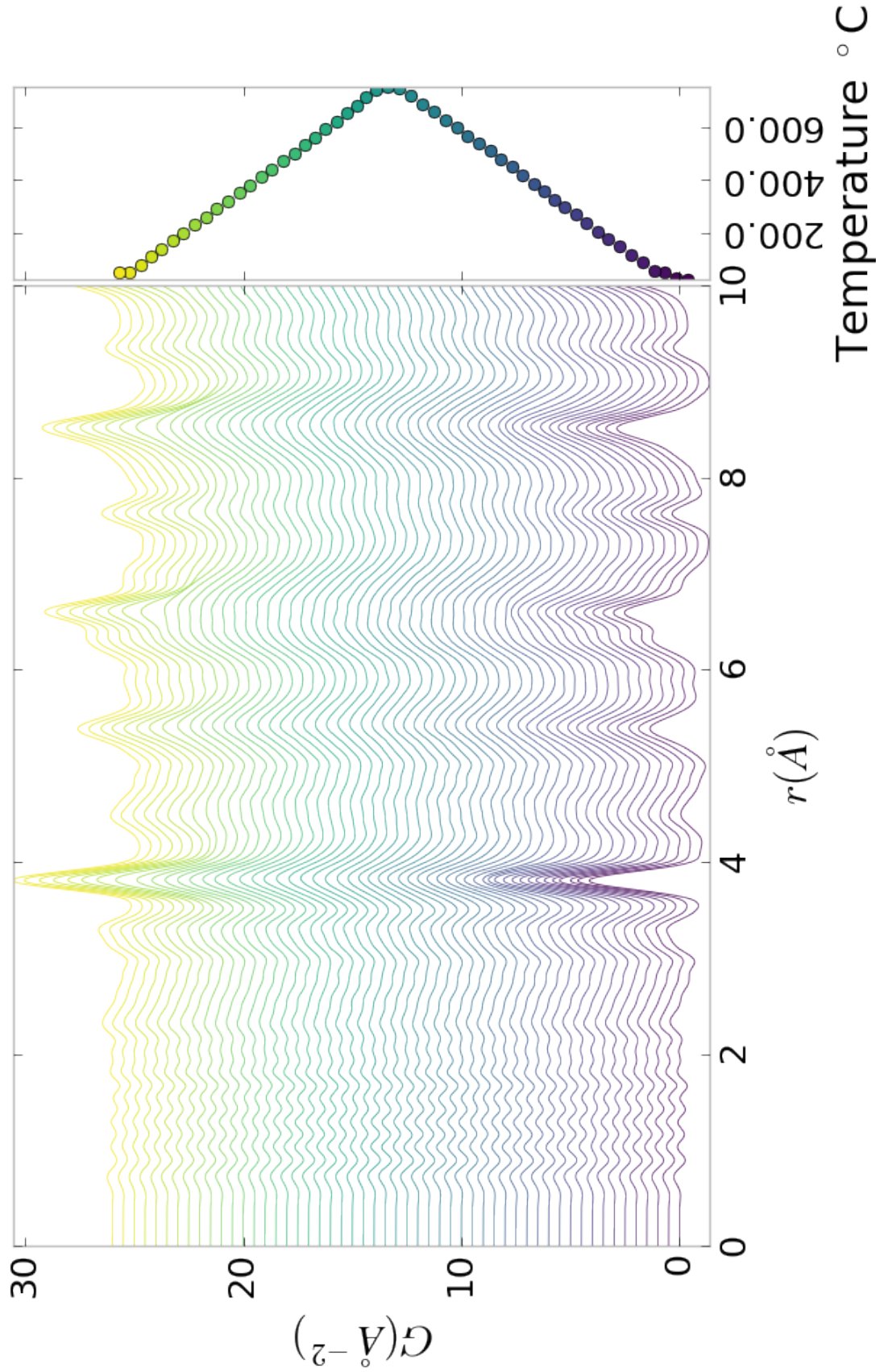


Figure 6.4: PDF as a function of temperature for PNO annealed at 750 $^{\circ}\text{C}$ for 25 hours showing a close up on the short range section

970 $I(Q)$

971 The annealed samples figures, 6.3 and 6.4, tell a rather different story. In this case the
972 PDF shows significant peak shifts and broadening, especially at higher interatomic
973 distances. Some peaks completely disappear, like the peak at 12 Å. Similar results
974 were also observed for samples with longer annealing times, as shown in the appendix.

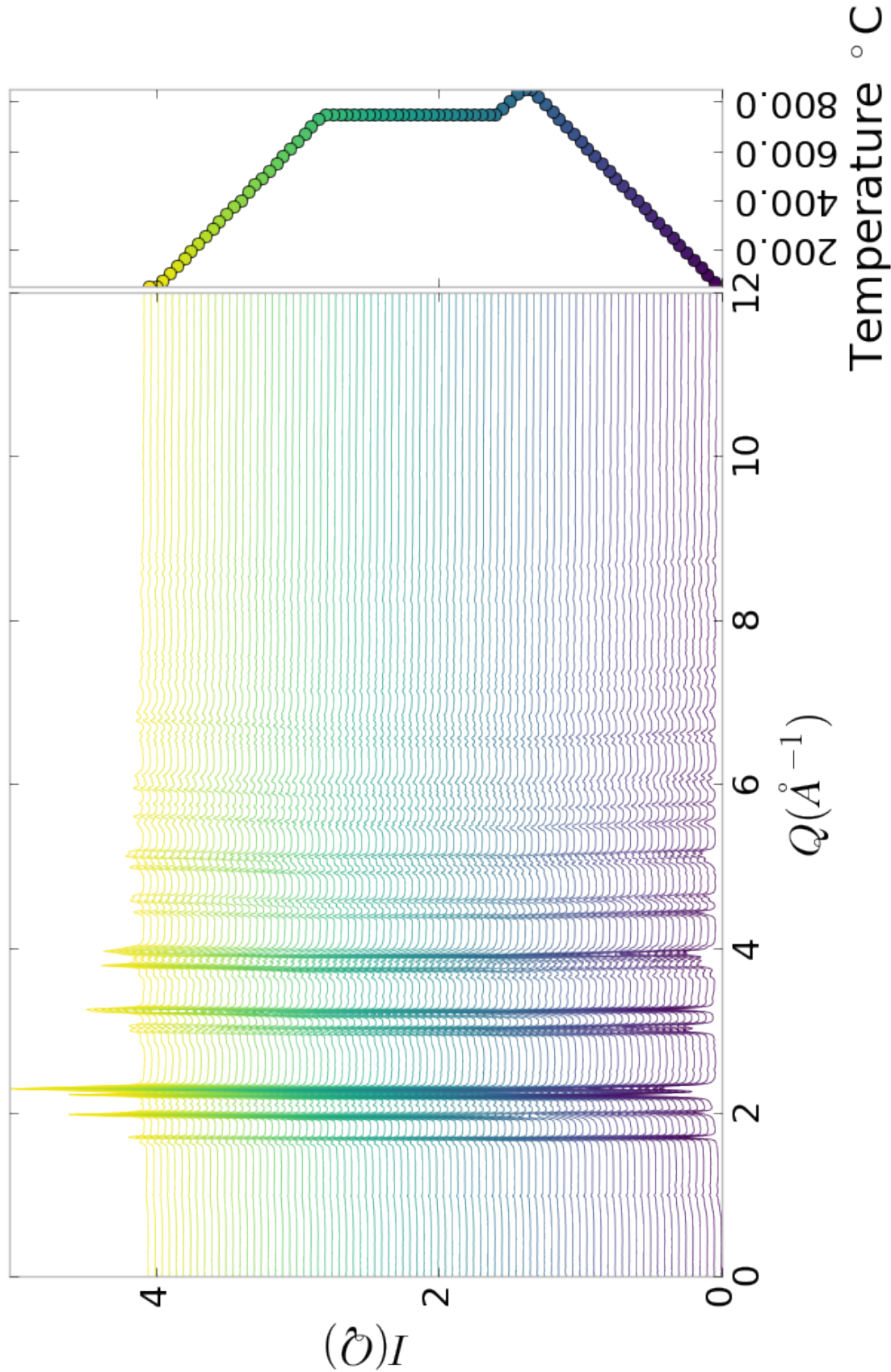


Figure 6.5: $I(Q)$ as a function of temperature for as synthesized PNO showing the full XRD

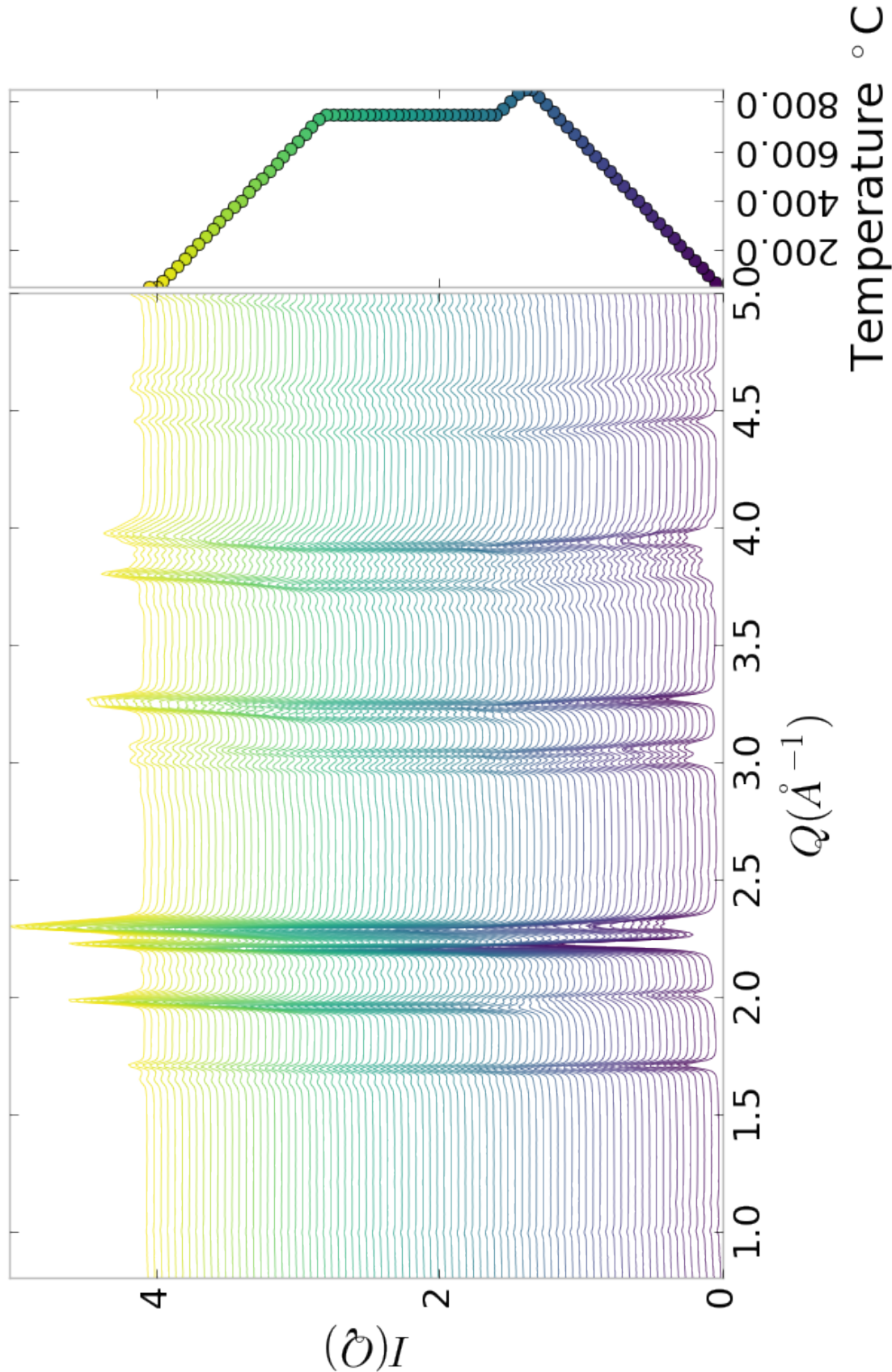


Figure 6.6: $I(Q)$ as a function of temperature for synthesized PNO showing a close up on the low Q section

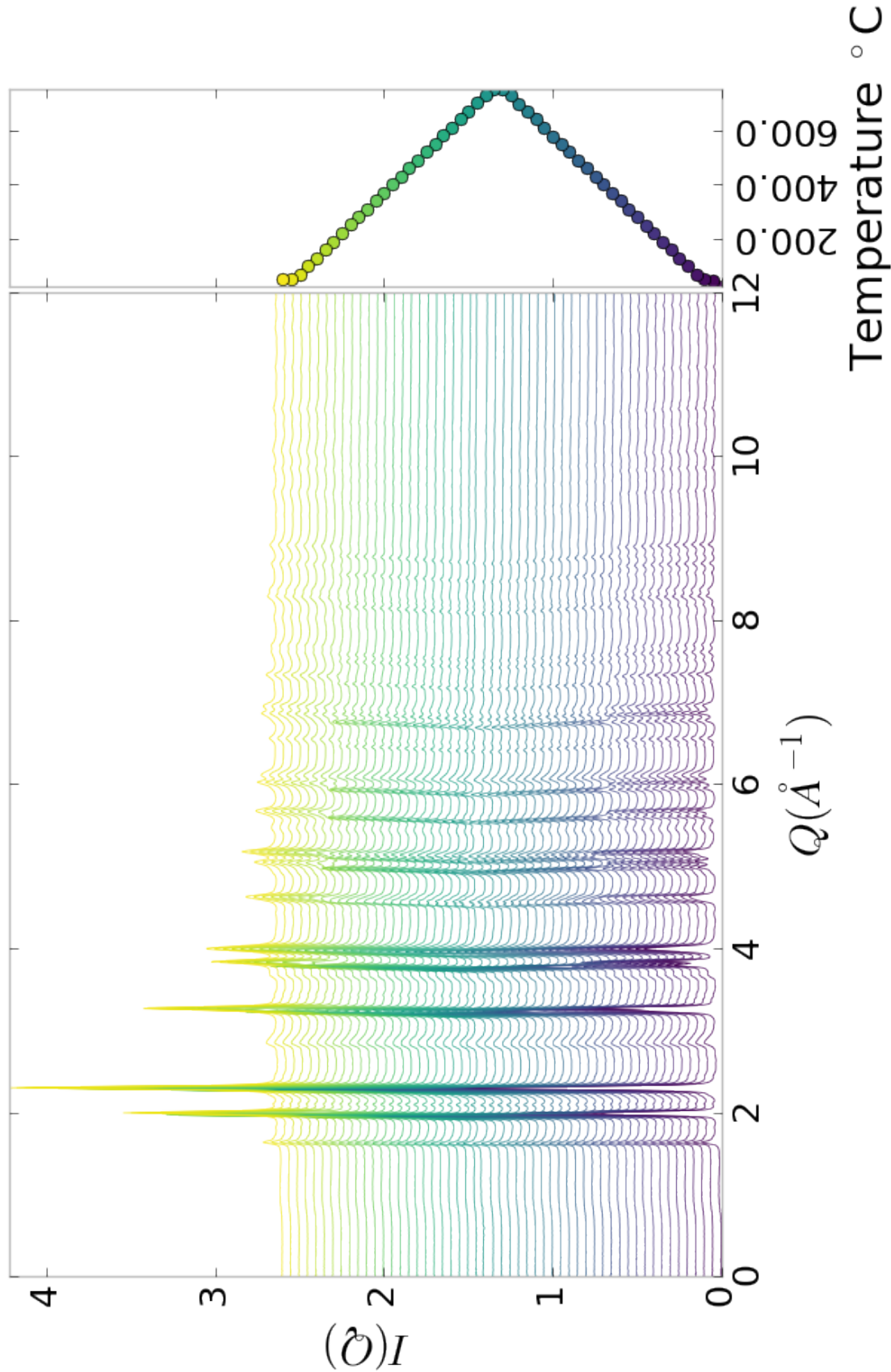


Figure 6.7: $I(Q)$ as a function of temperature for PNO annealed at 750 °C for 25 hours showing the full XRD

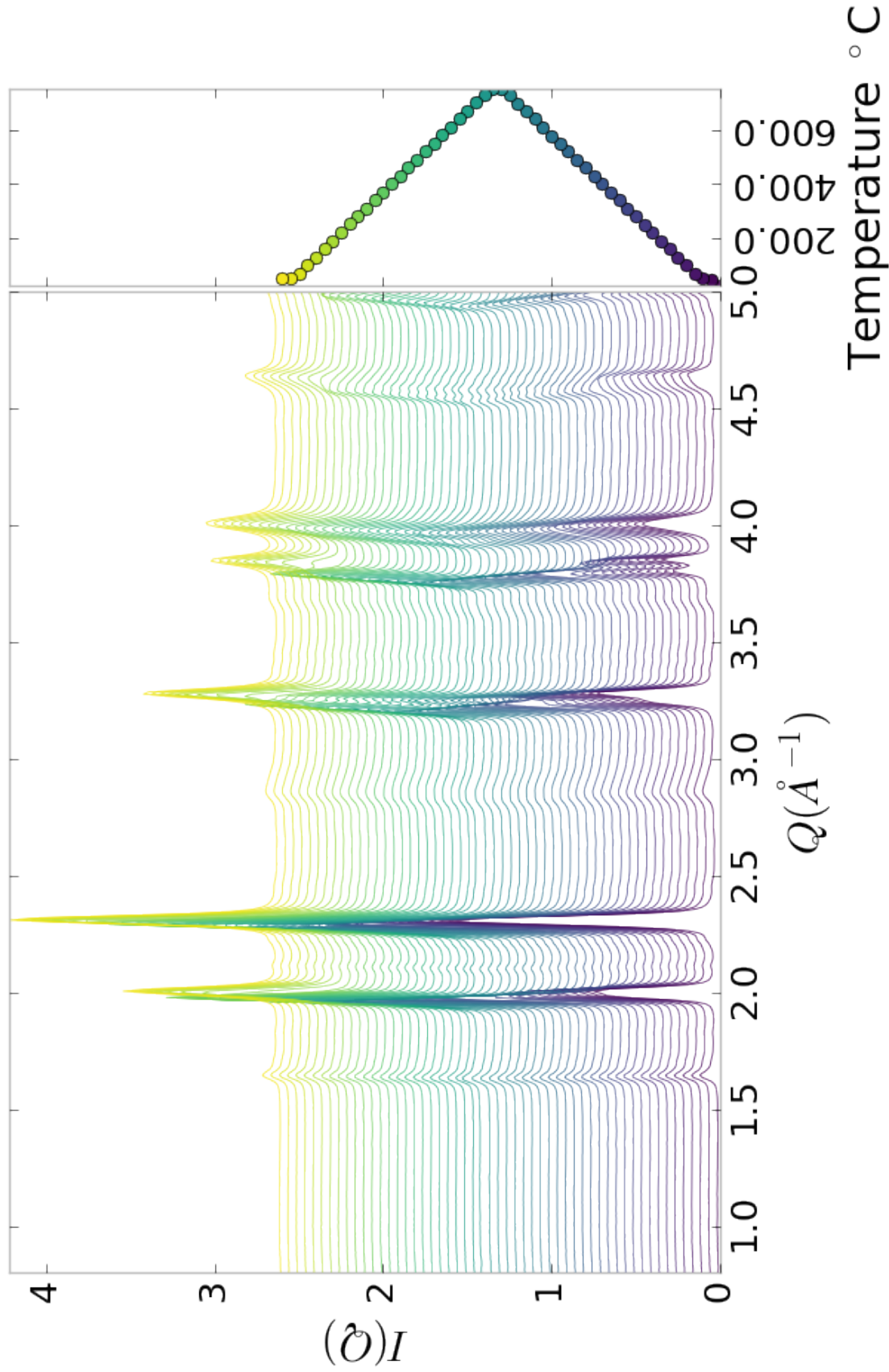


Figure 6.8: $I(Q)$ as a function of temperature for PNO annealed at 750 °C for 25 hours showing a close up on the low Q section

975 Inter Sample Comparison

976 Figures A.26 and A.20 show a very interesting contrast. Figure A.26 show significant
977 differences in the $I(Q)$ between the as-synthesized and annealed PNO, which could
978 be associated with the more degradation present in the annealed samples. However,
979 figure A.20 shows very little difference in the PDF between the various annealing
980 times. This discrepancy seems to point to some kind of disorder which changes the
981 interatomic distances very little but changes the symmetry enough to change the
982 Bragg reflections.

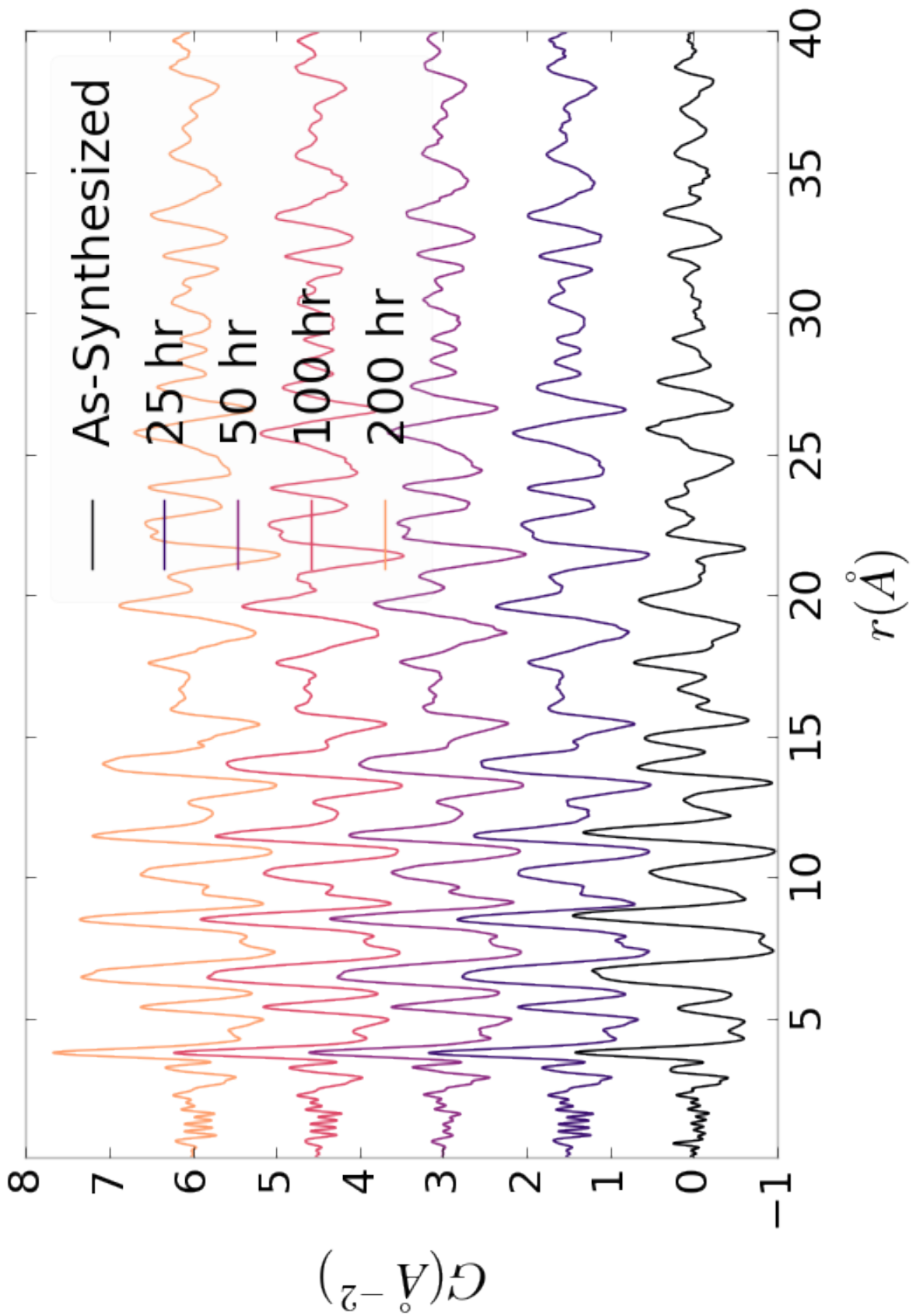


Figure 6.9: Comparison of PNO sample PDFs as a function of annealing time high-temp

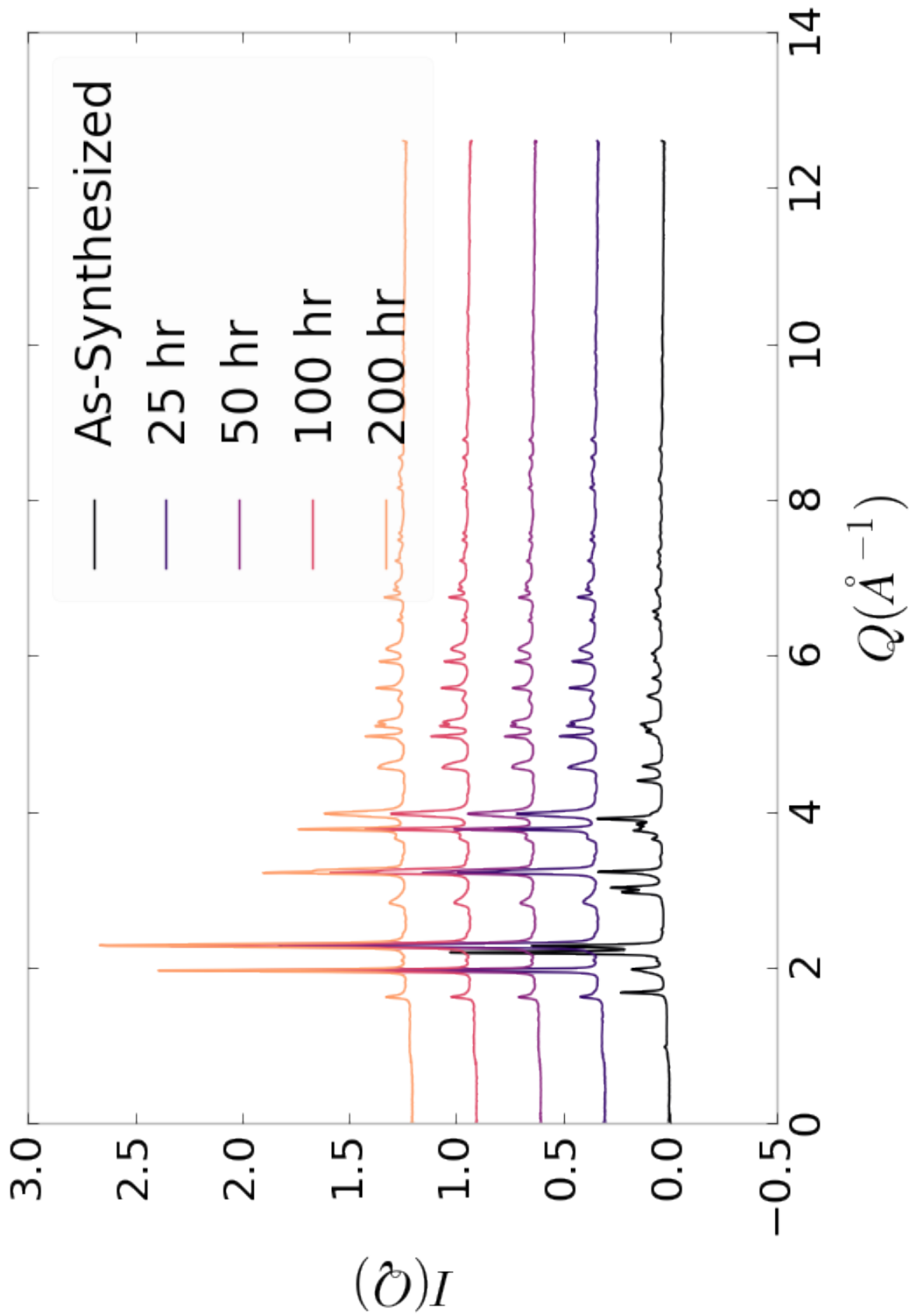


Figure 6.10: Comparison of PNO sample $I(Q)$ as a function of annealing time high-temp

983 6.5 SIMULATION

984 Simulations have not been run yet on these PNO samples. Solving the structures of
985 these samples is expected to be more difficult than the NP benchmarks previously
986 solved. The difficulty of these simulations is due to:

- 987 1. The PDF's insensitivity to the oxygen positions, due to the poor x-ray scattering
988 off the very electron poor oxygen.
- 989 2. The large difference in mass between the oxygen and other atoms, causing the
990 dynamics of the simulation to be governed by oxygen motion, necessitating long
991 simulation times to obtain movement of the other atoms.
- 992 3. The large parameter space caused by potential defects and degradation prod-
993 ucts. Without knowing that the starting phase is pure, it is difficult to even
994 produce starting structures, since the simulation will need to explore all the
995 potential defect/degenerated structures.

996 6.6 CONCLUSIONS

997 X-ray total scattering and x-ray powder diffraction data was obtained on Pr_2NiO_4
998 powder samples annealed for various lengths of time. In-situ studies on the beamline
999 were performed to understand how the structure of each of these powders changes
1000 at operating temperatures. The data was processed with the previously discussed Q
1001 binning, masking, and integration methodology. The PDF results show very little
1002 change in the structure for the as synthesized sample. However, the PDFs show
1003 a large change in the previously annealed samples. These changes seem to produce
1004 PDFs similar to the as-synthesized PNO at operating temperatures. This would seem
1005 to imply that the source of the anomalous PNO phase/power density relationship may
1006 be due to the adoption of an active structure upon heating which is universal despite

1007 the amount of thermal degradation observed at room temperature. In contrast to the
1008 PDF results, the XRD results seem to show significant changes in the PNO structure,
1009 both with ex-situ and in-situ annealing. The XRDs show the degradation of the PNO
1010 into various phases, potentially including Pr_2O_{11} , and higher ordered Pr based phases.
1011 The discrepancy between these two results is quite interesting as it seems that the
1012 XRD and PDF results are contradictory. Turbostratic displacements between the
1013 layers may be a cause of the PDF/XRD disagreement, as these changes would cause
1014 very little change in the local structure observed in the PDF, while causing large
1015 changes in the XRD.

1016 CHAPTER 7

1017 CONCLUSION

1018 The work here presents one of the most complete end to end approaches to pro-
1019 cessing, analyzing, and simulating atomic pair distribution function data. The goals
1020 of this work were to build a modular, quick, and robust method for handling both
1021 experimental PDF data and solving atomic structures from said data.

1022 The statistical mechanical PES solvers were designed to robustly find atomic
1023 solutions which are global minima of the PES. This was accomplished by using some
1024 of the most advanced Monte Carlo algorithms and samplers. The analytical equations
1025 for the PES and its gradients were derived to provide the quickest searches.

1026 The PDF gradients were derived and implemented as GPU kernels to further
1027 speed up the PES search. The inclusion of the GPUs, combined with the atom pair
1028 mapping, were found to provide a 10x to 100x speedup over a multiprocessor based
1029 CPU methodology.

1030 The extensive benchmarking of the NUTS-HMC system presented in chapters 2
1031 and 3 showcased the system's robustness, speed, and effectiveness. Interestingly it
1032 seems the the simulations also helped to elucidate the relationship between Rw and
1033 the resulting fit of the secondary metrics, including radial bond distribution. This is
1034 particularly important as it begins to establish Rw goals and a relationship between
1035 Rw and the confidence that features from the underlying structure that the PDF
1036 represents are reproduced by the structural model which is produced my Monte Carlo
1037 modeling. It seems that the threshold for acceptable Rw in Monte Carlo modeling
1038 needs to be quite lower than the current literature standards to properly reproduce

1039 the structure.

1040 A novel data processing workflow was also developed which focused on using Q
1041 resolution binning to create masks automatically and azimuthally integrate. The
1042 Q resolution binning provided a significant improvement in the automated masking
1043 robustness, leading to much fewer false positives, as shown by a series of masks
1044 generated on simulated and experimental data. The effect of these masks on the
1045 median and mean azimuthal integration was also discussed, establishing masks as
1046 very important to the removal of the high Q “kink” seen in 2D area detector data.
1047 Furthermore, a comparison was drawn between the median and mean integration,
1048 showing the median to be more reliable than the mean when working with data that
1049 could have residual detector defects. Overall the masking scheme was shown to reduce
1050 the standard deviation of the data significantly.

1051 Finally, preliminary results of x-ray total scattering measurements on Pr_2NiO_4
1052 were presented. Interestingly, these results show a strong discrepancy between the
1053 PDF and $I(Q)$ data. Where the PDF shows a very static as synthesized structure,
1054 despite annealing, the associated $I(Q)$ data shows peak movement and formation. For
1055 the pre-annealed samples both the $I(Q)$ and PDF data show peak changes. Inter-
1056 estingly, the PDFs of the as synthesized and pre-annealed samples show very similar
1057 local structure at operating temperatures.

1058 Despite all the work presented here, there is of course much more to be done.
1059 Implementing new ensembles, like Parallel Tempering, and faster Grand Canonical
1060 Monte Carlo, may help to find solutions faster and with less user based parameter
1061 tuning. Building the mathematics and software to quickly compute the data from
1062 other atomistic experiments, including EXAFS, STEM, and neutron scattering, could
1063 help to produce structures which more fully describe all the available experimental
1064 data. Implementing the existing codebase in a more general High Performance Com-
1065 putting context would allow for the solution of much larger particles, and extended

1066 solids. Further benchmarking will help to probe the robustness of the algorithm
1067 with other systems, including systems with periodic boundary conditions. Faster
1068 scattering data processing will enable a quicker total turn around time from taking
1069 experimental images to producing atomic structures.

1070 Even without these enhancements it is expected that this work will become a stan-
1071 dard method for solving atomic structures from x-ray total scattering experiments,
1072 having presented one of the most complete end to end x-ray processing and analysis
1073 systems.

BIBLIOGRAPHY

- 1075 [1] Milinda Abeykoon, Christos D. Malliakas, Pavol Juhás, Emil S. Božin, Mer-
1076 couri G Kanatzidis, and Simon J L Billinge, *Quantitative nanostructure char-*
1077 *acterization using atomic pair distribution functions obtained from laboratory*
1078 *electron microscopes*, Zeitschrift fur Kristallographie **227** (2012), no. 5, 248–256.
- 1079 [2] Alexandre A. Arnold, Victor Terskikh, Qian Ying Li, Rafik Naccache, Isabelle
1080 Marcotte, and John A. Capobianco, *Structure of NaYF₄ upconverting nanopar-*
1081 *ticles: A multinuclear solid-state NMR and DFT computational study*, Journal
1082 of Physical Chemistry C **117** (2013), no. 48, 25733–25741.
- 1083 [3] Simon J L Billinge and Takeshi Egami, *Underneath the Bragg Peaks: Structural*
1084 *Analysis of complex Materials*, vol. Volume 16, Pergamon, 2012.
- 1085 [4] Simon J L Billinge and Igor Levin, *The problem with determining atomic struc-*
1086 *ture at the nanoscale.*, Science (New York, N.Y.) **316** (2007), no. 5824, 561–565.
- 1087 [5] P. E. Blöchl, *Projector augmented-wave method*, Physical Review B **50** (1994),
1088 no. 24, 17953–17979.
- 1089 [6] Gary K. Chen and Yunfei Guo, *Discovering epistasis in large scale genetic as-*
1090 *sociation studies by exploiting graphics cards*, Frontiers in Genetics **4** (2013),
1091 no. DEC, 1–12.
- 1092 [7] Joshua J Choi, Xiaohao Yang, Zachariah M Norman, Simon J L Billinge, and
1093 Jonathan S Owen, *Structure of methylammonium lead iodide within mesoporous*
1094 *titanium dioxide: Active material in high-performance perovskite solar cells*,
1095 Nano Letters **14** (2014), no. 1, 127–133.
- 1096 [8] Peter J. Chupas, Karena W. Chapman, Charles Kurtz, Jonathan C. Hanson,
1097 Peter L. Lee, and Clare P. Grey, *A versatile sample-environment cell for non-*
1098 *ambient X-ray scattering experiments*, Journal of Applied Crystallography **41**
1099 (2008), no. 4, 822–824.
- 1100 [9] PJ Chupas, X Qiu, JC Hanson, PL Lee, CP Grey, and SJL Billinge, *Rapid-*

- 1101 *acquisition pair distribution function (RA-PDF) analysis*, Journal of Applied
1102 Crystallography **36** (2003), 1342–1347.
- 1103 [10] Matthew J. Cliffe, Martin T. Dove, D. A. Drabold, and Andrew L. Goodwin,
1104 *Structure determination of disordered materials from diffraction data*, Physical
1105 Review Letters **104** (2010), no. 12, 1–4.
- 1106 [11] Matthew J Cliffe and Andrew L Goodwin, *Nanostructure determination from the*
1107 *pair distribution function: a parametric study of the INVERT approach.*, Journal
1108 of physics. Condensed matter : an Institute of Physics journal **25** (2013), no. 45,
1109 454218.
- 1110 [12] Chunhua Cui, Lin Gan, Marc Heggen, Stefan Rudi, and Peter Strasser, *Composi-*
1111 *tional segregation in shaped Pt alloy nanoparticles and their structural behaviour*
1112 *during electrocatalysis.*, Nature materials **12** (2013), no. 12, 765–771.
- 1113 [13] Juarez L F Da Silva, Hyoung Gyu Kim, Maurício J. Piotrowski, Maurício J. Pri-
1114 eto, and Germano Tremiliosi-Filho, *Reconstruction of core and surface nanopar-*
1115 *ticles: The example of Pt55 and Au55*, Physical Review B - Condensed Matter
1116 and Materials Physics **82** (2010), no. 20, 1–6.
- 1117 [14] Emir Dogdibegovic, Christopher J. Wright, and Xiao-Dong Zhou, *Stability and*
1118 *Activity of $(Pr_{1-x}Nd_x)_2NiO_4$ as Cathodes for Solid Oxide Fuel Cells: I. Quantifi-*
1119 *cation of Phase Evolution in Pr_2NiO_4* , Journal of the American Ceramic Society
1120 **5** (2016), 1–5.
- 1121 [15] Simon Duane, A. D. Kennedy, Brian J. Pendleton, and Duncan Roweth, *Hybrid*
1122 *Monte Carlo*, Physics Letters B **195** (1987), no. 2, 216–22.
- 1123 [16] Timur Dykhne, Ryan Taylor, Alastair Florence, and Simon J L Billinge, *Data*
1124 *requirements for the reliable use of atomic pair distribution functions in amor-*
1125 *phous pharmaceutical fingerprinting.*, Pharmaceutical research **28** (2011), no. 5,
1126 1041–8.
- 1127 [17] C L Farrow, P Juhas, J W Liu, D Bryndin, E S Božin, J Bloch, Th Proffen, and
1128 S J L Billinge, *PDFfit2 and PDFgui: computer programs for studying nanostruc-*
1129 *ture in crystals.*, Journal of Physics. Condensed Matter : an Institute of Physics
1130 journal **19** (2007), no. 33, 335219.
- 1131 [18] Christopher L Farrow and Simon J L Billinge, *Relationship between the atomic*
1132 *pair distribution function and small-angle scattering: implications for modeling*

- 1133 *of nanoparticles.*, Acta Crystallographica Section A Foundations of Crystallography **65** (2009), no. Pt 3, 232–9 (en).
- 1135 [19] Riccardo Ferrando, Julius Jellinek, and Roy L Johnston, *Nanoalloys: From Theory to Applications of Alloy Clusters and Nanoparticles*, Chemical Reviews **108** (2008), no. 3, 846–904.
- 1138 [20] Anatoly Frenkel, *Solving the 3D structure of metal nanoparticles*, Zeitschrift für Kristallographie **222** (2007), no. 11, 605–611.
- 1140 [21] Carmelo Giacovazzo, Hugo Luis Monaco, Gilberto Artioli, Davide Viterbo, Marco Milanesio, Gastone Gilli, Paola Gilli, Giuseppe Zanotti, Giovanni Ferraris, and Michele Catti, *Fundamentals of Crystallography*, Oxford University Press, 1992.
- 1144 [22] Benjamin Gilbert, Jasmine J. Erbs, R. Lee Penn, Valeri Petkov, Dino Spagnoli, and Glenn A. Waychunas, *A disordered nanoparticle model for 6-line ferrihydrite*, American Mineralogist **98** (2013), no. 8-9, 1465–1476.
- 1147 [23] Benjamin Gilbert, Feng Huang, Hengzhong Zhang, Glenn A. Waychunas, and Jillian F Banfield, *Nanoparticles: strained and stiff.*, Science (New York, N.Y.) **305** (2004), no. 5684, 651–654.
- 1150 [24] Md Matthew D. Hoffman and Andrew Gelman, *The No-U-Turn Sampler: Adaptively Setting Path Lengths in Hamiltonian Monte Carlo*, The Journal of Machine Learning Research **15** (2014), no. 2008, 1593–1623.
- 1153 [25] W J Huang, R Sun, J Tao, L D Menard, R G Nuzzo, and J M Zuo, *Coordination-dependent surface atomic contraction in nanocrystals revealed by coherent diffraction.*, Nature Materials **7** (2008), no. 4, 308–313.
- 1156 [26] Pablo D Jadzinsky, Guillermo Calero, Christopher J Ackerson, David A Bushnell, and Roger D Kornberg, *Structure of a thiol monolayer-protected gold nanoparticle at 1.1 Å resolution.*, Science (New York, N.Y.) **318** (2007), no. 5849, 430–433.
- 1159 [27] I. K. Jeong, R. H. Heffner, M. J. Graf, and S. J. L. Billinge, *Lattice dynamics and correlated atomic motion from the atomic pair distribution function*, (2002), 9.
- 1162 [28] P. Juhás, T. Davis, C. L. Farrow, and S. J. L. Billinge, *PDFgetX3 : a rapid and highly automatable program for processing powder diffraction data into total*

- 1164 *scattering pair distribution functions*, Journal of Applied Crystallography **46**
1165 (2013), no. 2, 560–566 (en).
- 1166 [29] A. Kassiba, M. Makowska-Janusik, J. Bouclé, J. Bardeau, A. Bulou, and
1167 N. Herlin-Boime, *Photoluminescence features on the Raman spectra of quasistoi-*
1168 *chiometric SiC nanoparticles: Experimental and numerical simulations*, Physical
1169 Review B **66** (2002), no. 15, 1–7.
- 1170 [30] Jérôme Kieffer and Dimitrios Karkoulis, *PyFAI, a versatile library for azimuthal*
1171 *regrouping*, Journal of Physics: Conference Series **425** (2013), 202012.
- 1172 [31] G. Kresse and OJ. Hafner, *Ab initio molecular-dynamics simulation of the liquid-*
1173 *metal-amorphous-semiconductor transition in germanium*, Physical Review B **49**
1174 (1994), no. 20, 14251–14269.
- 1175 [32] G. Kresse and J. Hafner, *Ab initio molecular dynamics for liquid metals*, Physical
1176 Review B **47** (1993), no. 1, 558–561.
- 1177 [33] Yan Li, Giulia Galli, and François Gygi, *Electronic structure of thiolate-covered*
1178 *gold nanoparticles: Au102(MBA)44*, ACS Nano **2** (2008), no. 9, 1896–1902.
- 1179 [34] L D Marks, *Experimental studies of small particle structures*, Reports on
1180 Progress in Physics **57** (1994), no. 6, 603–649 (en).
- 1181 [35] A. S. Masadeh, E. S. Božin, C. L. Farrow, G. Paglia, P. Juhas, S. J. L. Billinge,
1182 A. Karkamkar, and M. G. Kanatzidis, *Quantitative size-dependent structure and*
1183 *strain determination of CdSe nanoparticles using atomic pair distribution func-*
1184 *tion analysis*, Physical Review B - Condensed Matter and Materials Physics **76**
1185 (2007), no. 11, 115413.
- 1186 [36] R L McGreevy and L Pusztai, *Reverse Monte Carlo Simulation: A New Tech-*
1187 *nique for the Determination of Disordered Structures*, Molecular Simulation **1**
1188 (1988), no. 6, 359–367.
- 1189 [37] Donald A. McQuarrie, *Statistical Mechanics*, University Science Books, Sausalito,
1190 CA, 2000.
- 1191 [38] Radford M Neal, *Probabilistic Inference Using Markov Chain Monte Carlo Meth-*
1192 *ods*, Intelligence **45** (1993), no. September, 144.

- 1193 [39] Radford M. Neal, *MCMC Using Hamiltonian Dynamics*, Handbook of Markov
1194 Chain Monte Carlo (Steve Brooks, Andrew Gelman, Galin L. Jones and Xiao-Li
1195 Meng, eds.), Chapman and Hall/CRC, 2011, pp. 113–162.
- 1196 [40] Katharine Page, Taylor C. Hood, Thomas Proffen, and Reinhard B. Neder,
1197 *Building and refining complete nanoparticle structures with total scattering data*,
1198 Journal of Applied Crystallography **44** (2011), no. 2, 327–336 (en).
- 1199 [41] B R Pauw, *Corrigendum: Everything SAXS: small-angle scattering pattern col-*
1200 *lection and correction (2013 J. Phys.: Condens. Matter 25 383201)*, Journal of
1201 Physics: Condensed Matter **26** (2014), no. 23, 239501.
- 1202 [42] Vitalij Pecharsky and Peter Zavalij, *Fundamentals of Powder Diffraction and*
1203 *Structural Characterization of Materials*, Springer Science, 2009.
- 1204 [43] John P. Perdew, Kieron Burke, and Matthias Ernzerhof, *Generalized Gradient*
1205 *Approximation Made Simple*, Physical Review Letters **77** (1996), no. 18, 3865–
1206 3868.
- 1207 [44] Andrew A. Peterson, *Global optimization of adsorbate-surface structures while*
1208 *preserving molecular identity*, Topics in Catalysis **57** (2014), no. 1-4, 40–53.
- 1209 [45] Valeri Petkov, Youngmin Lee, Shouheng Sun, and Yang Ren, *Noncrystallographic*
1210 *atomic arrangement driven enhancement of the catalytic activity of Au nanoparticles*, Journal of Physical Chemistry C **116** (2012), no. 50, 26668–26673.
- 1212 [46] Valeri Petkov, Binay Prasai, Yang Ren, Shiyao Shan, Jin Luo, Pharrah Joseph,
1213 and Chuan-Jian Zhong, *Solving the nanostructure problem: exemplified on metal-*
1214 *alloy nanoparticles*, Nanoscale **6** (2014), no. 17, 1–11.
- 1215 [47] Valeri Petkov, Shiyao Shan, Peter Chupas, Jun Yin, Lefu Yang, Jin Luo, and
1216 Chuan-Jian Zhong, *Noble-transition metal nanoparticle breathing in a reactive*
1217 *gas atmosphere.*, Nanoscale **5** (2013), no. 16, 7379–87.
- 1218 [48] Th. Proffen and R. B. Neder, *DISCUS: a Program for Diffuse Scattering and*
1219 *Defect-Structure Simulation*, Journal of Applied Crystallography **30** (1997), 171–
1220 175.
- 1221 [49] Erin L. Redmond, Brian P. Setzler, Pavol Juhas, Simon J. L. Billinge, and
1222 Thomas F. Fuller, *In-Situ Monitoring of Particle Growth at PEMFC Cathode*
1223 *under Accelerated Cycling Conditions*, Electrochemical and Solid-State Letters
1224 **15** (2012), no. 5, B72 (en).

- 1225 [50] H. W. Sheng, M. J. Kramer, A. Cadien, T. Fujita, and M. W. Chen, *Highly*
1226 *optimized embedded-atom-method potentials for fourteen FCC metals*, Physical
1227 Review B - Condensed Matter and Materials Physics **83** (2011), no. 13, 134118.
- 1228 [51] Chenyang Shi, Majid Beidaghi, Michael Naguib, Olha Mashtalir, Yury Gogotsi,
1229 and Simon J L Billinge, *Structure of Nanocrystalline Ti₃C₂ MXene Using Atomic*
1230 *Pair Distribution Function.*, Physical Review Letters **112** (2014), no. March,
1231 125501.
- 1232 [52] Randall Q. Snurr, Alexis T. Bell, and Doros N. Theodorou, *Prediction of ad-*
1233 *sorption of aromatic hydrocarbons in silicalite from grand canonical Monte Carlo*
1234 *simulations with biased insertions*, The Journal of Physical Chemistry **97** (1993),
1235 no. 51, 13742–13752 (EN).
- 1236 [53] Chang Q. Sun, *Size dependence of nanostructures: Impact of bond order defi-*
1237 *ciency*, Progress in Solid State Chemistry **35** (2007), no. 1, 1–159.
- 1238 [54] X. Yang, P. Juhás, and S. J L Billinge, *On the estimation of statistical uncertain-*
1239 *ties on powder diffraction and small-angle scattering data from two-dimensional*
1240 *X-ray detectors*, Journal of Applied Crystallography **47** (2014), no. 4, 1273–1283.
- 1241 [55] Masatomo Yashima, Makiko Enoki, Takahiro Wakita, Roushown Ali, Yoshitaka
1242 Matsushita, Fujio Izumi, and Tatsumi Ishihara, *Structural Disorder and Dif-*
1243 *fusional Pathway of Oxide Ions in a Doped Pr₂NiO₄ -Based Mixed Conductor*,
1244 Journal of the American Chemical Society **130** (2008), no. 9, 2762–2763.
- 1245 [56] Hengzhong Zhang, Bin Chen, Jillian F. Banfield, and Glenn A. Waychunas,
1246 *Atomic structure of nanometer-sized amorphous TiO₂*, Physical Review B **78**
1247 (2008), no. 21, 214106.
- 1248 [57] X.-D. Zhou, J.W. Templeton, Z. Nie, H. Chen, J.W. Stevenson, and L.R. Pedersen,
1249 *Electrochemical performance and stability of the cathode for solid oxide fuel*
1250 *cells: V. high performance and stable Pr₂NiO₄ as the cathode for solid oxide fuel*
1251 *cells*, Electrochimica Acta **71** (2012), 44–49.

1252

APPENDIX A

1253

SUPPLEMENTAL INFORMATION: PHASE CHANGES AND

1254

ANNEALING DYNAMICS OF Pr_2NiO_4 AND ITS

1255

DERIVATIVES

1256 **Intra Sample Comparison**

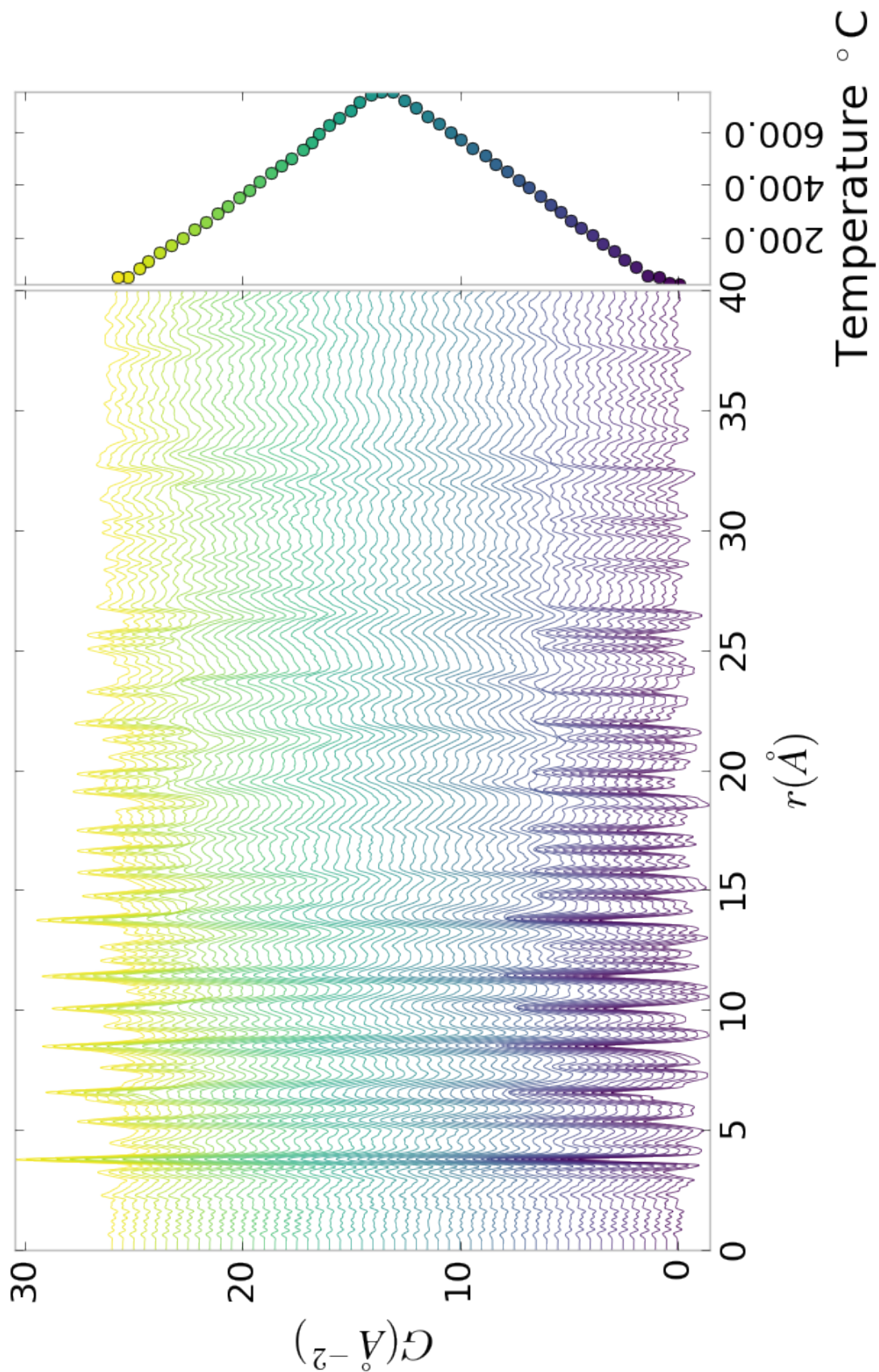


Figure A.1: PDF as a function of temperature for PNO annealed at 750 $^{\circ}\text{C}$ for 50 hours showing the full PDF

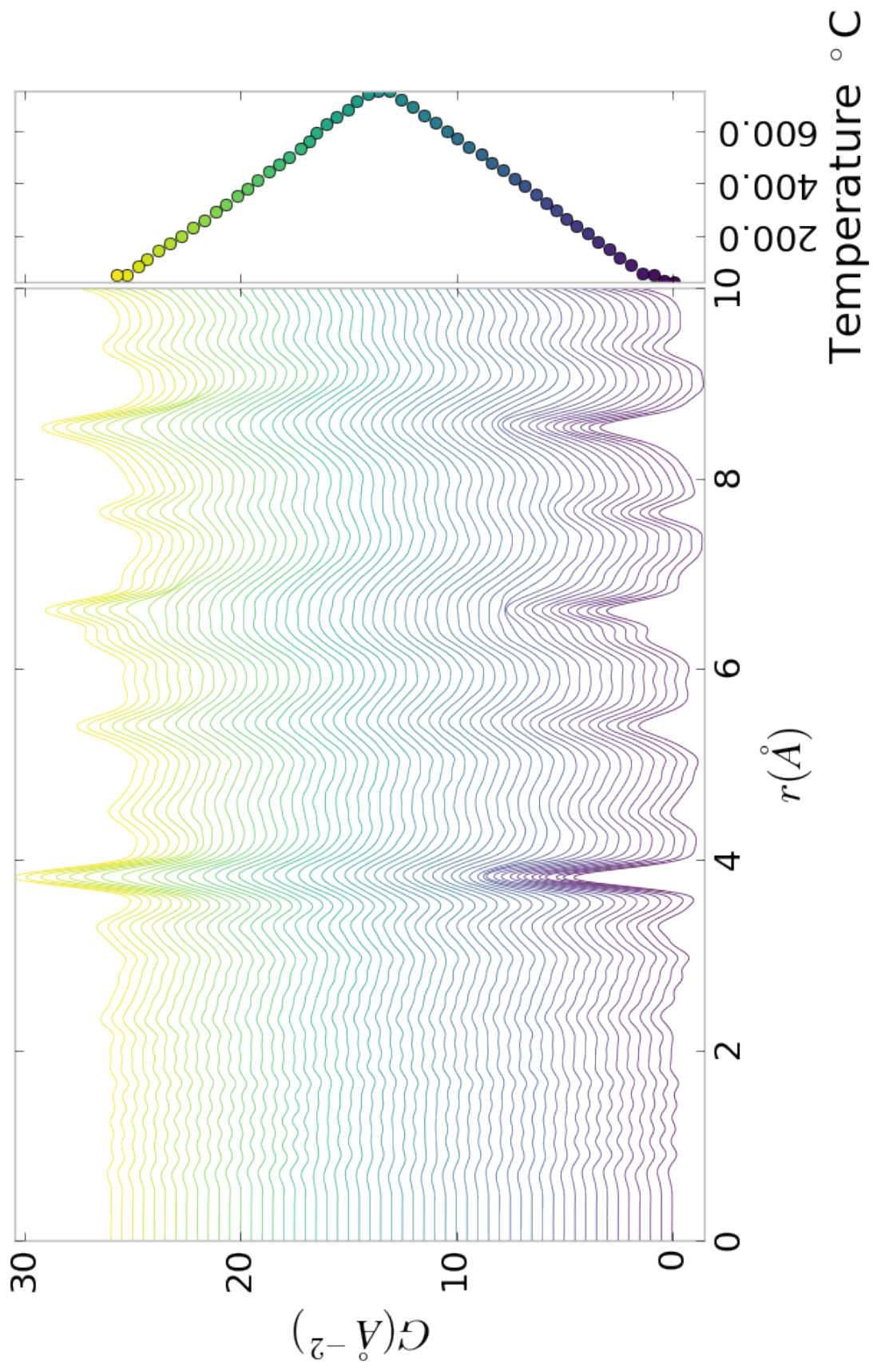


Figure A.2: PDF as a function of temperature for PNO annealed at 750 °C for 50 hours showing a close up on the short range section

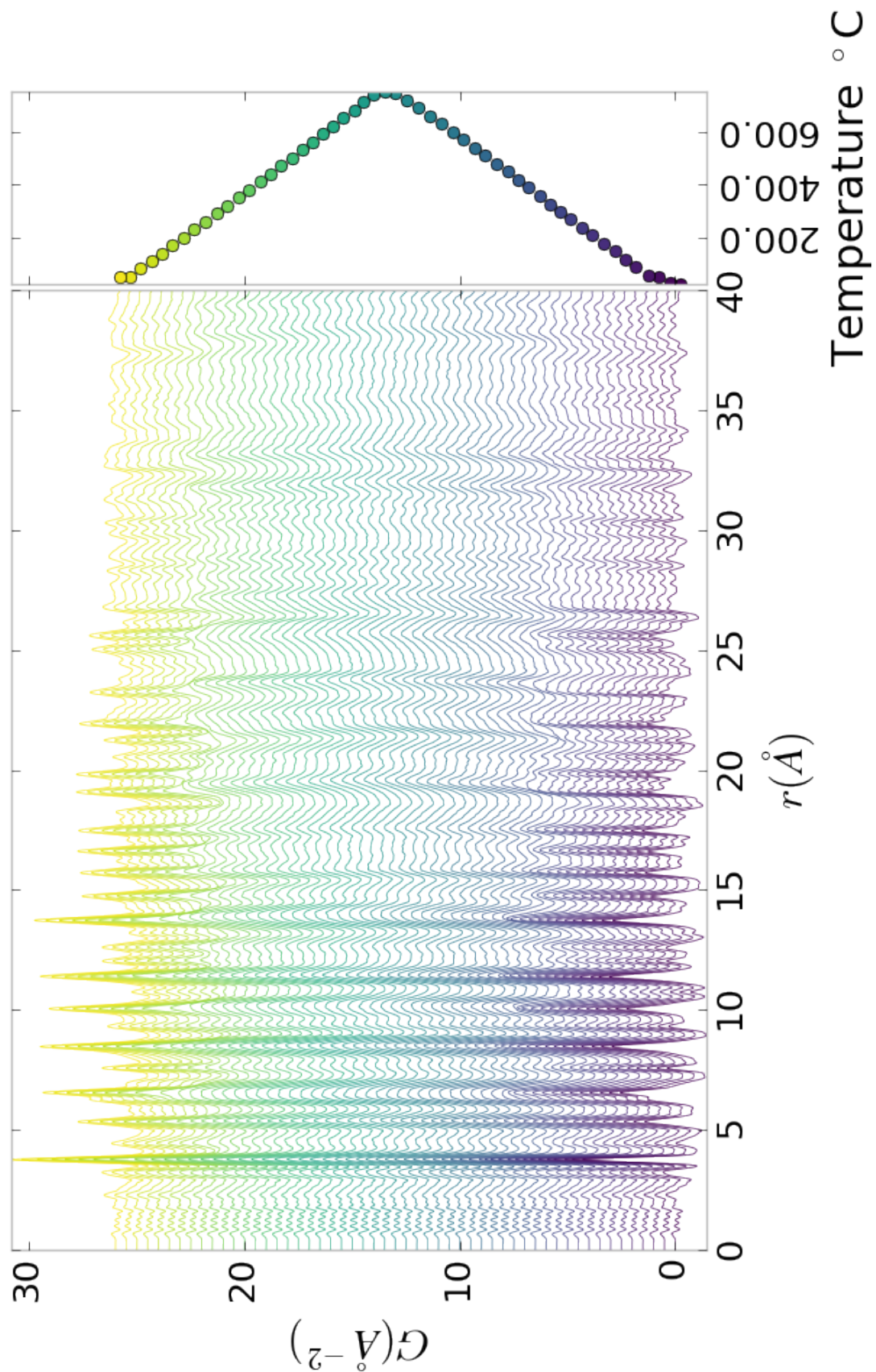


Figure A.3: PDF as a function of temperature for PNO annealed at 750 $^\circ\text{C}$ for 100 hours showing the full PDF

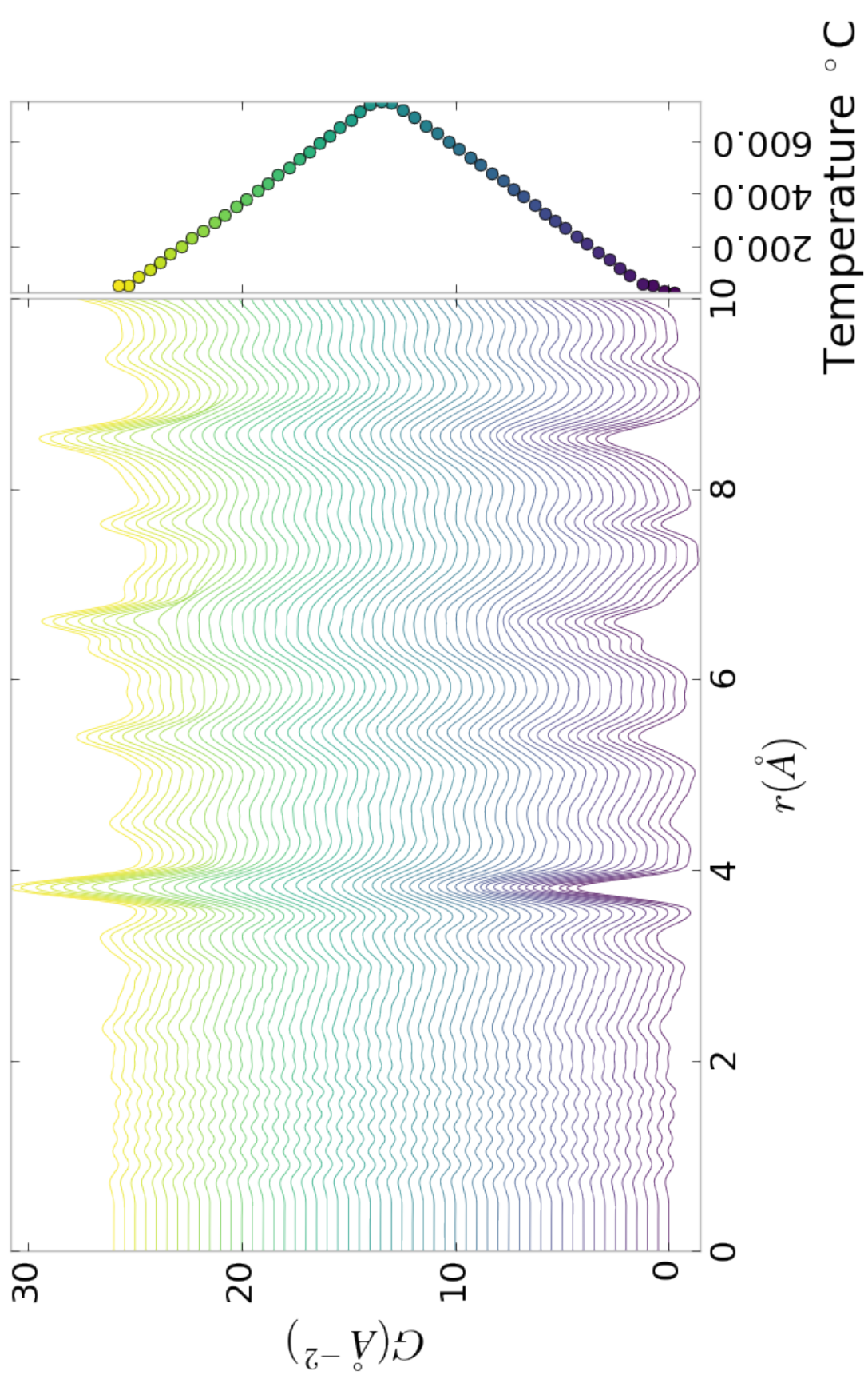


Figure A.4: PDF as a function of temperature for PNO annealed at 750 °C for 100 hours showing a close up on the short range section

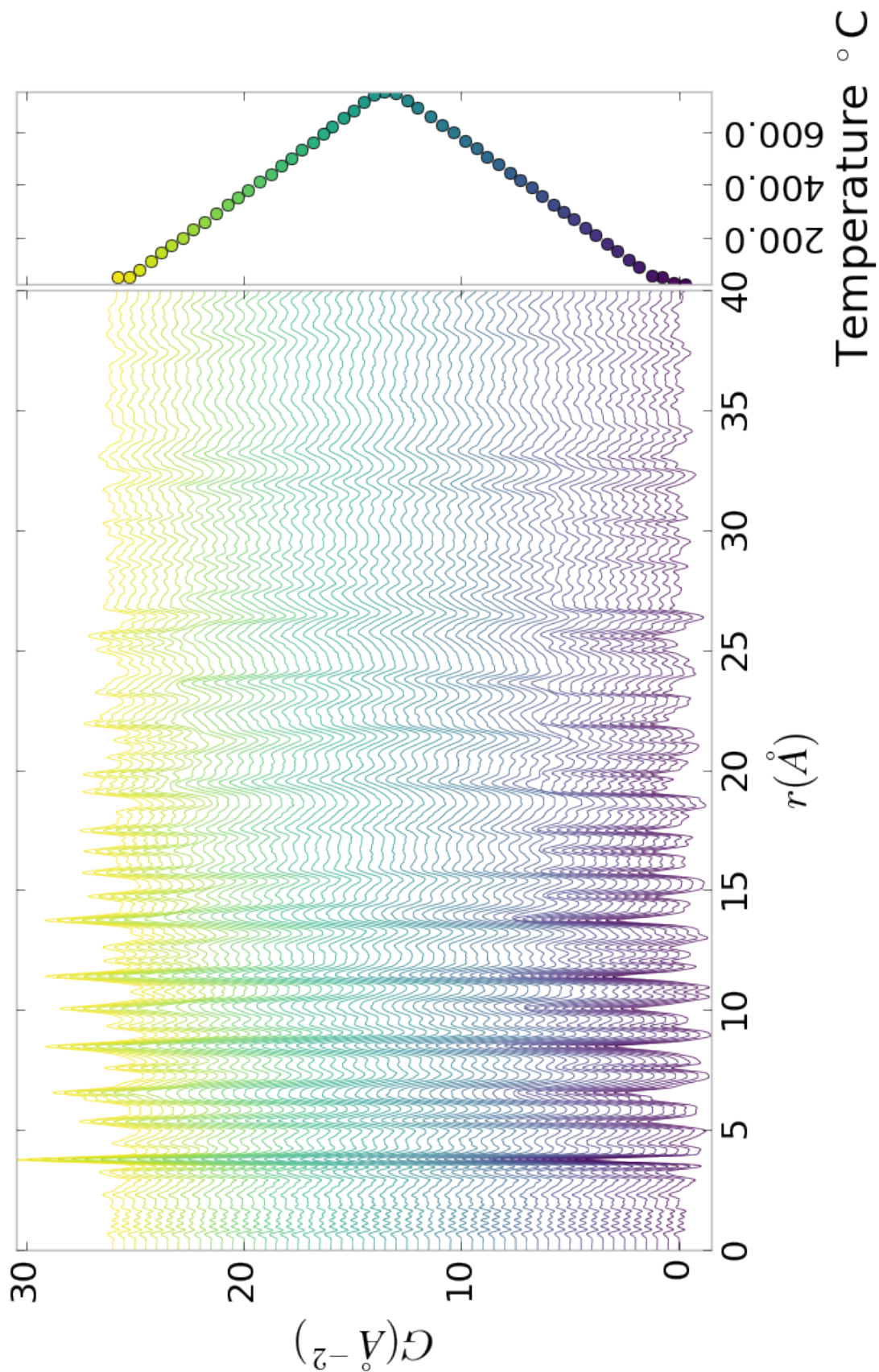


Figure A.5: PDF as a function of temperature for PNO annealed at 750 $^{\circ}\text{C}$ for 200 hours showing the full PDF

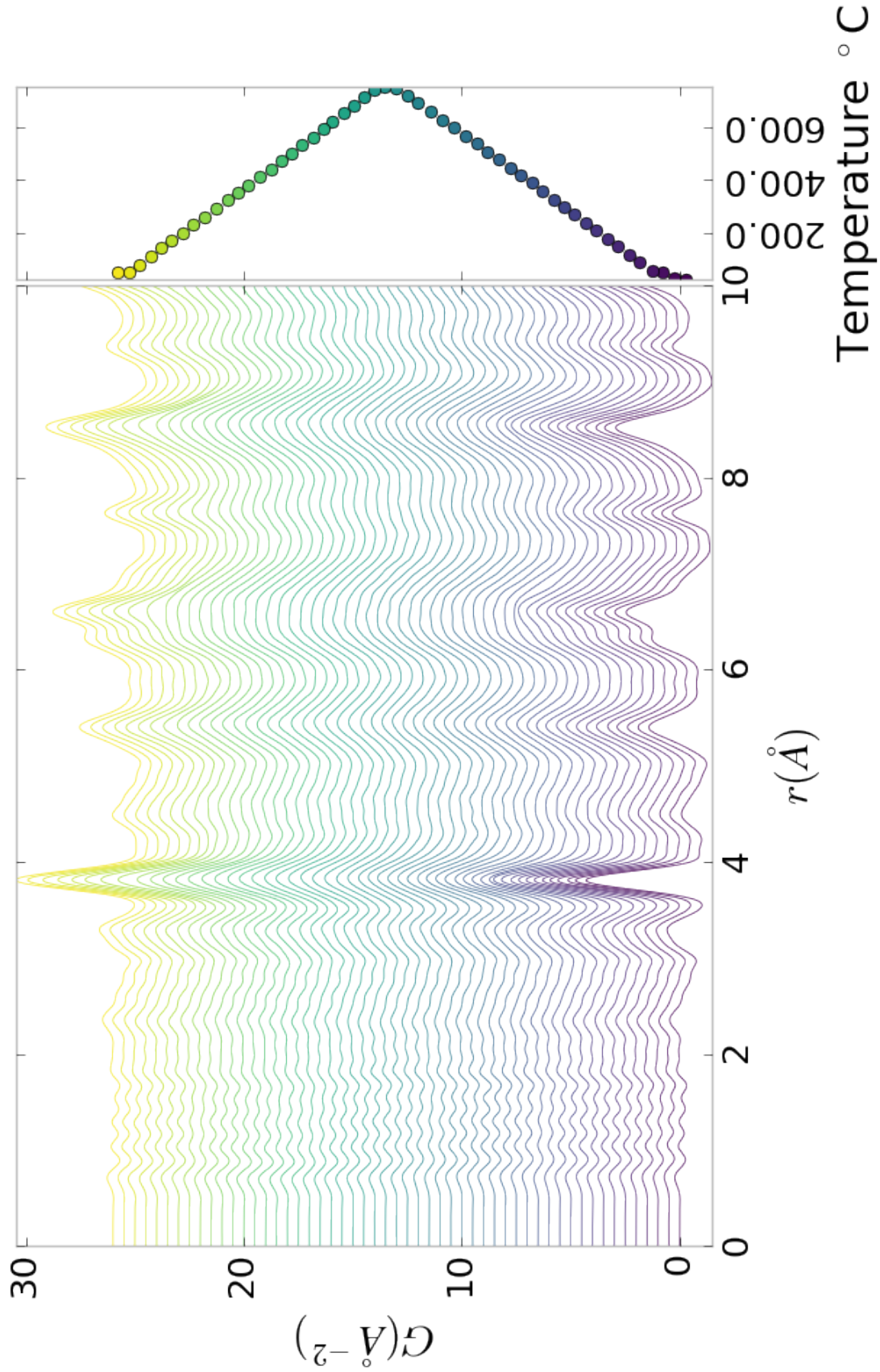


Figure A.6: PDF as a function of temperature for PNO annealed at 750 °C for 200 hours showing a close up on the short range section

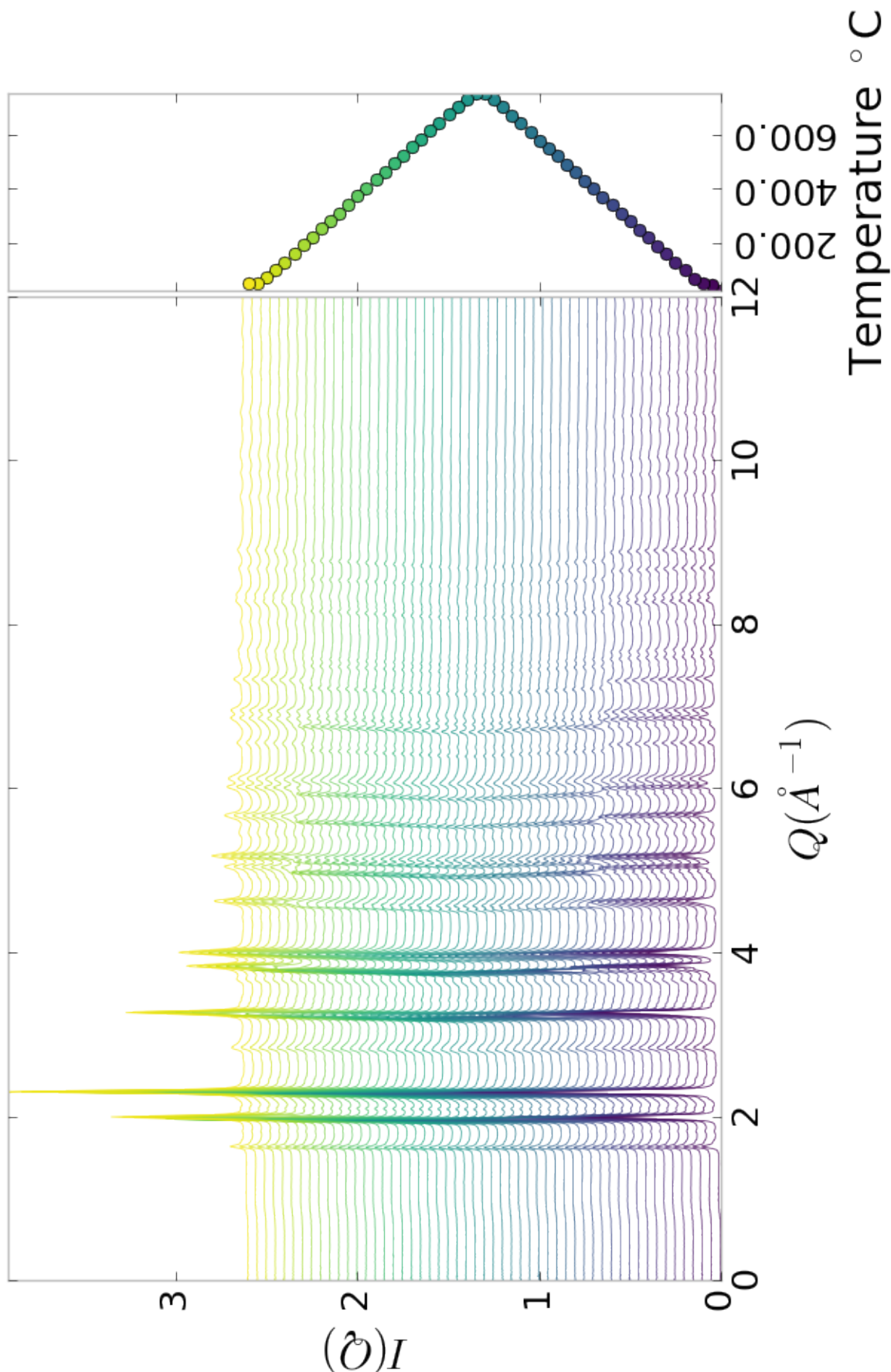


Figure A.7: $I(Q)$ as a function of temperature for PNO annealed at 750 $^{\circ}\text{C}$ for 50 hours showing the full XRD

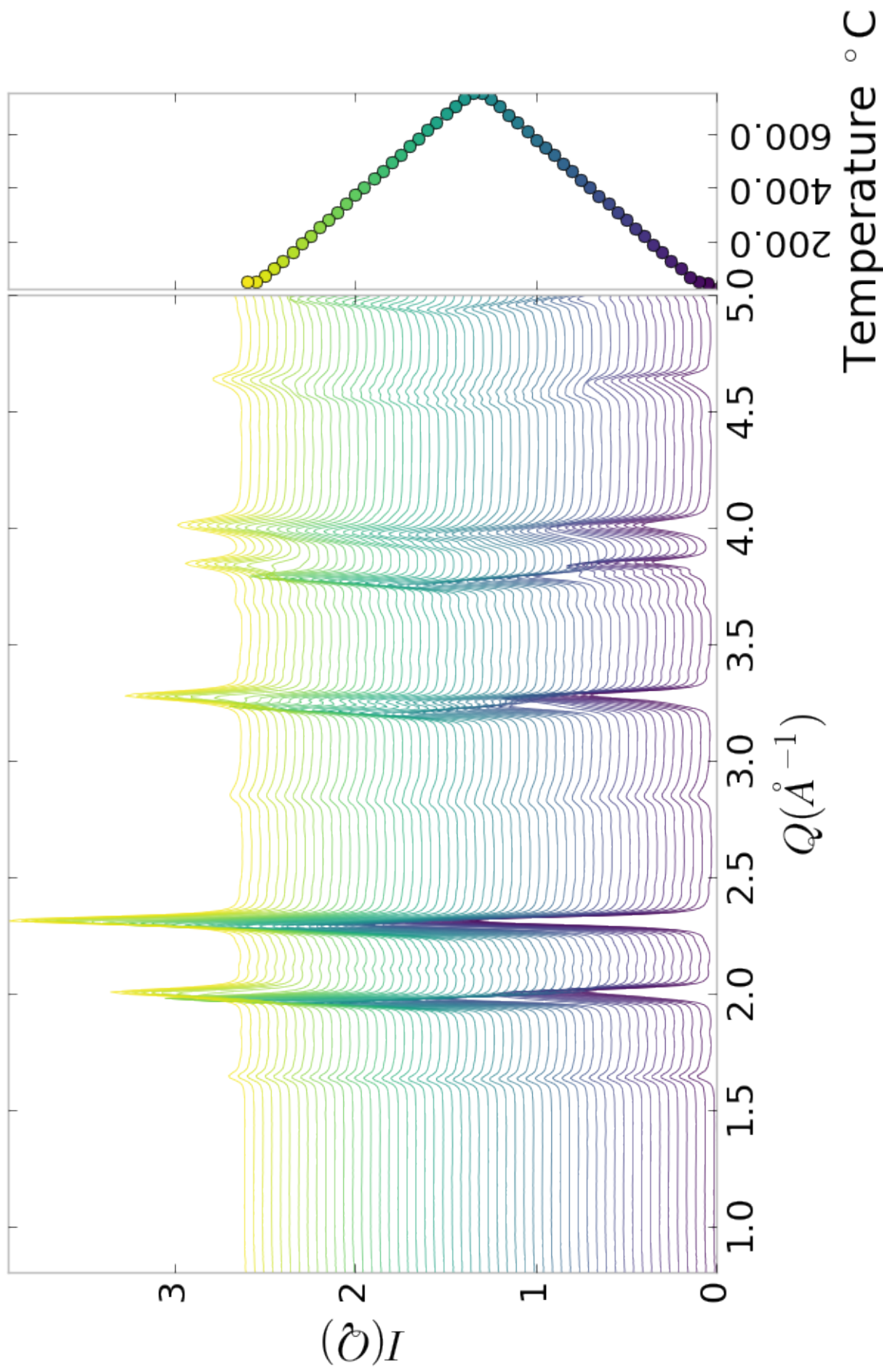


Figure A.8: $I(Q)$ as a function of temperature for PNO annealed at 750 °C for 50 hours showing a close up on the low Q section

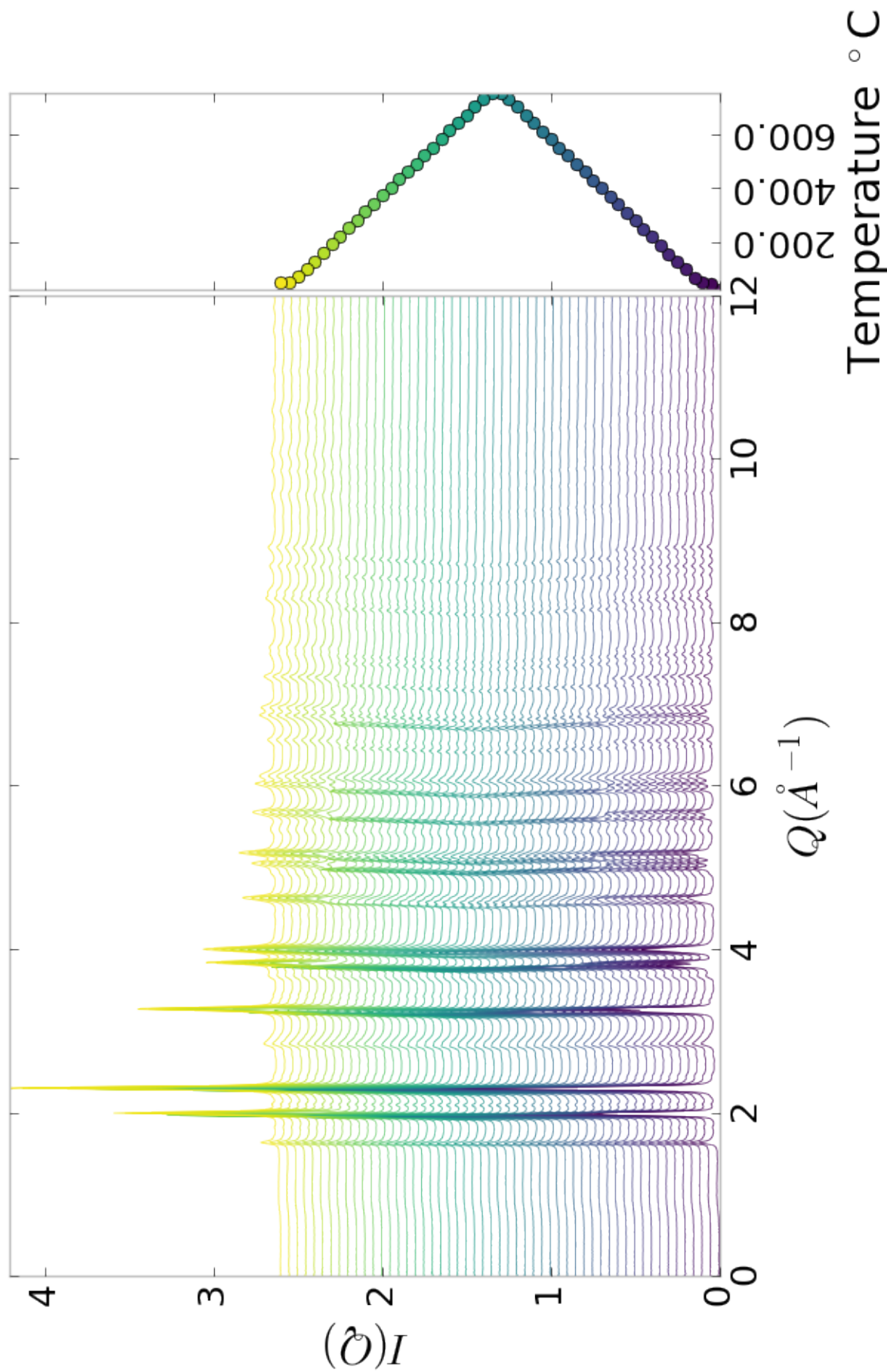


Figure A.9: $I(Q)$ as a function of temperature for PNO annealed at $750\text{ }^{\circ}\text{C}$ for 100 hours showing the full XRD

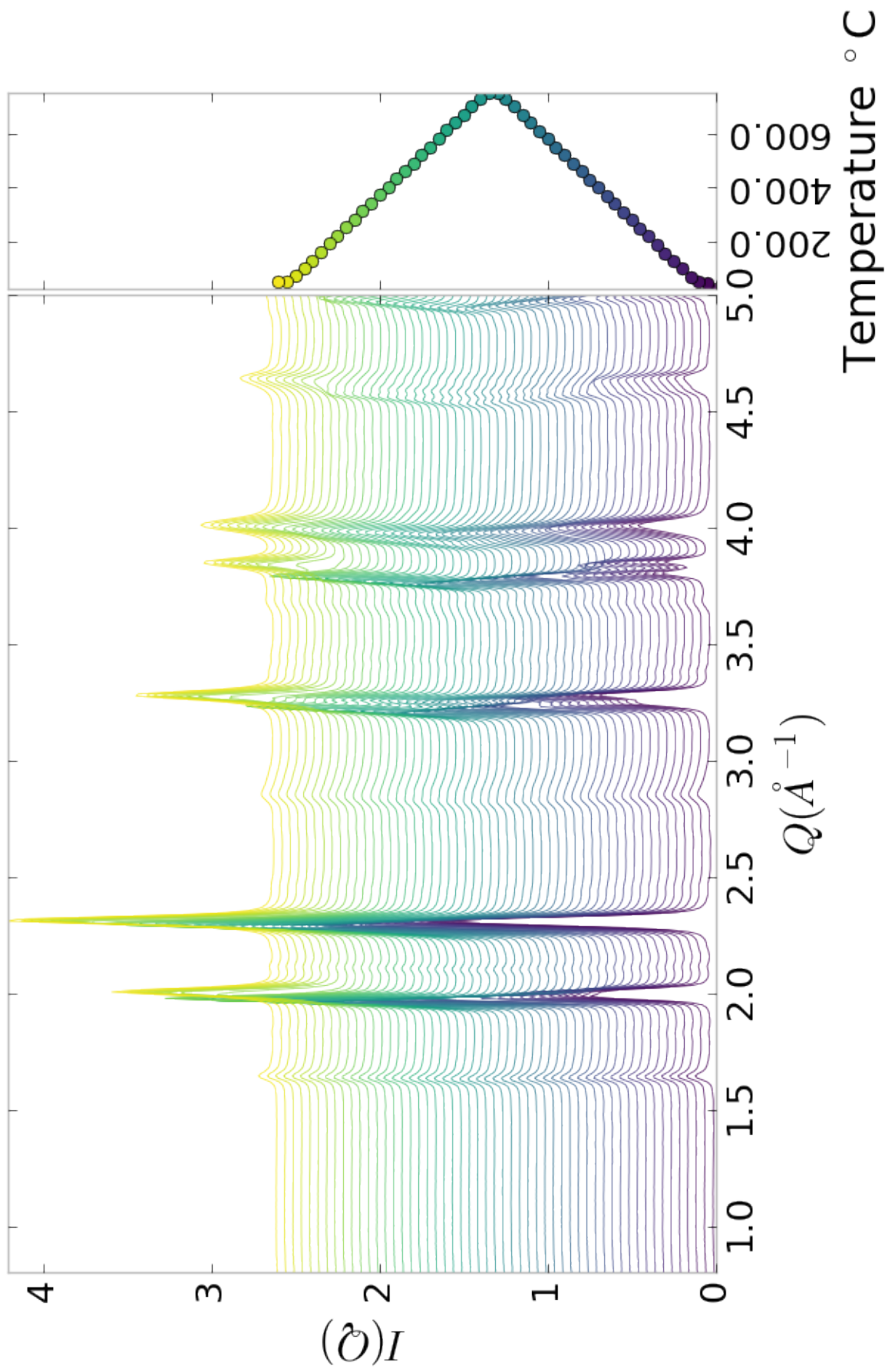


Figure A.10: $I(\vec{Q})$ as a function of temperature for PNO annealed at 750 °C for 100 hours showing a close up on the low Q section

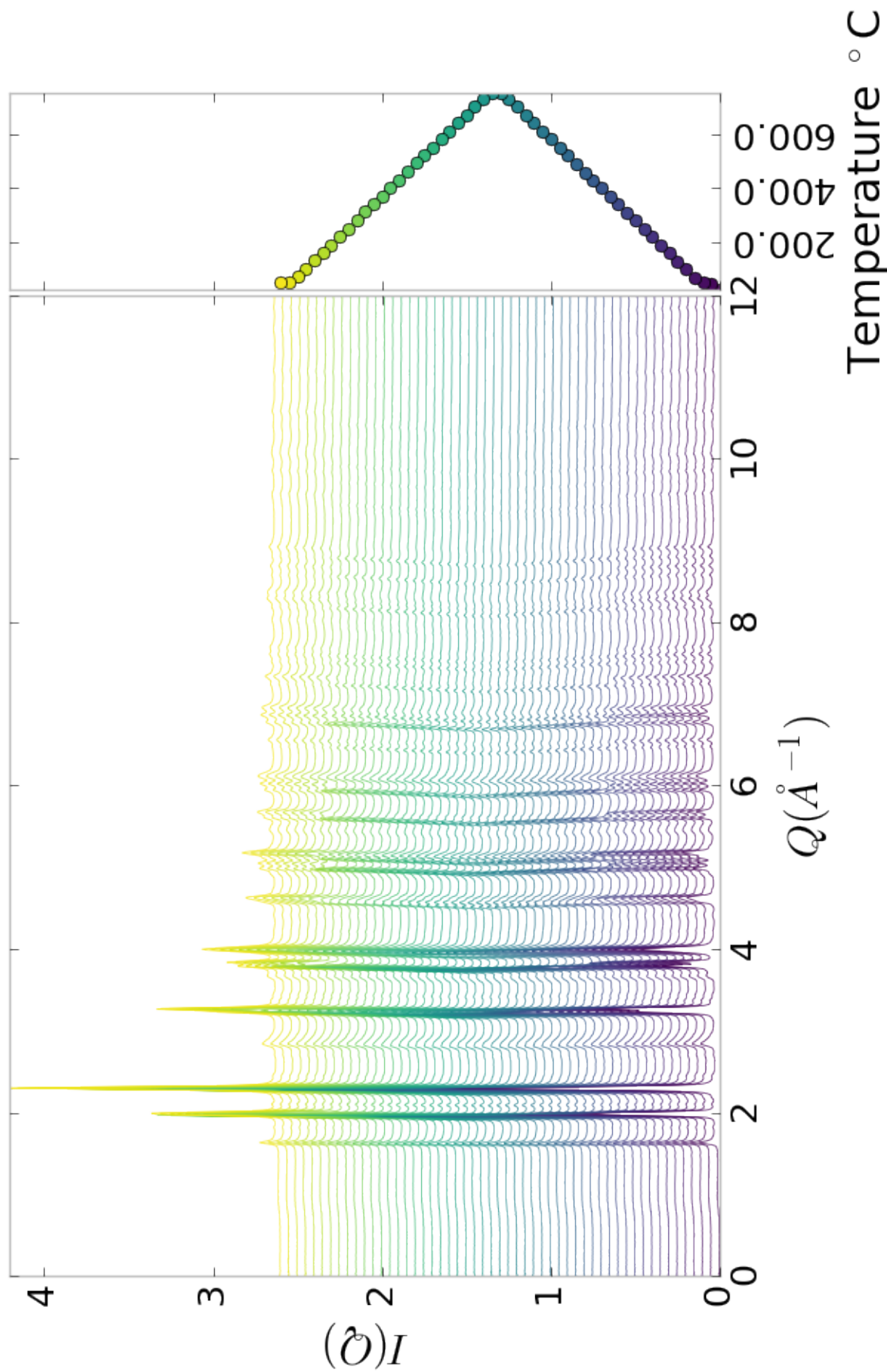


Figure A.11: $I(Q)$ as a function of temperature for PNO annealed at 750 $^{\circ}\text{C}$ for 200 hours showing the full XRD

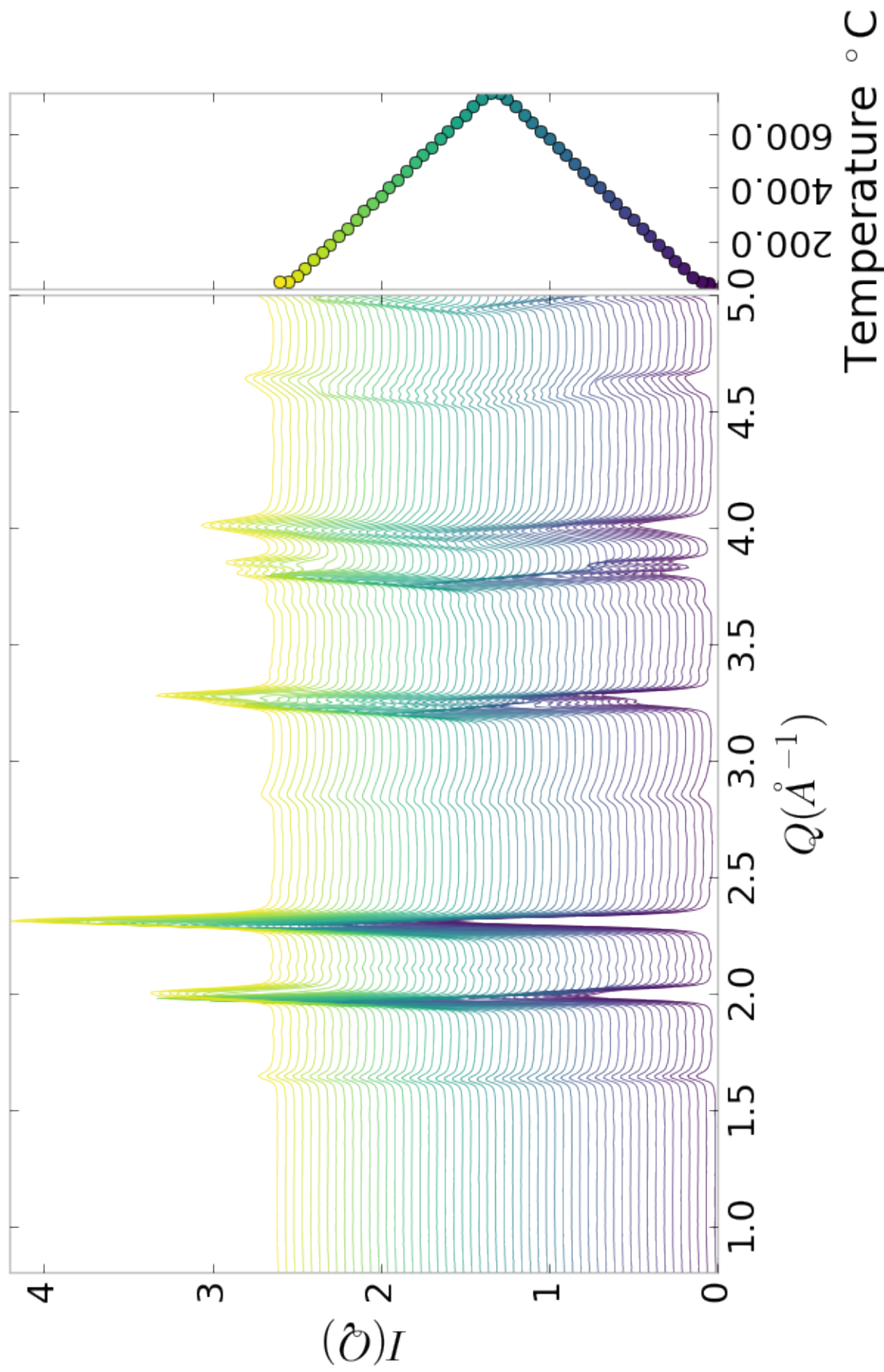


Figure A.12: $I(Q)$ as a function of temperature for PNO annealed at 750 °C for 200 hours showing a close up on the low Q section

1257 **Inter Sample Comparison**

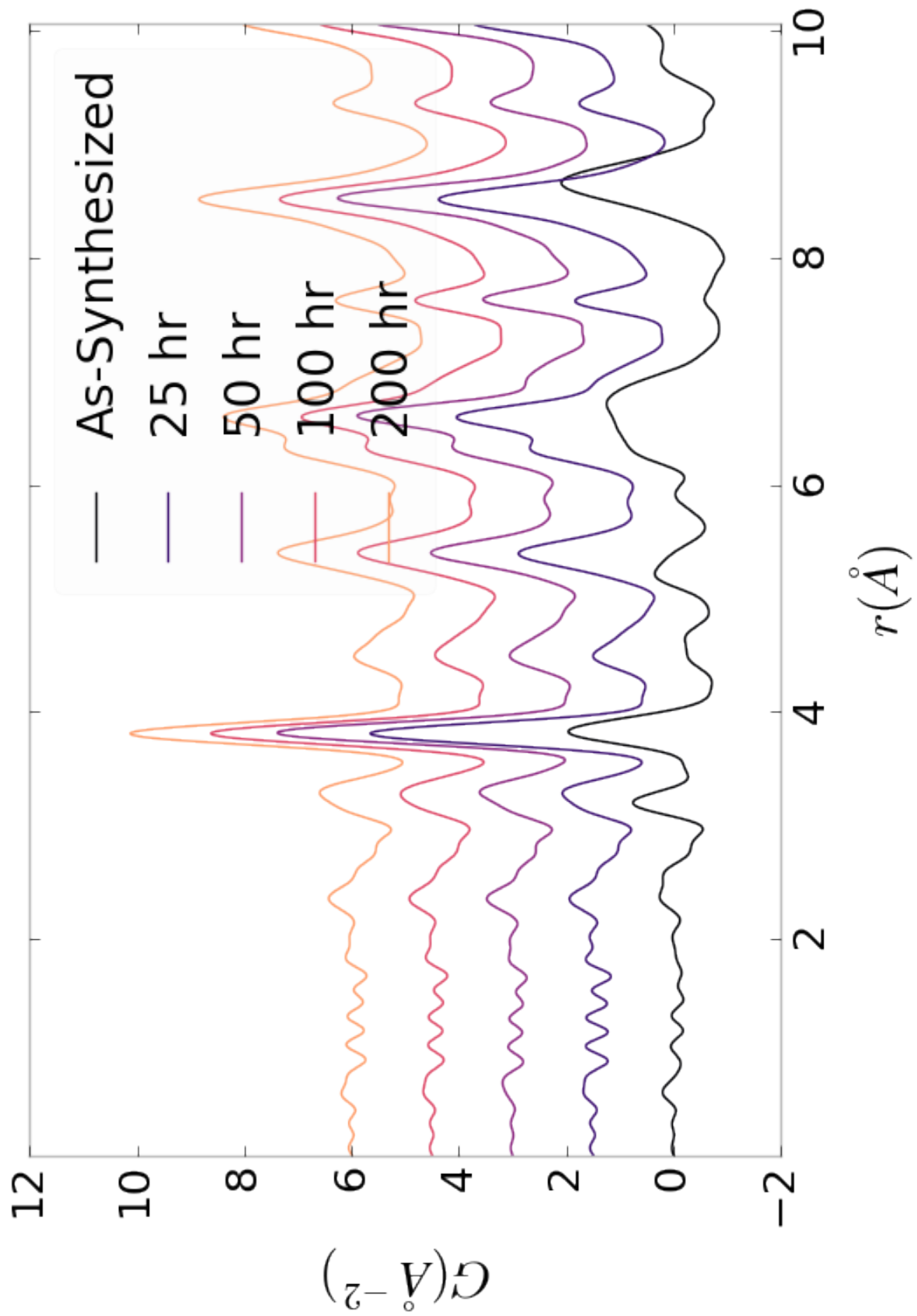


Figure A.13: Comparison of PNO sample PDFs as a function of annealing time at room temperature

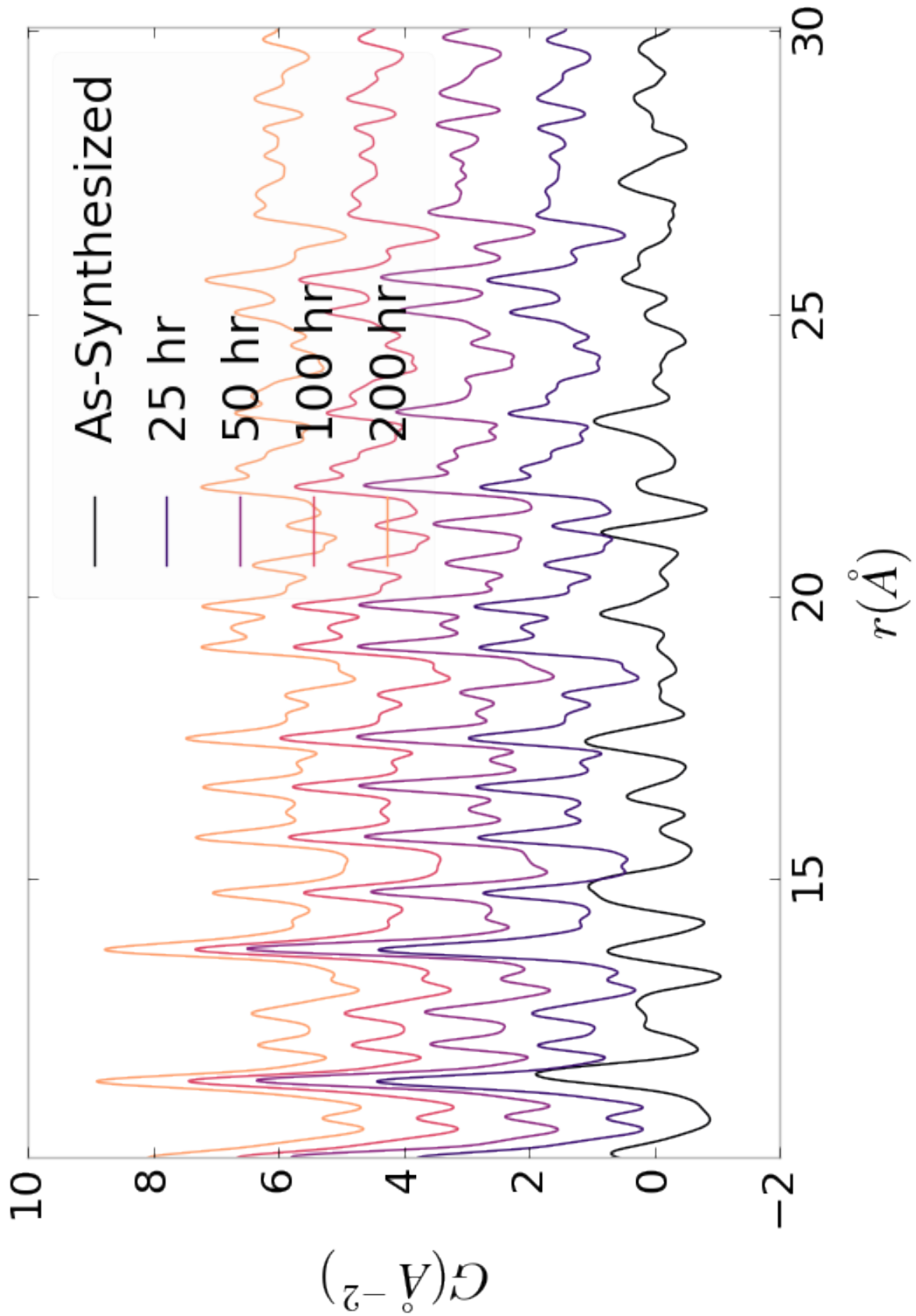


Figure A.14: Comparison of PNO sample PDFs as a function of annealing time at room temperature

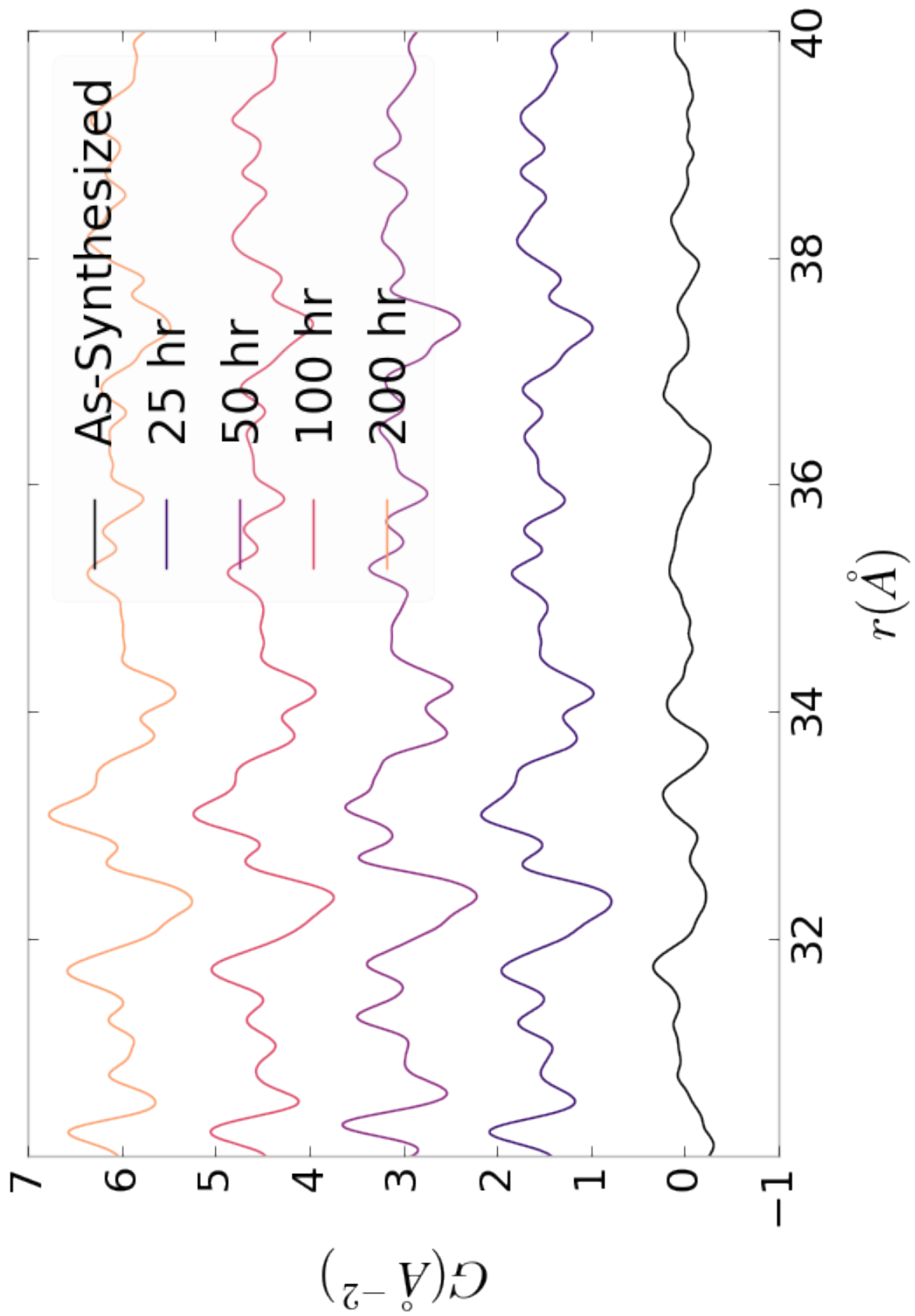


Figure A.15: Comparison of PNO sample PDFs as a function of annealing time at room temperature

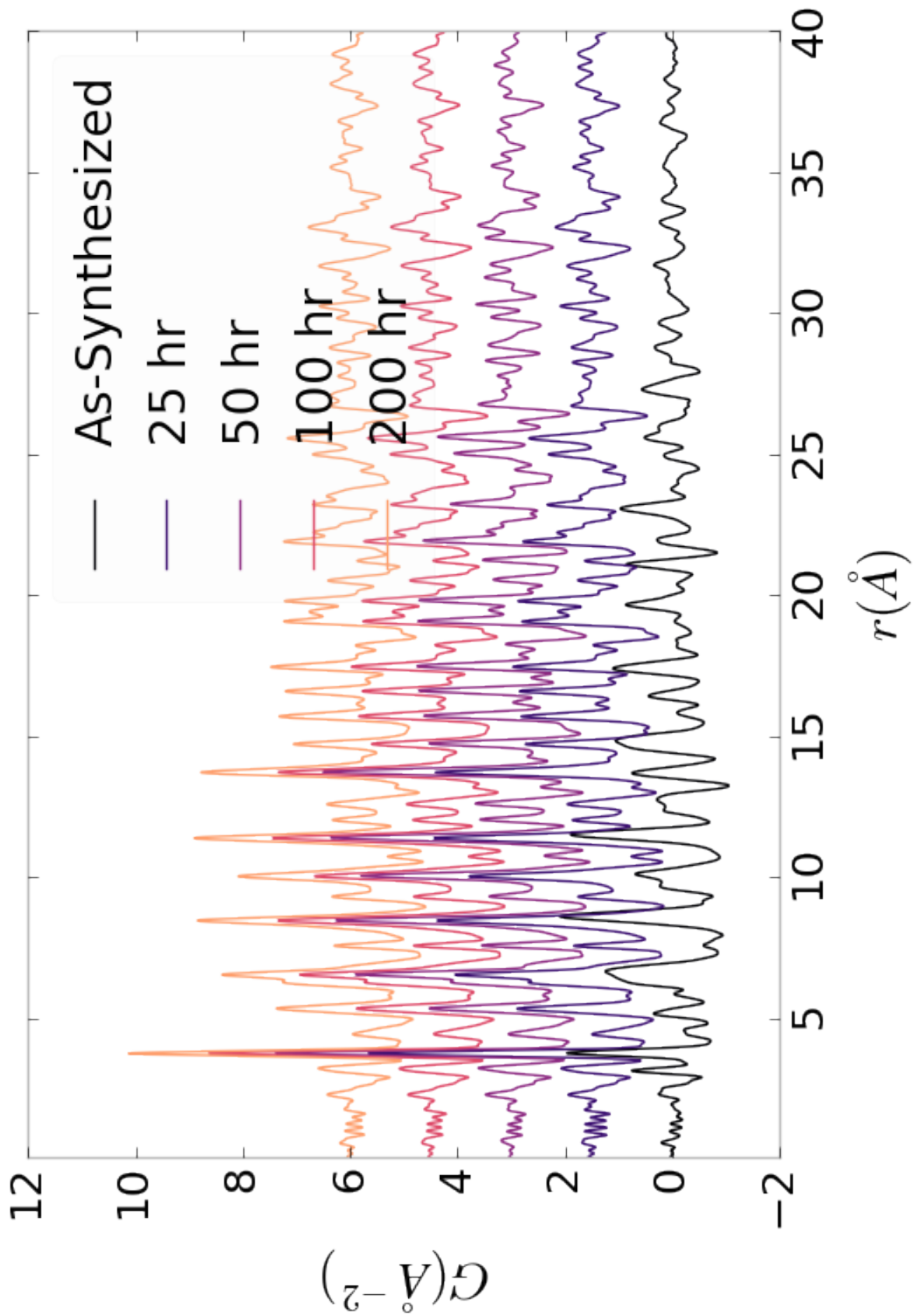


Figure A.16: Comparison of PNO sample PDFs as a function of annealing time at room temperature

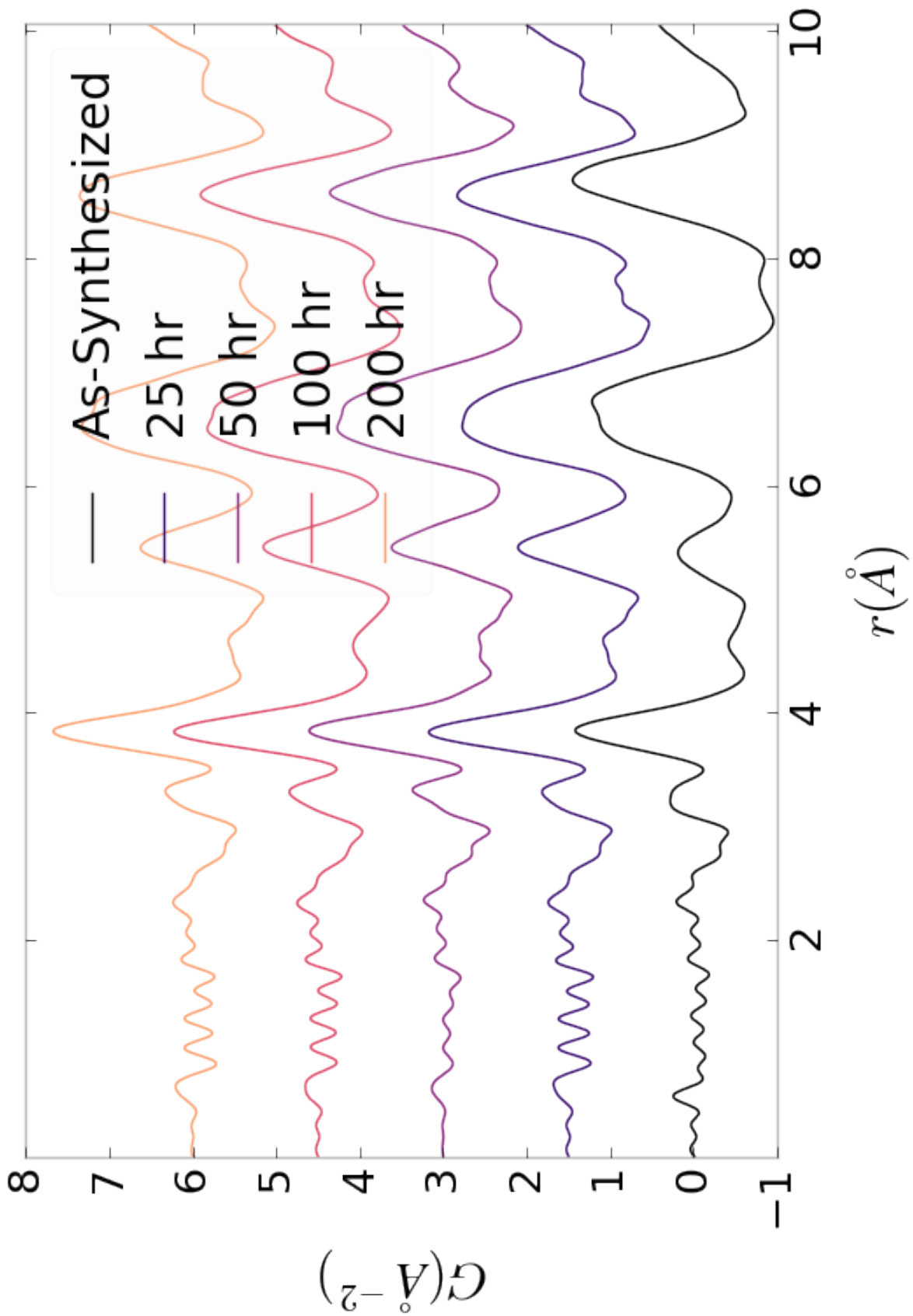


Figure A.17: Comparison of PNO sample PDFs as a function of annealing time at operating temperature

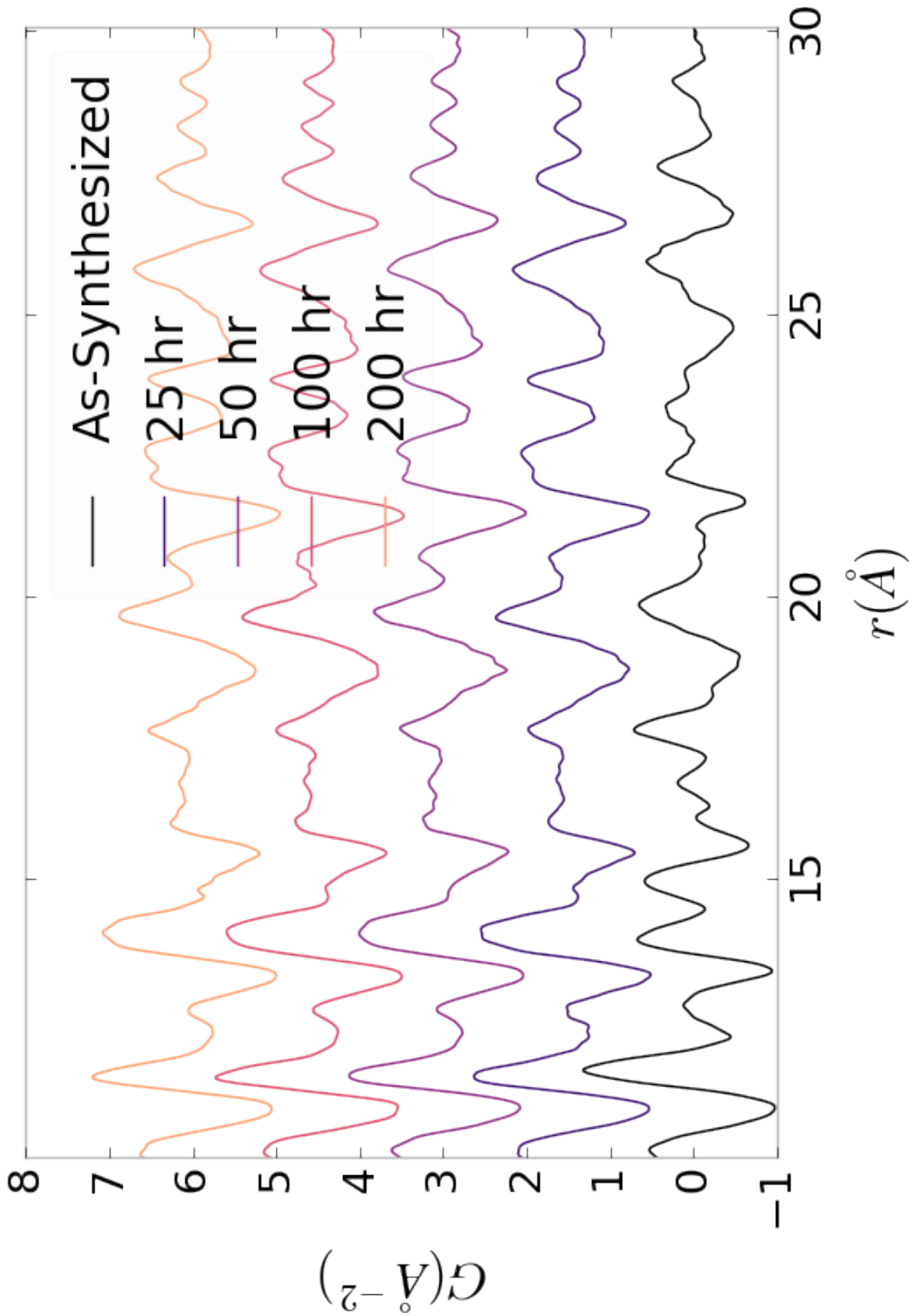


Figure A.18: Comparison of PNO sample PDFs as a function of annealing time at operating temperature

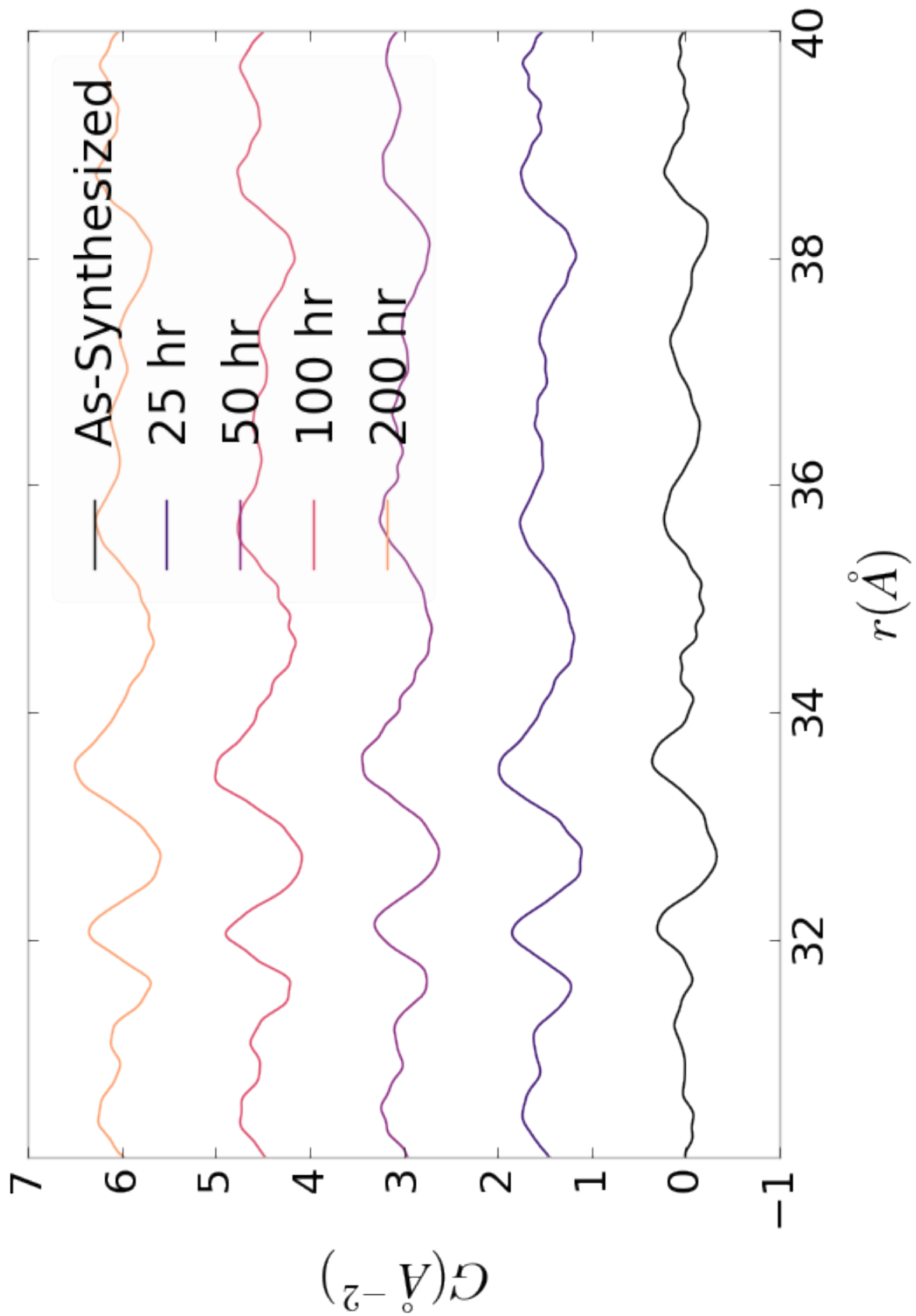


Figure A.19: Comparison of PNO sample PDFs as a function of annealing time at operating temperature

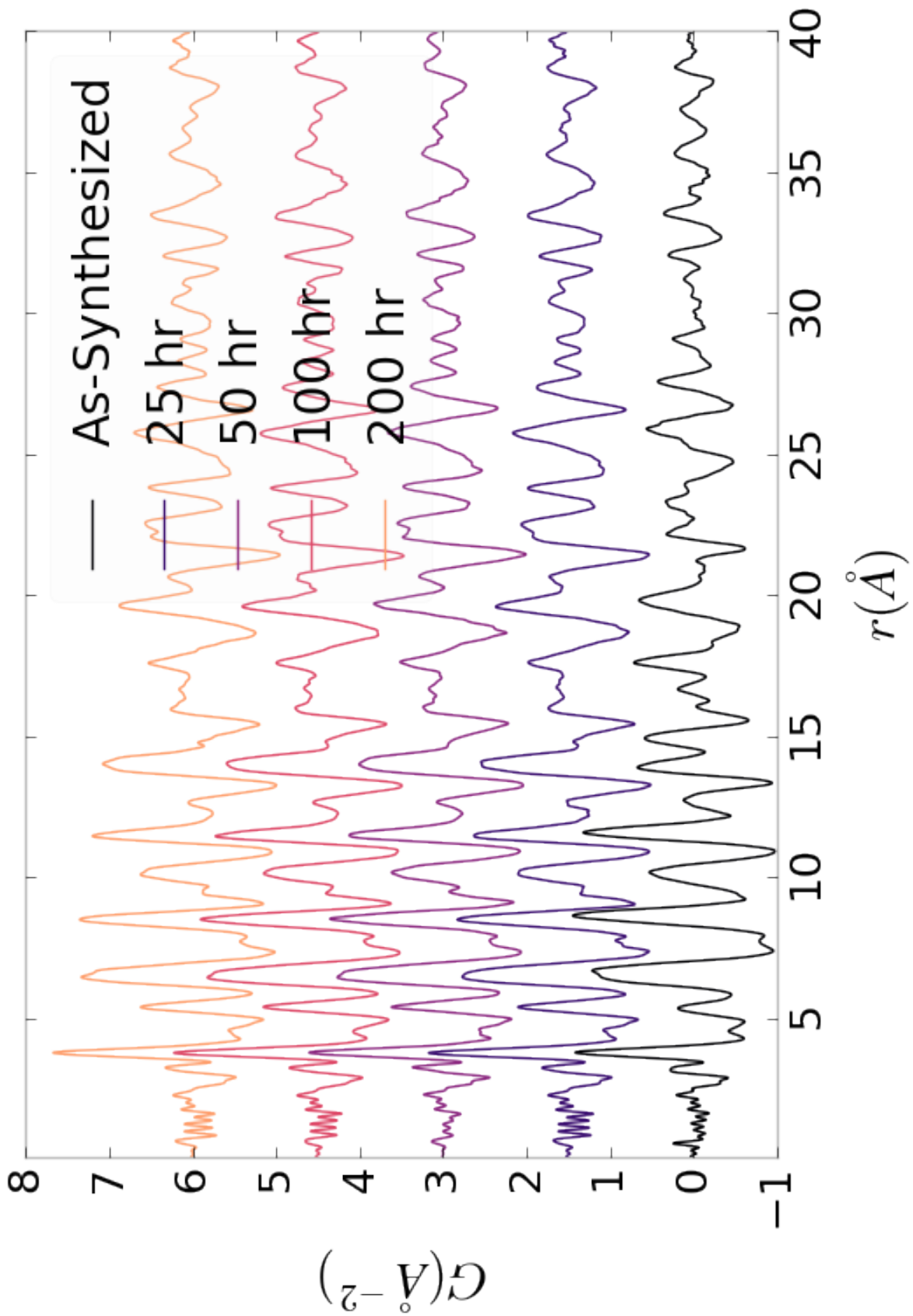


Figure A.20: Comparison of PNO sample PDFs as a function of annealing time at operating temperature

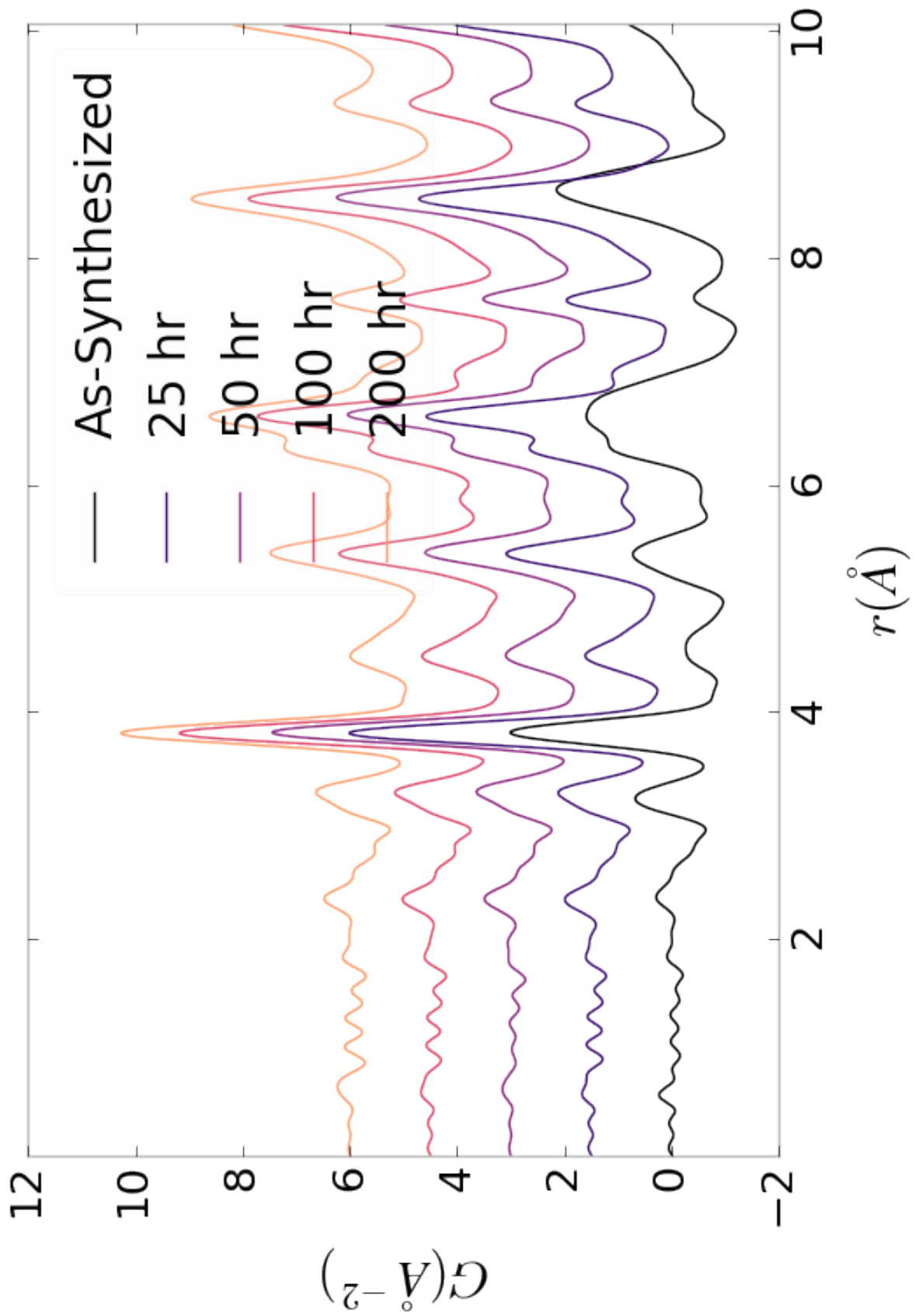


Figure A.21: Comparison of PNO sample PDFs as a function of annealing time cooled back to room temperature

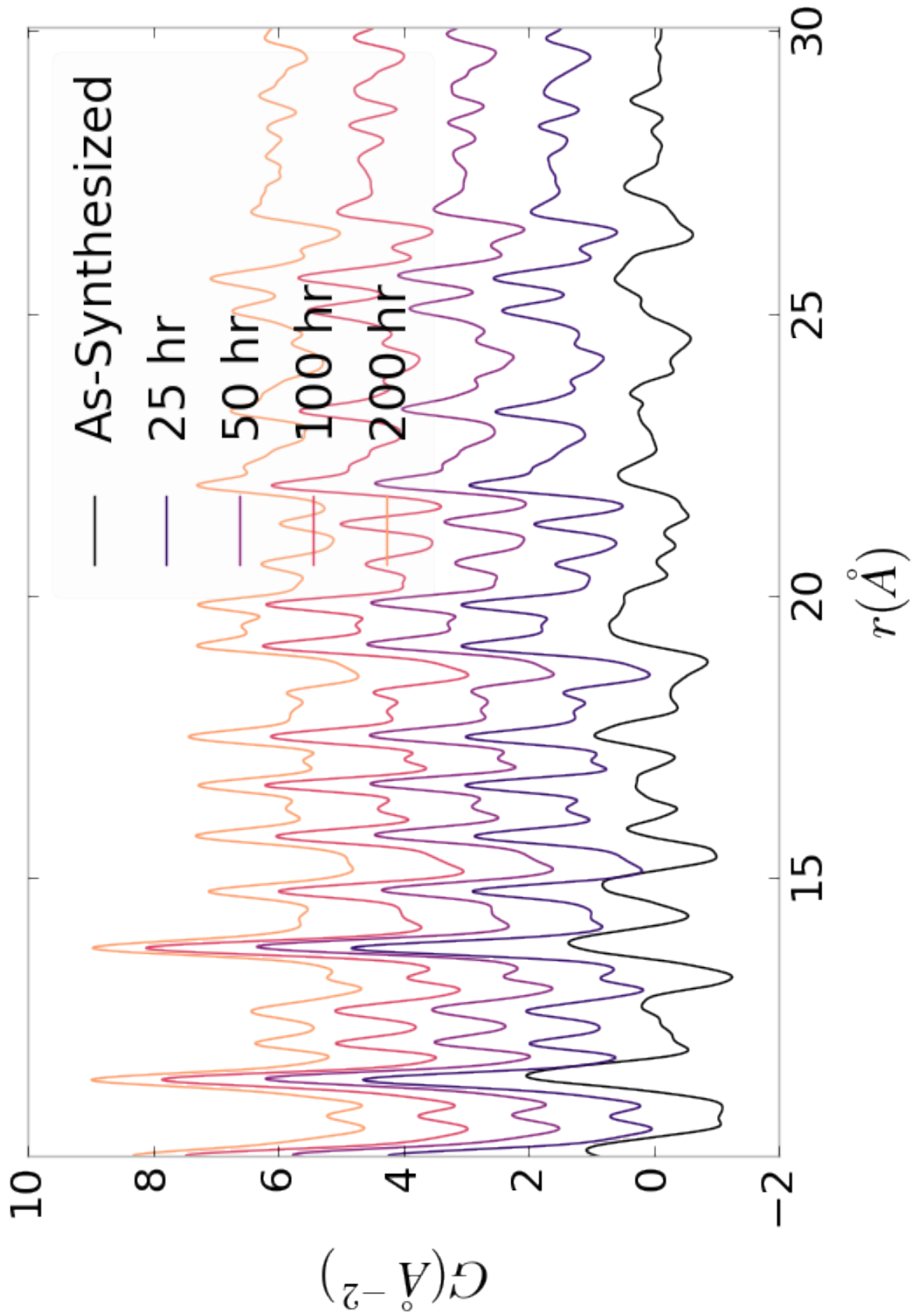


Figure A.22: Comparison of PNO sample PDFs as a function of annealing time cooled back to room temperature

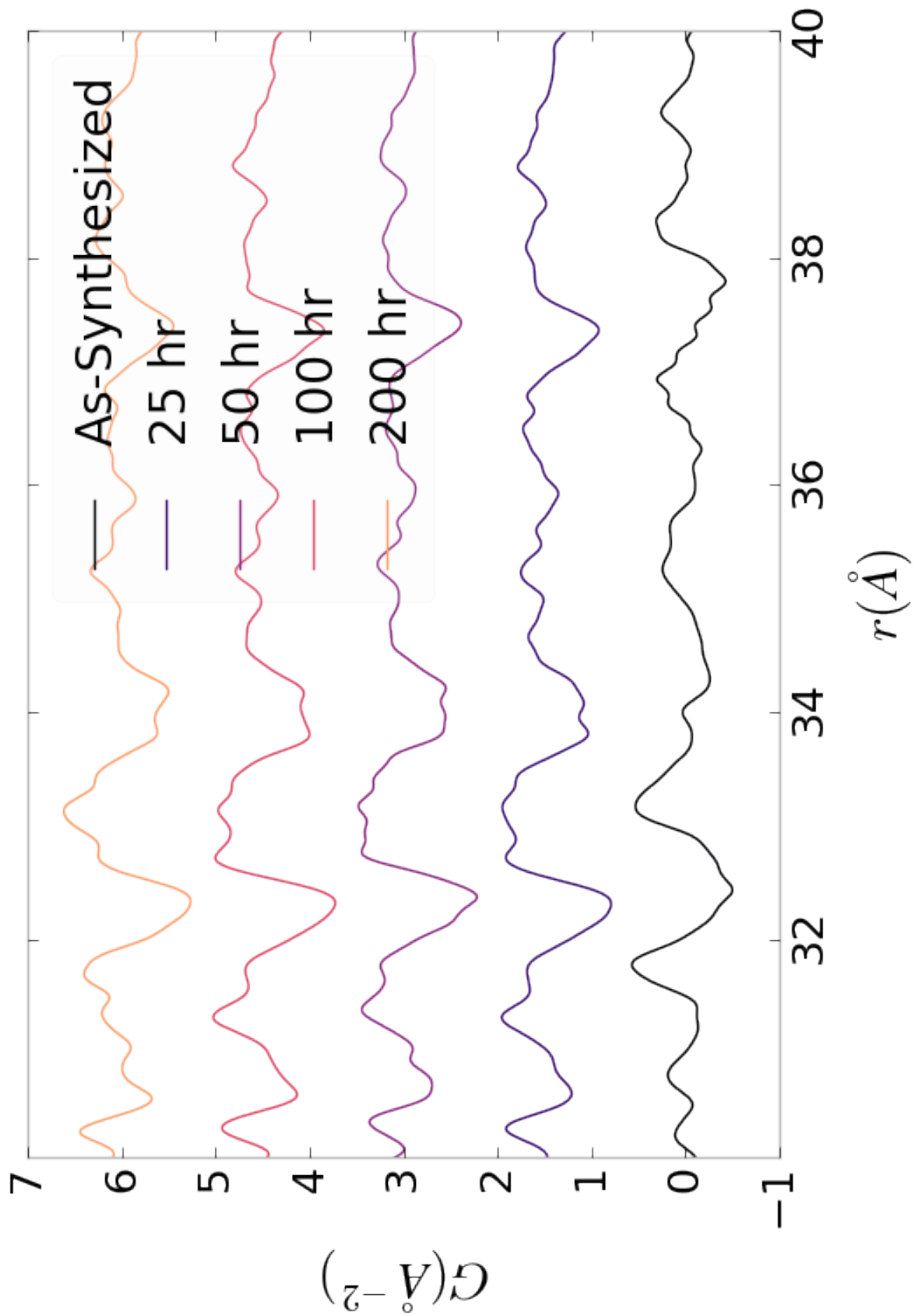


Figure A.23: Comparison of PNO sample PDFs as a function of annealing time cooled back to room temperature

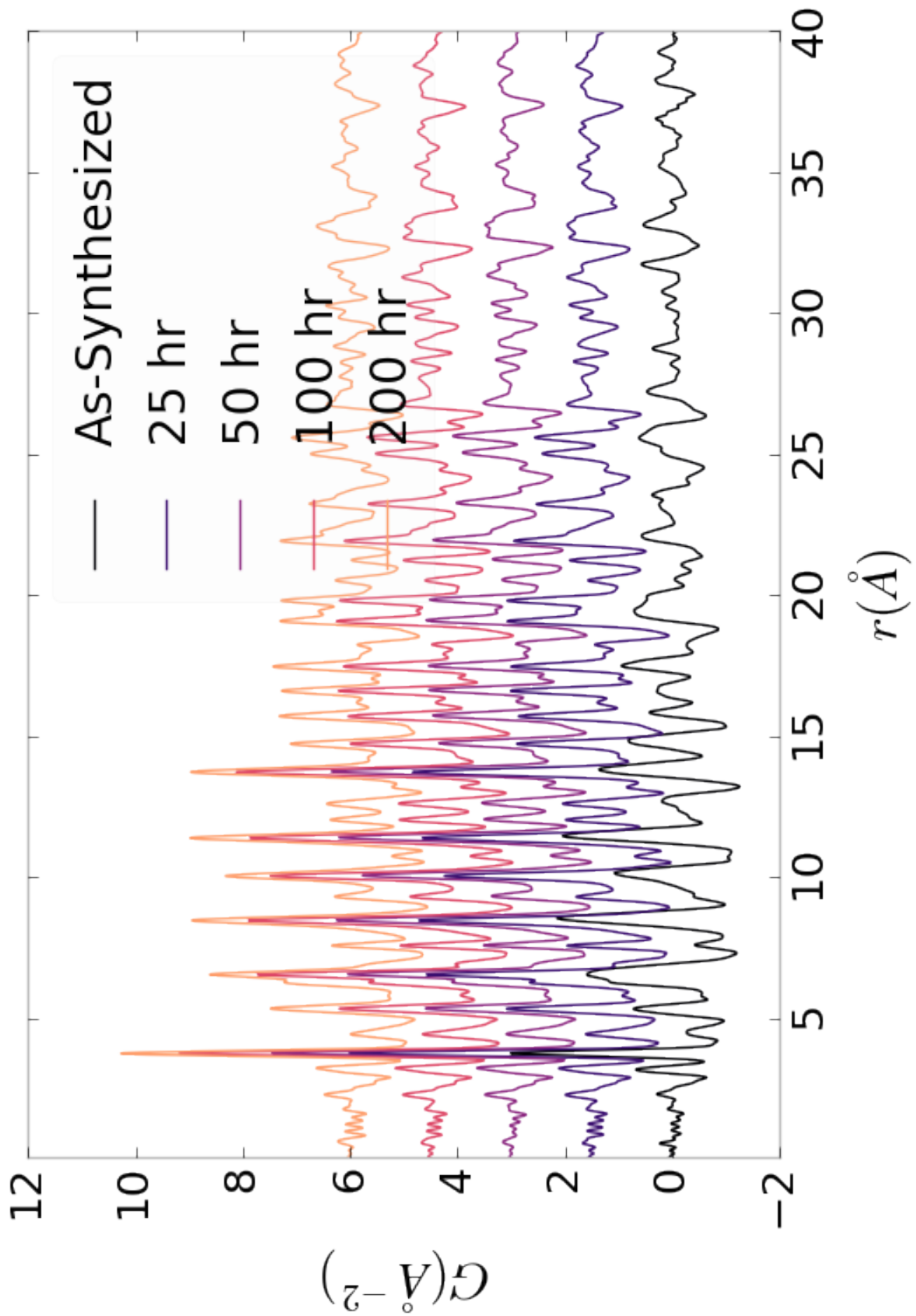


Figure A.24: Comparison of PNO sample PDFs as a function of annealing time cooled back to room temperature

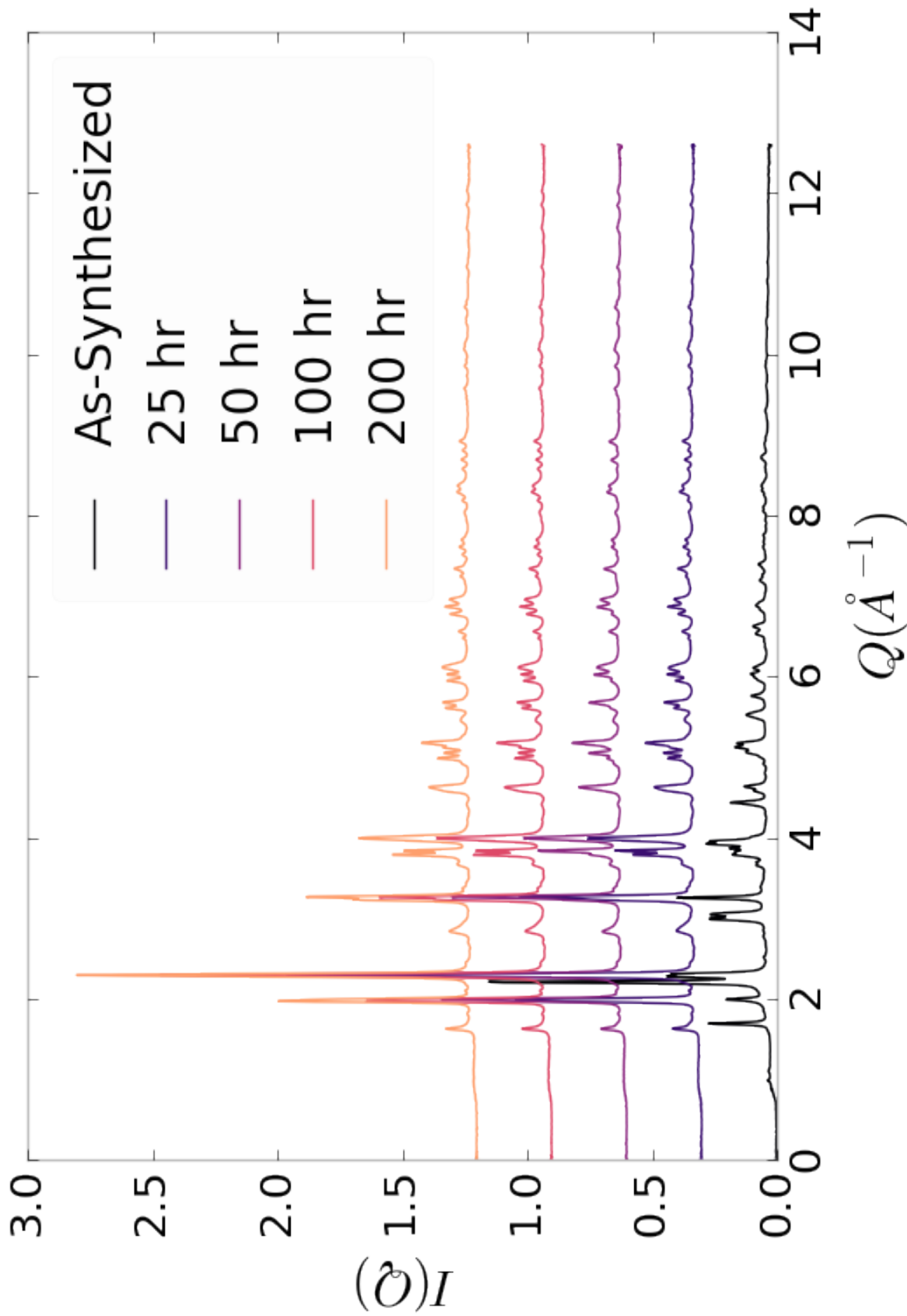


Figure A.25: Comparison of PNO sample $I(Q)$ as a function of annealing time at room temperature

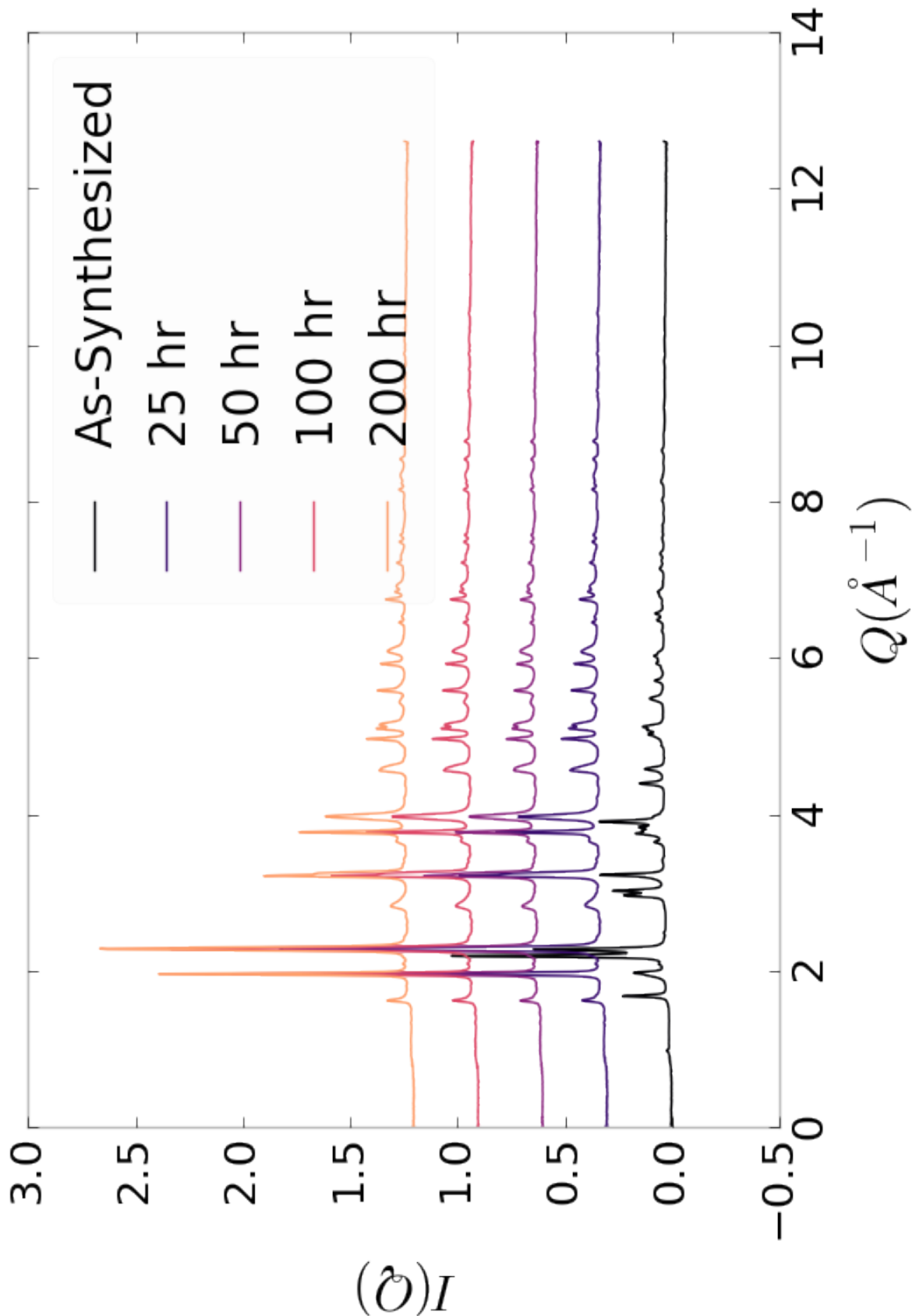


Figure A.26: Comparison of PNO sample $I(Q)$ as a function of annealing time at operating temperature

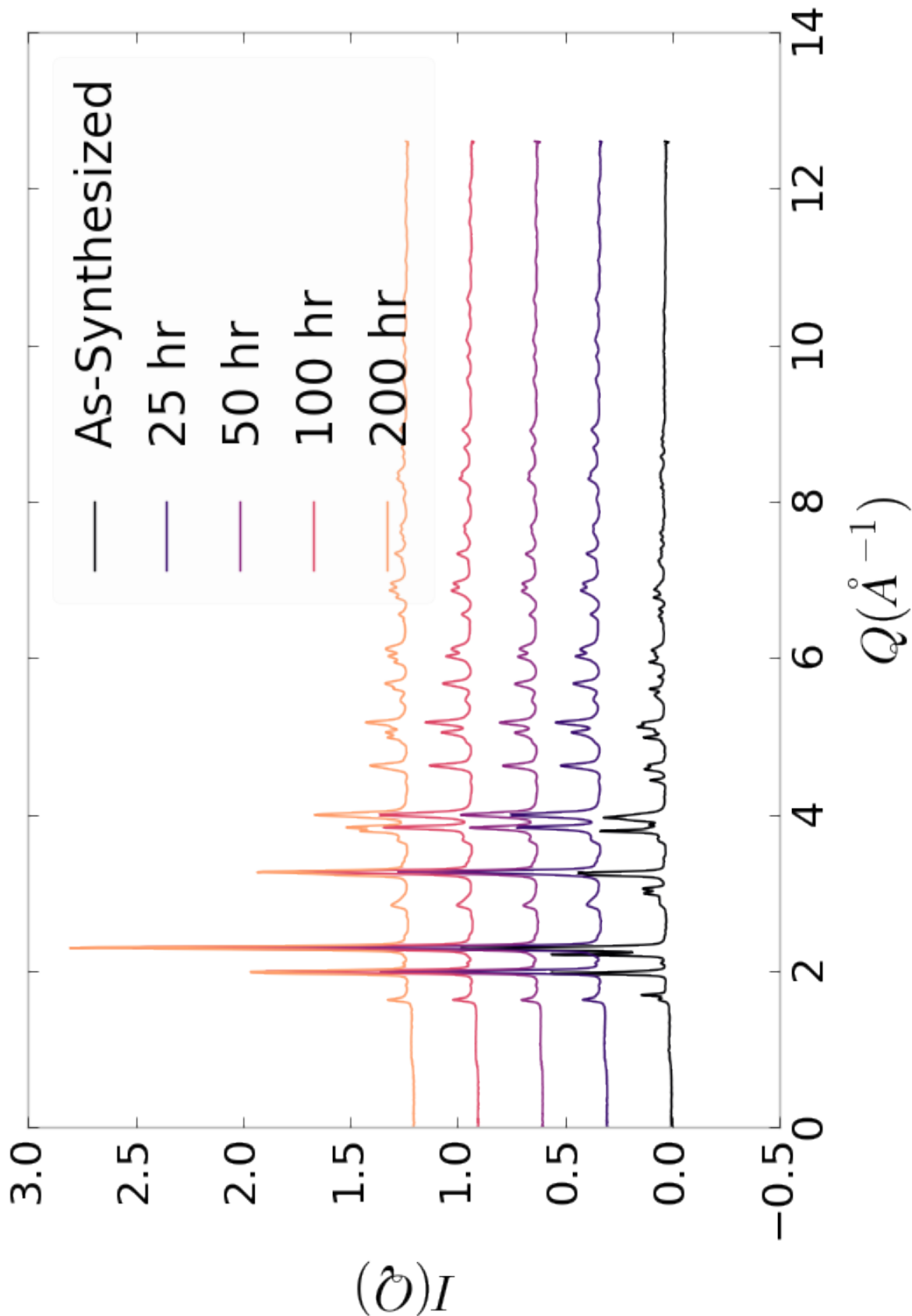


Figure A.27: Comparison of PNO sample $I(Q)$ as a function of annealing time cooled back to room temperature